

Monte Carlo Techniques of Electron and Photon Transport for Radiation Dosimetry

D.W.O. Rogers and A.F. Bielajew
National Research Council of Canada Ottawa, Canada
K1A 0R6

Reprinted from
Chapter 5, Vol. III The Dosimetry of Ionizing Radiation
Edited by Kenneth R. Kase, Bengt E. Bjarngard and
Frank H. Attix
(Academic Press, 1990)

This version has been reworked electronically by scanning the original, then optical character recognition and lots of checking. Many figures have been redrawn using the original data files but some have just been scanned in. To maintain identical pagination, new pages are often forced in mid-line.

Please report any remaining typos/misinterpreted symbols to drogers@physics.carleton.ca.

Dave Rogers is currently at Carleton University Ottawa (drogers@physics.carleton.ca),

Alex Bielajew is at University of Michigan, Ann Arbor (bielajew@umich.edu).

Revised Jan 10, 2014 to correct typos noted by Patty Oliver

Contents

I. Introduction	427
II. Monte Carlo Codes	428
II.A. OVERVIEW: THE MONTE CARLO TECHNIQUE	428
II.A.1. What Is Monte Carlo?	428
II.A.2. Photon, Electron, and Atomic Processes	430
II.A.3. Photon Transport	433
II.A.4. Sampling a Physical Process	434
II.A.5. Class I and Class II Models and Thresholds for Discrete Events	436
II.A.6. Energy Loss in a Thin Slab of Water	438
II.A.7. Electron Transport	443
II.B. CROSS-SECTION DEPENDENCE ON ENERGY AND ATOMIC NUMBER	446
II.B.1. Photons	446
II.B.2. Electrons and Positrons	453
II.C. STEP-SIZE EFFECTS	460
II.D. SCORING QUANTITIES OF INTEREST	467
II.D.1. Introduction	467
II.D.2. Scoring Techniques	468
II.D.3. Use of Symmetries	471
II.E. THE SELECTION OF RANDOM NUMBERS	472
II.F. AN EXAMPLE: 20-MEV ELECTRONS ON A SLAB OF WATER	474
II.F.1. Depth-Dose Curves	475
II.F.2. Fluence Versus Depth	477
II.F.3. Energy Versus Depth	479
II.F.4. Beam Radius Effects	481
II.G. A COMPARISON OF ETRAN AND EGS	481
II.G.1. Class I Versus Class II Algorithms	482
II.G.2. Multiple Scattering	483
II.G.3. Transport at Low Energies and Termination of Histories	487
II.G.4. Step Sizes, Boundary Crossings, Variance Reduction, and Timing	489
II.G.5. Other Differences	491
III. Code Accuracy	492
III.A. CROSS-SECTION DATA	492

III.A.1. Photons	493
III.A.2. Electrons	493
III.B. OTHER SYSTEMATIC AND STATISTICAL UNCERTAINTIES	493
III.B.1. Systematic Errors	494
III.B.2. Statistical Uncertainties	495
III.B.3. Computing Efficiency	496
III.C. EXPERIMENTAL BENCHMARKS	497
III.C.1. Response Functions for Photon and Electron Detectors	498
III.C.2. Photon Depth-Dose Curves	500
III.C.3. Absorbed Dose per Unit Incident Fluence of 7-MeV Photons	504
III.C.4. Bremsstrahlung Production	505
III.C.5. Electron Depth-Dose Curves	508
III.C.6. Ion Chamber Response to ^{60}Co γ -Rays	513
III.C.7. Dose at an Interface	517
III.C.8. Stopping-Power Ratios	521
IV. Variance Reduction Techniques	522
IV.A. INTRODUCTION	522
IV.B. EXPONENTIAL TRANSFORMATION OF PHOTON PATH LENGTH AND FORCED INTERACTIONS	523
IV.C. ENHANCED CROSS SECTIONS	526
IV.D. RANGE REJECTION OF ELECTRONS	526
IV.E. USE OF PRECOMPUTED RESULTS	527
V. Computing Requirements	528
V.A. INTRODUCTION	528
V.B. A TREATMENT-PLANNING EXAMPLE	529
VI. Conclusions	531
VII. Appendix A: Computational Models	532
VIII. Acknowledgment	532
IX. References	533

5

Monte Carlo Techniques of Electron and Photon Transport for Radiation Dosimetry

D. W. O. ROGERS and A. F. BIELAJEW
DIVISION OF PHYSICS
NATIONAL RESEARCH COUNCIL OF CANADA
OTTAWA, ONTARIO, CANADA K1A 0R6

I. Introduction

In this chapter we discuss the Monte Carlo simulation of the transport of electrons and photons through bulk media in the energy range 10 keV to 50 MeV. The Monte Carlo technique consists of using knowledge of the probability distributions governing the individual interactions of electrons and photons in materials to simulate the random trajectories of individual particles. One keeps track of physical quantities of interest for a large number of histories to provide the required information about average quantities and their associated distributions.

Many problems in radiation dosimetry, radiotherapy physics, and radiation protection have been addressed by Monte Carlo techniques because the complexity of electron and photon transport in material renders analytic solutions intractable. The use of Monte Carlo techniques in these fields has increased dramatically in the last few years for a combination of reasons. One is the rapid increase in speed and decrease in cost of data processing. At the same time, large, general-purpose software packages have become available. Furthermore, the use of high-energy photon and electron beams for radiotherapy makes it essential to take into account electron transport for dosimetry and treatment planning purposes. This can be done in complete generality only by using coupled electron-photon Monte Carlo calculations.

Monte Carlo techniques were originally developed, and are still extensively used, to study neutron and photon transport for nuclear power

reactor applications. Neutron and photon problems are in some ways inherently simpler than those for electrons because the number of neutron and photon interactions is low enough that each interaction event may be simulated explicitly. In the case of electrons, the large number of interactions necessitates a more complex approach, which also greatly increases the computing time per particle. On the other hand, electron and photon cross sections are relatively smooth in the energy range of interest. This greatly simplifies calculations compared to neutron transport, where the cross sections vary rapidly.

Although electron transport via Monte Carlo techniques has not received as much attention as neutron and photon transport, two widely used and very sophisticated approaches are available. One is based on the ETRAN (electron transport) codes originally developed at the National Bureau of Standards by Berger and Seltzer (1973). The other is based on the EGS (electron-gamma-shower) code developed by Ford and Nelson (1978) at the Stanford Linear Accelerator Center.

A Monte Carlo simulation code has four major components: (1) the cross-section data for all the processes being considered in the simulation, (2) the algorithms used for the particle transport, (3) the methods used to specify the geometry of the problem and to determine the physical quantities of interest, and (4) the analysis of the information obtained during the simulation.

While the last two components can greatly affect running time, they do not affect the underlying physics of the simulation. Hence, when we speak of the EGS or ETRAN code we really mean only the first two of these components.

The purpose of this chapter is to give an overview of Monte Carlo simulation of electron and photon transport and to indicate the accuracy of these techniques. Chapter 6 in this volume gives examples of the use of this technique to solve radiotherapy physics problems. Major emphasis is given here to the ETRAN and EGS codes, since one gains insight into the general technique by understanding the differences in these codes and, perhaps more importantly, because most future applications and developments should be built on the many years of effort already invested.

II. Monte Carlo Codes

II.A. OVERVIEW: THE MONTE CARLO TECHNIQUE

II.A.1. What Is Monte Carlo?

Monte Carlo techniques are used in a wide range of scientific endeavors and the term has a variety of different meanings (see, for example,

Shreider, 1966). In the context of radiation transport, Monte Carlo techniques are those which simulate the random trajectories of individual particles by using machine-generated (pseudo-)random numbers to sample from the probability distributions governing the physical processes involved. By simulating a large number of histories, information can be obtained about average values of macroscopic quantities such as energy deposition. Moreover, since one follows individual particle histories, the technique can be used to obtain information about the statistical fluctuations of particular kinds of events. It is also possible to use the Monte Carlo technique to answer questions which cannot be addressed by experimental investigation, such as “What fraction of these electrons were generated in the collimator versus the filter?” or “How often have certain photons undergone Compton scattering?”

In contrast to Monte Carlo methods, there are various analytic approaches for solving the radiation transport equation. Because of the complex nature of electron transport, most analytic solutions require many simplifying assumptions. The early work in this field has been reviewed by Berger (1963). While analytical techniques have made important contributions to our understanding of electron transport, they are incapable of dealing accurately with the vast majority of problems of interest today. However, there has been considerable recent progress in applying the deterministic method of discrete ordinates to electron-photon transport calculations (see, e.g., Morel and Lorence, 1986). This technique may play a significant role in the future, depending on just what speed can be obtained in practical situations. However, since the technique solves the transport equation directly, it is not capable of answering questions about an individual particle's history in as direct a manner as the Monte Carlo technique.

In Monte Carlo simulations of electron transport it is time-consuming to simulate each interaction individually because an electron undergoes a large number of elastic scatterings from nuclei during its history. Also, in the course of slowing down, a large number of low-energy “knock-on” electrons are set in motion and many atoms are left in excited states. These problems are made tractable by using the condensed-history technique (Berger, 1963), in which the path of the electron is broken into a series of steps for which the effects of the large number of individual interactions occurring during the step are grouped together. One grouping accounts for the large number of deflections caused by elastic scattering. This uses a multiple-scattering theory such as that of Moliere (1948) or of Goudsmit and Saunderson (1940). The other major grouping accounts for the large number of small energy losses through the use of a continuous slowing-down model. Monte Carlo codes can be divided into two broad

categories, called class I and class II by Berger (1963). These are distinguished by how they treat individual events that lead to bremsstrahlung photons and/or knock-on electrons. In class I models, the energy losses and angular deflections associated with all individual events are grouped together and the energy and direction of the primary electron are not affected by the creation of individual secondary particles. In class II models, individual interactions affect the energy and direction of the primary electron when they create knock-on electrons or bremsstrahlung photons above certain energy thresholds, although the effects of secondary particle production below these thresholds are still grouped together. The distinctions between these two classes are dealt with in detail in Section II.A.5.

II.A.2. Photon, Electron, and Atomic Processes

It is certainly a necessary, if not sufficient, condition that one takes into account accurately all the relevant physical processes in electron-photon transport if the Monte Carlo technique is to provide an accurate simulation. In this section we enumerate the processes which affect simulations in the range from a few kilo-electron-volts to tens of mega-electron-volts. In Section II.B we review how the interaction cross sections vary with energy and atomic number in order to make clear which processes are relevant in a given simulation. Detailed formulas for cross sections and angular distributions are left to code documentation and textbooks.

a. Photons. As a photon passes through matter it can experience a variety of interactions. For energies of the order of 1 MeV, the most common event is a Compton interaction (also called incoherent scattering), in which the photon scatters from an electron and sets it in motion. In many calculations it is adequate to consider this electron as free, but at lower energies the cross sections are affected by the fact that the electron is initially bound in an atom. The Compton event also leaves a “hole” in the atom which must be filled (see a discussion of atomic effects below).

At photon energies above a few mega-electron-volts, pair production begins to dominate the photon interactions. In this case the photon interacts with the field of the nucleus, is absorbed, and creates an electron-positron pair. Much less frequently the photon may interact with the field of an atomic electron. Unlike pair production in the field of the nucleus, the original electron can take up a considerable amount of energy in this process and hence it is referred to as triplet production (e^- , e^- , and e^+). A vacancy is left in the atom.

At lower photon energies the predominant photon interaction is the photoelectric effect, in which the photon is absorbed by the atom and a photoelectron is ejected, once again leaving a vacancy in the atom, usually in the K shell.

The last major photon interaction is Rayleigh (or coherent) scattering, in which the photon scatters elastically from atoms, molecules, or other structures in the material. No energy is lost by the photon except for a negligible amount to the atomic recoil.

Several other photon processes can occur. One is the quite rare double-Compton effect, in which a second photon appears when a photon scatters from an electron. Although the process is usually not modeled, the so-called Mork correction includes this effect in the total Compton cross section. Two other processes, which are usually ignored completely, are nuclear Thompson scattering, in which the photon scatters elastically from the nucleus (i.e., low-energy nuclear Compton scattering), and Delbruck scattering, in which the photon scatters elastically from the Coulomb field of the nucleus. In photonuclear reactions the nucleus absorbs a photon and gives off a nucleon. The predominant reactions are (γ, n) and (γ, p) , which have a “giant resonance” centered at roughly 12 MeV for heavy nuclei and 24 MeV for light nuclei. The cross sections for these reactions are never more than 10% of the total photon cross section and usually much less (see, for example, Hubbell, 1969; Ahrens et al., 1975; Berman, 1976; Fuller and Gerstenberg, 1978). These reactions are rarely important in radiation dosimetry calculations for two reasons. One is that the photon mean free paths are usually large relative to the geometries of interest so that the small increase in attenuation has only a minor effect. Second, the (γ, n) cross section often dominates over the (γ, p) cross section (especially for high- Z materials), and the neutron results in energy deposition only after another nuclear interaction occurs, thus spreading out an already small effect. On the other hand, for radiation shielding calculations the neutrons may be transported farther than the original photons and thus dominate leakage through the shield.

b. Electrons. As electrons and positrons pass through matter they can often be thought of as continuously losing energy via inelastic collisions with bound atomic electrons. This can give rise to various possibilities, ranging from an excited atomic state to a high-energy knock-on electron which leaves behind a vacancy in the original atom. The creation of knock-on electrons above a specified threshold energy may be considered separately. For electrons it is usually modeled using the inelastic Moller cross section, which treats both electrons as free. The maximum energy transfer to the knock-on electron is one-half of the initial energy

since, by convention, the knock-on electron is taken to be the one with the lower energy. For a positron, the creation of knock-on electrons is modeled using the Bhabha cross section. The two particles are distinguishable in this case, and hence knock-on electrons may have energies up to the initial positron energy.

Slowing electrons may also lose energy by radiative processes whereby an incident electron (or positron) interacts in the field of a nucleus to produce a photon. As in the case of knock-on electrons, the creation of bremsstrahlung photons can be considered to have two components: (1) a continuous process in which the electron produces soft photons below a threshold photon energy and (2) discrete events which create bremsstrahlung photons above the same photon energy threshold. Although it is unlikely, an electron or positron can lose all of its energy to the bremsstrahlung photon it produces.

A slowing or stopped positron can also lose energy by annihilating in a collision with an electron. At rest, its annihilation creates a pair of 511 keV photons. Annihilation in flight also leads to two photons which share the total energy of the positron and electron.

The final major interaction of slowing electrons and positrons is elastic scattering from atomic nuclei. In the types of Monte Carlo calculations discussed here, this process is usually treated using multiple-scattering theories. In transport simulations for electrons with initial energies of tens of kilo-electron-volts or less, this process can be simulated as a series of discrete events, but for higher energies the number of such events becomes prohibitive. For example, Berger and Wang (1989) estimate that electrons undergo 4000 elastic scatterings in slowing from 500 to 250 keV in aluminum or 7000 scatterings in gold. To handle this situation, most electron transport algorithms use a condensed-history technique in which the electron is followed in a series of steps, and a multiple-scattering theory is used to group individual elastic scattering events which occurred during the step. *c. Atomic.* In many of the processes described above, one product is an atom from which an electron has been removed, usually from the K shell. These vacancies are then filled by electrons from higher shells with the attendant creation of fluorescent x rays or Auger electrons. The fluorescence yield indicates how often an x ray is produced, instead of an Auger electron, as these vacancies are filled. Its value is small for low- Z materials and over 90% in the K shell for materials with $Z \geq 60$. The higher-shell vacancies created in this process are also filled. This “relaxation process” can be very complex. In general, however, the resultant x rays and Auger electrons are of very low energy unless the original vacancy was in the K shell.

II.A.3. Photon Transport

Figure 1 presents a flow diagram for a Monte Carlo simulation of photon transport. The word DETERMINE in the diagram symbolizes an important concept. At each of these points one makes use of detailed knowledge of the physical processes involved in photon transport and, by

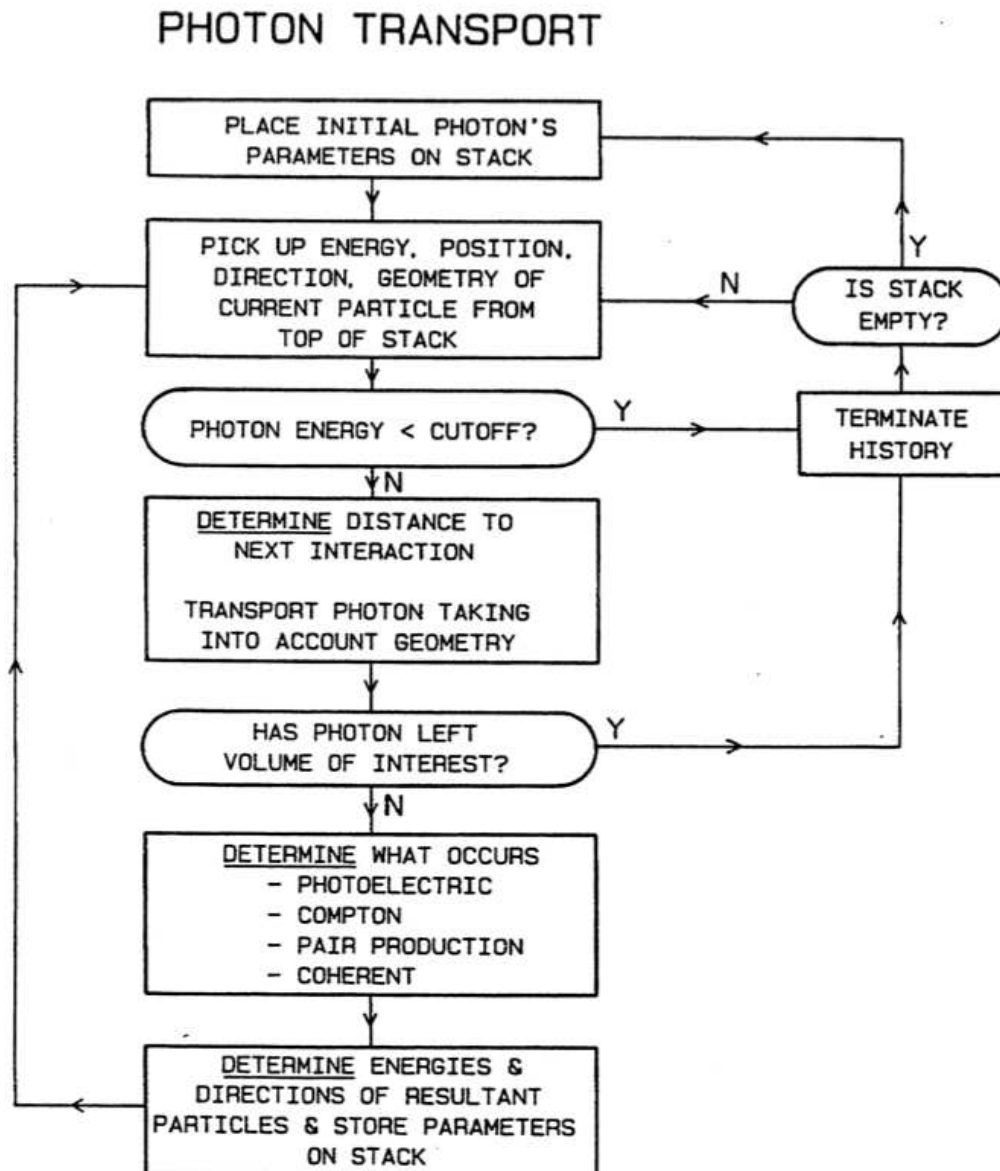


Figure 1: Logic flow of a Monte Carlo simulation of photon transport. DETERMINE means that the quantities of interest are found by sampling from the relevant probability distribution using one or more random numbers.

sampling from an appropriate probability distribution, determines the parameters of the event. In the next section we discuss more specifically how this is done.

Another concept introduced by Fig. 1 is that of a “stack” of particles. This is merely a procedure for storing the necessary phase space parameters of particles generated during the simulation so that they can be processed later. The stack is essential because at each photon interaction it is possible to create one or more additional particles (electrons, positrons, fluorescent x rays, etc.) and one must store the phase space parameters for each particle so that it can be processed in turn. This procedure is possible because at any point in the simulation the future of a photon or an electron is independent of its previous history.

Photon histories are terminated because the photon has been absorbed, the energy of the photon falls below a cutoff and we are no longer interested in it, or the photon leaves the geometric volume of interest. The details of what to do when the history is terminated and how to define the energy cutoff depend on what quantities are of interest in the calculation.

This raises the point that Fig. 1 shows only an algorithm for simulating the photon transport. This would be of little interest by itself since nothing is “scored.” By scoring a physical quantity of interest we mean monitoring selected aspects of the transport process and keeping track of items of interest to us. For example, if we are interested in absorbed dose we score the energy deposited by interactions in a particular geometric region. The most efficient way to score various quantities of interest is discussed in Sections II,D and IV.

II.A.4. Sampling a Physical Process

The inherent nature of virtually all the processes involved in particle transport is random. At best, our knowledge of each process amounts to knowing the probability distributions governing the event. For example, knowledge of the total cross section of a photon in a material does not tell us how far it goes in the material but only the mean value of its path length prior to an interaction. We also know that the path lengths are distributed exponentially. Similarly, differential cross sections give us the probability that a process may occur as a function of some final-state variable (e.g., energy or angle). Thus an essential element of any Monte Carlo simulation is the ability to sample the various probability distributions which describe the physical processes involved and to simulate the random nature of these individual events. This can be a very complex task. Fortunately, much work has been devoted to the subject, so accurate and

efficient algorithms exist for sampling from all frequently used distributions (e.g., the Klein-Nishina differential cross section for Compton scattering). For some of the less frequent processes, various approximations are introduced and/or the sampling routines become inefficient, but these have little effect on the overall timing or accuracy of the simulation because they are used so infrequently. Ford and Nelson (1978) have given a general introduction to sampling methods and a thorough review of all those utilized in the EGS code (a slightly revised version is reprinted in Nelson et al., 1985). Other general references are available (Kahn 1956; Butler, 1956; McGrath and Irving, 1975; Carlsson, 1981).

The general problem of sampling can become complex. Ford and Nelson require more than 22 typeset pages and 109 equations to derive their sampling formulas for the complementary bremsstrahlung and pair production differential cross sections! One can generally use previously written sampling routines. Nonetheless, it is instructive to review an example. Consider a simple photon transport model which includes only Compton scattering and pair production events, with the cross section at a given energy (in reciprocal centimeters)

$$\Sigma_{\text{tot}} = \Sigma_{\text{Compton}} + \Sigma_{\text{pair}}$$

The questions at hand are how far a given photon goes before interacting and which interaction occurs, that is, how do we implement the first two DETERMINEs in Fig. 1? The procedure begins with the selection of two random numbers R_1 and R_2 uniformly distributed between 0 and 1 (see Section II.E). Since we know that the path lengths of the photons are exponentially distributed, we must sample from an exponential distribution having a mean path length given by Σ_{tot}^{-1} . Any of the above references prove that the variable

$$x = -\frac{1}{\Sigma_{\text{tot}}} \ln R_1 \quad (\text{cm})$$

is exponentially distributed between zero and infinity with a mean value of $1/\Sigma_{\text{tot}}$. We have thus DETERMINED that this photon will go a distance x cm and then interact. We can then DETERMINE which type of interaction occurs by selecting a Compton interaction if $R_2 \leq \Sigma_{\text{Compton}}/\Sigma_{\text{tot}}$ and a pair interaction otherwise. These are the two simplest but most often used sampling routines in Monte Carlo simulations.

II.A.5. Class I and Class II Models and Thresholds for Discrete Events

Berger (1963) divided electron transport algorithms into two broad classes distinguished by how the energy of the primary electron is related to the energy lost in individual interactions. In class I models, the effects on the primary electron of all interactions of a certain type are grouped together for each condensed-history step. Class II models group the effects of only a subset of the interactions for each type and treat the effects of the remaining interactions on an individual basis. For example, for collisional energy loss a continuous energy-loss model is used which groups together the effects of all interactions that produce knock-on electrons with energy below some arbitrary threshold energy. Individual treatment is given to those relatively rare “catastrophic” interactions which create secondary particles above the same arbitrary energy. These discrete interactions cause the primary electron to lose energy and be deflected. The choice of the energy thresholds for considering the creation of secondary electrons or photons as discrete events is arbitrary and a component of the algorithm, not of the physical processes involved.

One simple form of electron Monte Carlo calculation is the continuous slowing down approximation (CSDA) model in which no secondary particles are produced and the unrestricted total stopping power is used to account for the energy loss in each step. The name arises because the electron is thought of as continuously losing energy along its path, although the algorithm takes finite steps and the energy appears to drop in discrete steps. In the CSDA model, all angular deflections are treated using a multiple-scattering theory. The CSDA model is clearly a class I algorithm.¹ However, class I algorithms can be sophisticated enough to include the generation of secondary particles and account for energy-loss straggling. ETRAN’s treatment of knock-on electrons is done using a class I algorithm.

Class II algorithms are, in principle, more accurate than class I because correlations between primary and secondary particles are included. However, these correlations are significant in only a few very specialized circumstances (see Section II,G,1). Since EGS uses class II algorithms and ETRAN uses a class I algorithm, it is worthwhile to examine the differences between these two classes of algorithms in order to elucidate how EGS and ETRAN, and many other codes, work.

Table I summarizes some definitions of energy cutoffs and production thresholds. Energy cutoffs are used in both class I and class II algorithms, whereas the production thresholds apply only to class II algorithms. Electron interactions which create secondary particles with energies below

¹This statement was misleading. Since CSDA models create no secondary electrons, the distinction between class I and class II has no meaning.

Table 1:
DEFINITIONS OF ENERGY CUTOFFS AND THRESHOLDS

	Electrons or positrons	Photons	Meaning
Energy cutoffs	ECUT	PCUT	Particle histories are terminated for particles with kinetic energies below these values
Production thresholds	AE	AP	The production by electrons of secondary particles with kinetic energy greater than these values is modeled explicitly
	AE' ECUT'		Same as above but for total energies (including rest mass of electron).

these thresholds are grouped together with other elastic and low-energy loss events and considered part of a continuous process. The continuous part of the energy loss is modeled using what is called the restricted stopping power. This is the part of the stopping power restricted to creating secondary particles with energies less than the thresholds, AE and AP (see Table I), and hence is a function of AE and AP (see Section II,B,2).

Elastic electron scattering from atomic nuclei is treated using a multiple-scattering formalism. Any such formalism which takes into account scattering from the atomic electrons as well as from the nucleus should, in principle, be dependent on AE, the threshold for considering knock-on electron production separately. This is not usually the case, which leads to (a usually unimportant) double counting of these scatterings. Andreo and Brahme (1984) used another variation in which elastic scatterings causing large deflections are treated as discrete events and the remainder of the multiple scattering is simulated using a Gaussian model.

Figure 2 depicts electron transport in a class II algorithm. In the model the electron moves in short, straight steps. For each step, a multiple scattering theory is used to select the angle through which the electron is deflected. The multiple-scattering theory should also be used to account for the true path length of the particle during the step. From this true path length one can deduce the amount of energy lost via continuous processes, including the creation of knock-ons with energy below AE and bremsstrahlung photons with energy less than AP. Although the energy deposited by these low-energy particles is distributed throughout the shaded area about the path, in the model it is considered to be deposited

DISCRETE AND CONTINUOUS ENERGY LOSS

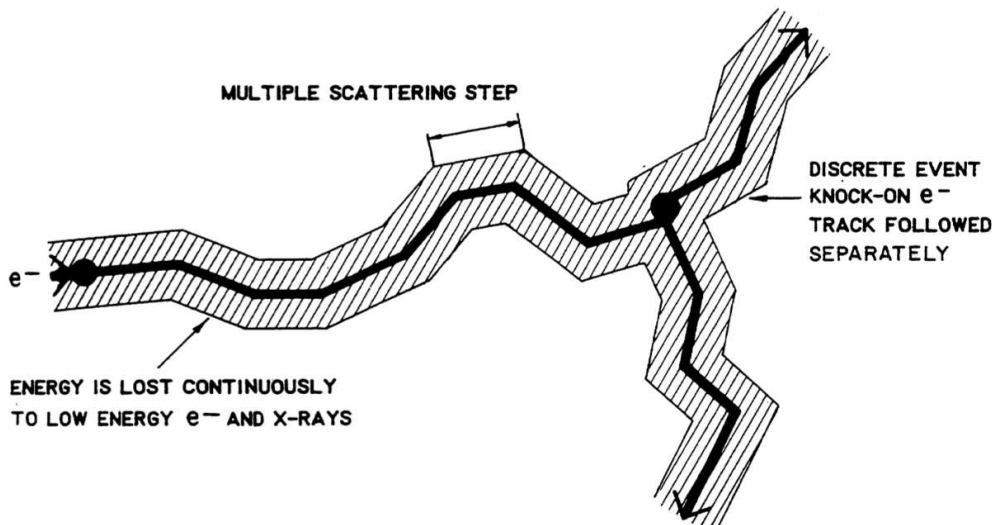


Figure 2: In a class II algorithm, the energy loss and deflection of the slowing electrons are broken into two components. The continuous energy loss is considered to occur along the straight-line path but in reality includes energy deposition throughout the shaded area by secondaries with energies less than the production thresholds AE and AP . Multiple scattering is taken into account by a deflection in each small step. Discrete interactions create knock-on electrons with energies above AE or bremsstrahlung photons with energies above AP .

on the path itself. After going distances governed by the appropriate cross sections, the electron undergoes a discrete interaction and creates a secondary particle above the production threshold (AE or AP). The secondary particle is also tracked. The energy of the primary electron is decremented during the discrete interaction by an amount corresponding to the energy of the secondary particle. This usually excellent approximation ignores the binding energy of electrons knocked out of a molecule and any energy taken up by the nucleus or electron when a bremsstrahlung photon is created.

II.A.6. Energy Loss in a Thin Slab of Water

It is instructive to consider the results of a variety of models for a pencil (zero area) beam of 20-MeV electrons incident normally on a 0.25cm-thick semi-infinite slab of water.

In a CSDA model, to first order, all the electrons pass through the slab and lose the same amount of energy in continuous processes. This energy

is given by the product of the slab thickness and the total unrestricted stopping power for 20-MeV electrons in water and amounts to 618 keV or 3.1 % of the initial energy. At the same time, the electrons have been deflected slightly by elastic scattering from the hydrogen and oxygen nuclei and by scattering from the electrons in the water. Figure 3 shows the angular distributions behind the plate of water as calculated (see Appendix A) by the Moliere multiple-scattering formalism in EGS and the Goudsmit-Saunderson multiple-scattering formalism in ETRAN/CYLTRAN. Figure 3 shows that 96% of the electrons are deflected less than 9° . These angular deflections have little effect on the path length or on the energy lost passing through the slab. This lack of effect on the average path length through the slab is why this configuration was chosen as an example.

In the CSDA model used in the example above, both EGS (somewhat modified) and ETRAN were using a class I algorithm to model the electron²

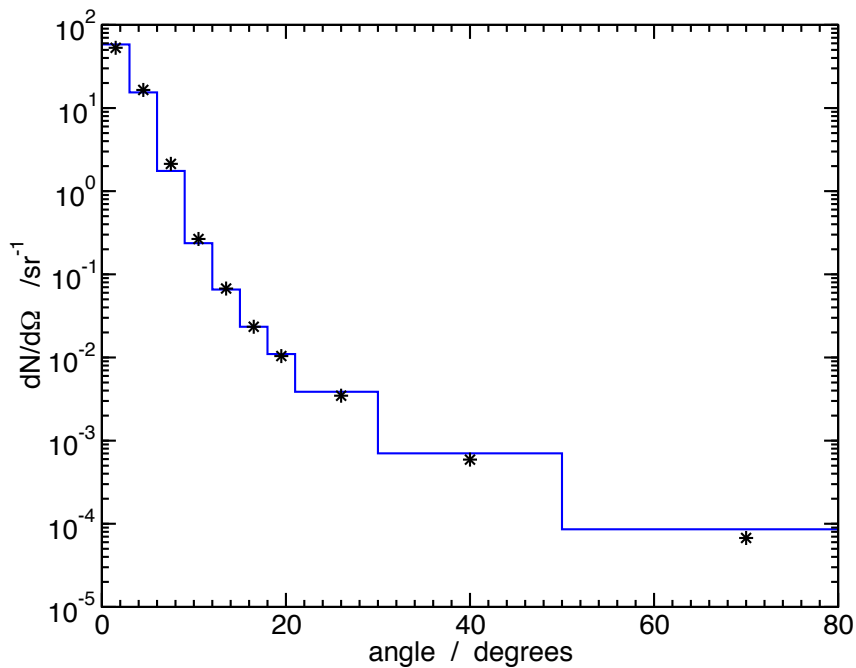


Figure 3: Calculated angular distribution of the electrons after an incident pencil beam of 20-MeV electrons passes through a 0.25-cm-thick slab of water. A CSDA model with no secondaries was used in both cases. The EGS calculation (histogram) uses the Moliere multiple-scattering formalism and the CYLTRAN calculation (stars) uses the Goudsmit Saunderson multiple-scattering formalism. Statistical uncertainties are less than the size of the stars.

²It is meaningless to talk of Class I when no secondaries are being created.

transport. Let us now consider a class II algorithm in which knock-on electrons with a kinetic energy of 1 MeV or greater are created. Energy losses and angular deflections from two sources are considered: the continuous events and the discrete events that create knock-on electrons with energies greater than 1 MeV. These discrete interactions are relatively rare; only 2.1% of the 20-MeV electrons experience one while traversing the 0.25-cm slab of water. However, to allow for the energy loss that occurs during these events, the continuous energy loss must be calculated using a restricted stopping power. The unrestricted stopping power of 2.47 MeV cm^{-1} is reduced to a restricted stopping power of 2.24 MeV cm^{-1} by excluding the creation of knock-ons of energy greater than 1 MeV. Thus, when using this class II algorithm, the 97.9% of the electrons that go through the water slab without creating a secondary electron lose slightly less energy (560 keV) than those in the CSDA calculation (618 keV). On the other hand, the electrons which do create a knock-on with energy greater than 1 MeV must themselves lose at least 1 MeV, in addition to the energy loss due to the continuous processes. As seen by the stars in Fig. 4, this leads to an energy spectrum with a 1-MeV gap below the electrons that do not create knock-ons and a distribution from that threshold down to a cutoff at 9.7 MeV. This lower cutoff occurs because the primary electron and knock-on electron are identical particles, and by convention the primary electron can lose only one-half of its energy when creating a knock-on. For incident positrons the distribution would extend to zero energy.

Despite the significant differences in the energy distributions of the electrons coming through the plate in the two models, the mean energy loss is the same. The additional losses due to the discrete events are exactly compensated by the reduction in the continuous energy loss. Although the class II model explicitly accounts for deflections of the primary when knock-ons are created, the number of such events and the size of the deflections are generally so small that the calculated angular distribution of electrons coming through the plate is unchanged.

Let us now consider a second class II calculation in which no knock-on electrons are explicitly created but the production of bremsstrahlung photons with energies greater than 100 keV is accounted for explicitly. In this case roughly 4% of the electrons create a photon and the appropriate restricted stopping power of 2.05 MeV cm^{-1} implies that the electrons lose 514 keV via continuous processes while passing through the plate. Since an electron can give anywhere from 100 keV to all of its energy to a bremsstrahlung photon, the results with this model (diamonds in Fig. 4) show a continuous distribution of electron energies from essentially zero energy to within 100 keV of the continuous-energy-loss peak. Once again

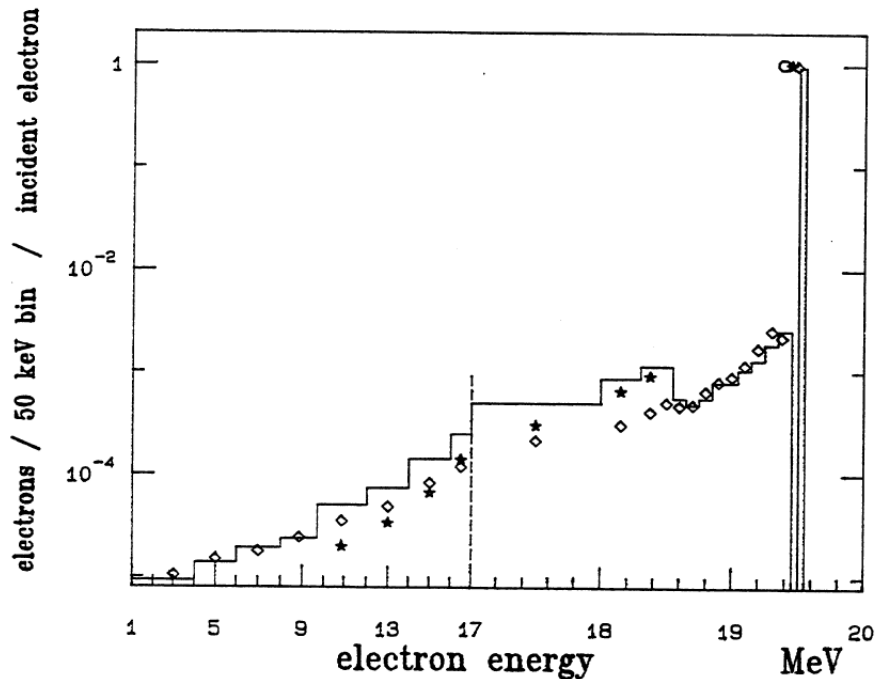


Figure 4: Energy distribution of primary electrons, calculated by a variety of algorithms when a beam of 20-MeV electrons passes through a 0.25-cm slab of water. Circles, Class I, CSDA calculation³; stars, a class II calculation that explicitly considers only knock-on electrons above 1 MeV ($AE = 1$ MeV); diamonds, a class II calculation with bremsstrahlung photons above 100 keV; histogram, calculation creating knock-ons and bremsstrahlung photons. In all cases the mean energy loss was $618 \text{ keV} \pm 1\%$. Note that the energy axis changes scale at 17 MeV.

the mean energy loss is the same and, to first order, the angular distribution is identical to that obtained by the CSDA calculation because EGS does not deflect an electron when it creates a photon. (In second order, the electrons which create photons are lower in energy and scatter more, but this has a negligible effect on the angular distribution.)

The third class II model shown by the histogram in Fig. 4 allows for creating knock-ons with energies greater than 1 MeV and bremsstrahlung photons with energies greater than 100 keV. The restricted stopping power of 1.83 MeV cm^{-1} implies that the 94% of the particles that do not experience a discrete interaction lose only 456 keV in the slab. The energy distribution shows two thresholds, 100 keV and 1 MeV below the continuous-energy-loss peak.³

All of the above models of the passage of incident 20-MeV electrons through 0.25 cm of water correctly predict the angular distributions and

³It was incorrect in the caption to call a CSDA calculation a Class I calculation as no secondaries are created. It may be acceptable if the energy loss were being sampled from a straggling distribution, but that is not the case here.

mean energy losses. However, none of them accurately models physical reality since the production thresholds of 1.0 and 0.1 MeV and the corresponding thresholds in the electron spectrum have no physical significance. The true energy spectrum of electrons emerging from the plate is a continuous distribution. If this were the feature of interest in our calculation, we would be forced to use very small values of AE and AP. Figure 5⁴ presents the results of one such calculation using $AP = AE = 1$ keV. Here the straggling of the energy loss has been modeled by calculating explicitly the many random events which create knock-ons. On average, each primary electron created 21 knock-on electrons and the continuous energy losses represented only one-half of the total energy loss in the slab.

While this approach provides an accurate representation of the electron energy spectrum, it requires an inordinate amount of computing time. Andreo and Brahme (1984) have suggested a useful alternative class II scheme in which some reasonable value of AE is adopted and energy-

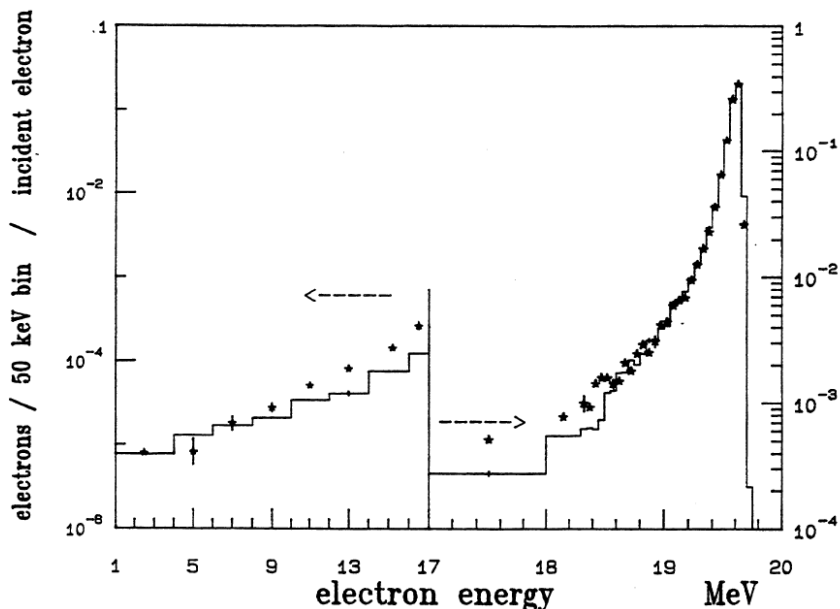


Figure 5: Energy-loss straggling distribution of primary electrons for a normally incident beam of 20-MeV electrons passing through a 0.25-cm slab of water. Stars, the class II calculation, done with EGS with $AE = AP = 1$ keV; histogram, a class II calculation⁴ done with CYLTRAN. The discrepancies between 10 and 18.3 MeV reflect numerical accuracy problems with the L(LB) distribution in CYLTRAN which have been corrected recently (see Seltzer, 1989).

⁴The caption incorrectly states that the CYLTRAN calculation is a Class II calculation. In fact it is a class I calculation.

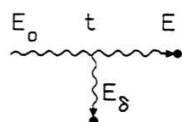
loss straggling from the creation of knock-ons with the energy below AE is handled by sampling a Gaussian energy-loss straggling distribution which smears out the energies of the continuous energy-loss component.

ETRAN and its descendants follow this approach even further and treat all energy losses caused by knock-on electrons as a continuous process; i.e., they use a class I algorithm. To account for the energy-loss straggling due to the creation of knock-on electrons, ETRAN uses the Blunck-Leisegang (1950) modification of the Landau (1944) energy-loss straggling distribution [which we call L(BL)]. At the same time, ETRAN does create knock-on electrons. Since the L(BL) distribution already decreases the energy of the primary electron to account for the creation of knock-on electrons, ETRAN does not further decrease this energy when the knock-on is created. Figure 5 presents the distribution of electron energies calculated by CYLTRAN (see Appendix A) for our 20-MeV beam of electrons on a 0.25-cm slab of water. The distribution is in fair agreement with the class II calculation described above, but the class I calculation takes much less time (for a further discussion, see Rogers and Bielajew, 1986; Seltzer, 1989).

II.A.7. Electron Transport

As a review of the distinctions between class I and class II models, consider Fig. 6, which, for simplicity, excludes radiative events. In the class II model, an electron of initial energy E_0 travels a distance t and then creates a knock-on electron of energy E_δ . Immediately after creating the knock-on, the energy of the primary electron is $E_0 - tL_{\text{col}}^{AE} - E_\delta$ where L_{col}^{AE} is the collision stopping power restricted to secondaries with energies less than AE and tL_{col}^{AE} is the energy lost in continuous processes and deposited along the path t . The creation of the knock-on causes the primary electron to change direction. The path would also have been deflected by multiple scattering, which is not shown in Fig. 6. In the class I model, the electron travels a step length t and creates an electron somewhere along the path. The energy at the end of the step is not explicitly affected by the creation of the knock-on electron but is decreased by sampling from an energy-loss distribution. This could ignore energy-loss straggling and would then be tS_{col} the path length times the unrestricted collision stopping power (radiative effects are ignored). To include energy-loss straggling one could sample the energy loss [denoted $\Delta E(t)$ in Fig. 6] from a straggling distribution such as the L(BL) distribution used by ETRAN. In either case, to conserve energy, one must subtract the energy of the knock-on electron to calculate the energy deposited locally because all secondaries have been accounted for in the $\Delta E(t)$ term. This

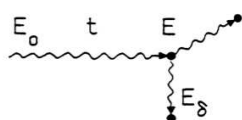
Class I
Uncorrelated Energy Loss



$$E = E_0 - \Delta E(t)$$

$$E_{\text{dep}} = \Delta E(t) - E_{\delta}$$

Class II
Correlated Energy Loss



$$E = E_0 - t L_{\text{col}}^{\text{AE}} - E_{\delta}$$

$$E_{\text{dep}} = t L_{\text{col}}^{\text{AE}}$$

Figure 6: Distinctions between the uncorrelated energy-loss mechanisms used in class I algorithms and the correlated energy-loss mechanisms used in class II algorithms. For simplicity, only discrete interactions creating knock-on electrons are considered. $\Delta E(t)$ is the energy loss sampled from an energy-loss straggling distribution and L is the restricted collision stopping power for secondaries below energy AE .

procedure is correct in principle, but it can produce unusual answers if not enough histories are used. In this class I algorithm, the creation of the knock-on electron does not explicitly affect the direction of the primary electron, although the multiple-scattering deflection associated with the step (not shown in Fig. 6) may at least attempt to account for these deflections.

Figure 7 presents a logic-flow diagram for electron transport simulations using either a class I or a class II algorithm. As in Fig. 1 for photon transport, this figure shows only the transport part of the code and additional logic would be required to score quantities of interest. The logic flow has been simplified in many respects in order to make the figure comprehensible.

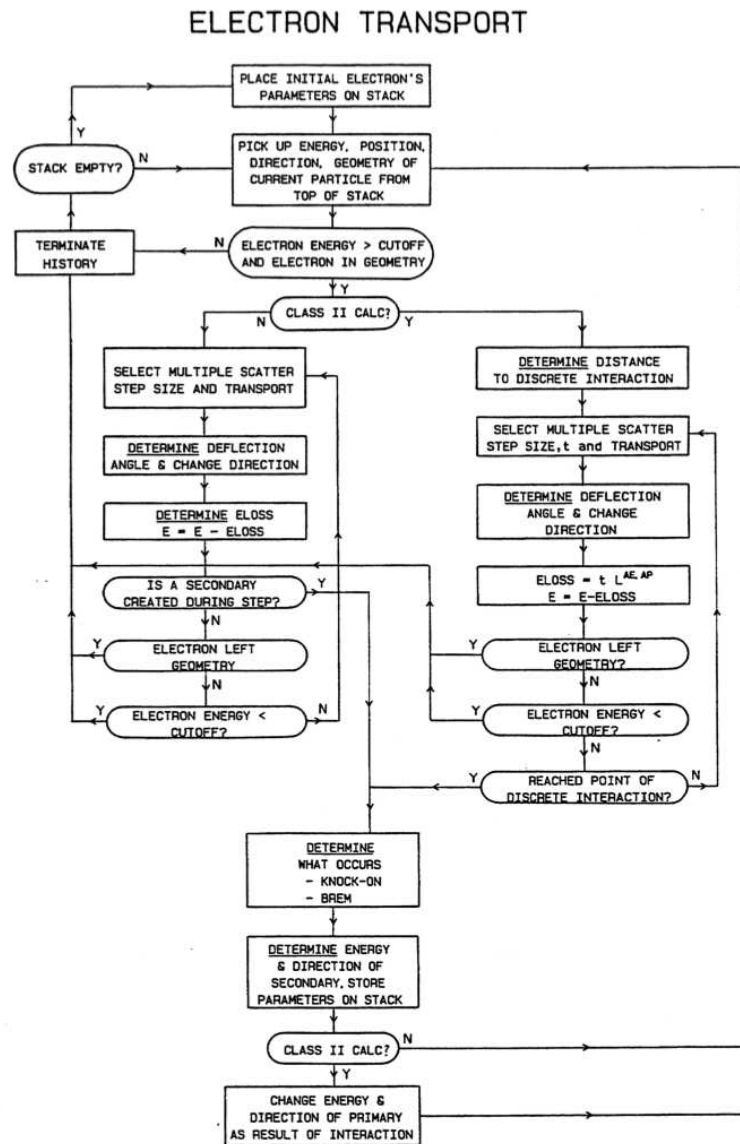


Figure 7: Logic flow for class I and class II Monte Carlo algorithms for simulating electron transport. DETERMINE has the same meaning as in Fig. 1. Many details of the simulation have had to be simplified. In most realistic calculations, the bulk of the computing time is spent in the multiple-scattering step loops near the middle of the diagram.

II.B. CROSS-SECTION DEPENDENCE ON ENERGY AND ATOMIC NUMBER

Numerous cross-section data are required in Monte Carlo calculations and a major part of any general-purpose code such as the ITS system or EGS is devoted to providing these data. This section presents a brief overview of the cross sections and their functional dependence on energy and atomic number. For more detailed information see, for example, the texts by Roy and Reed (1968), Anderson (1984), and Attix (1986), and the data compilations by Berger and Seltzer [1982a, also published as International Commission on Radiation Units and Measurements (ICRU) Report. No. 37, 1984b] and Hubbell (1969, extracts given by Evans, 1968). Uncertainties in these cross sections are discussed in Section III,A.

II.B.1. Photons

Figure 8 shows the various photon cross sections as functions of the atomic number Z for energies between 10 keV and 1.0 MeV. One notable feature is that the more or less straight lines on these log-log graphs indicate Z^n functional forms (except for the photoelectric effect, where absorption edges become important). The Compton effect goes exactly as Z^1 because the cross section based on the Klein-Nishina free-electron approximation was used to plot these graphs. The 10-MeV graph shows the Z^2 dependence of the pair production cross section. The difference in cross-section dependence for the Compton and pair processes means that at 10 MeV Compton scattering strongly dominates for low- Z materials, whereas pair production dominates for high- Z materials.

The photoelectric cross section has an even stronger Z -dependence, from $\sim Z^4$ to Z^5 , although the effect of absorption edges changes this for lower energies and higher Z . This very strong Z dependence of the photoelectric effect means that an admixture of even very small amounts of elements of high atomic numbers in low- Z material such as tissue can play an important role in low-energy simulations.

The functional dependence of coherent or Rayleigh scattering is complex, varying between Z^2 for small angles and Z^3 for large angles. The overall cross section is seen in Fig. 8 to vary as $Z^{2.4}$ at 10 keV and $Z^{2.7}$ at 100 keV.

Figure 9 presents the pair production cross section divided by Z^2 as a function of photon energy for hydrogen and uranium. It shows how little departure there is from the Z^2 dependence for this cross section and also that there is a monotonic increase with photon energy. The cross section for triplet production, which occurs in the field of the atomic electron, is

proportional to Z instead of Z^2 and so it is relatively more important for low- Z materials. Figure 10 shows that Z times the ratio of the cross sections for triplet and pair production is only mildly dependent on material and increases to between one-half and one for photon energies greater than 10 MeV where pair production is important. However, in the materials and energy range normally of interest in dosimetry, the triplet process plays a minor role. EGS treats it as if it were pair production; i.e., the pair production cross section is increased to account for the process, but only an e+-e-pair is created.⁵

Another perspective on the photon cross-section data is presented in Figs. 11 and 12, where the percentage contributions of the various processes to the total cross section are given as functions of photon energy for carbon and lead. For low- Z materials the Compton process dominates over a wide energy range and represents more than half the cross section from ~ 25 keV to 25 MeV for carbon. For high- Z materials the photoelectric and pair production processes play more significant roles. Compton scattering is more than half of the cross section only from ~ 600 keV to ~ 5 MeV.

Figures 11 and 12 emphasize the relative contributions to the total cross section, and this is what controls which interactions occur. However, one is often interested in energy deposition. In this case, the amount of energy lost by the photon in each interaction is important. The photon is completely absorbed in the photoelectric effect and in pair and triplet production, although some of the energy usually reappears as photons via bremsstrahlung emission, positron annihilation, or fluorescent x rays. However, in Compton scattering, the wavelength shift of the photon at a given angle is independent of the incident energy. Hence, as shown in Fig. 13, at low energies (large wavelengths) only a small fraction of the photon's energy is lost, on average, in each collision ($\sim 14\%$ at 100 keV), whereas at higher energies a larger fraction is lost ($\sim 50\%$ at ^{60}Co γ energies and 80% at 100 MeV). This means that low-energy photons in low- Z material can undergo many interactions before they lose much energy. For example, for a broad beam of 100-keV photons incident on a tissue phantom, 4% of the dose at the maximum of the depth-dose curve is due to photons which have Compton-scattered 10 or more times (Rogers, 1984b). Rayleigh scattering is an elastic process and causes no energy deposition. Since this cross section is generally forward peaked (especially for low- Z materials and higher energies) and since it generally constitutes 10% or less of the total cross section, its contribution to energy deposition can often be ignored, although its influence on the angular distribution of transmitted photons is noticeable (see, e.g., Johns and Yaffe, 1983).

⁵An option in EGSnrc now handles triplet production properly.

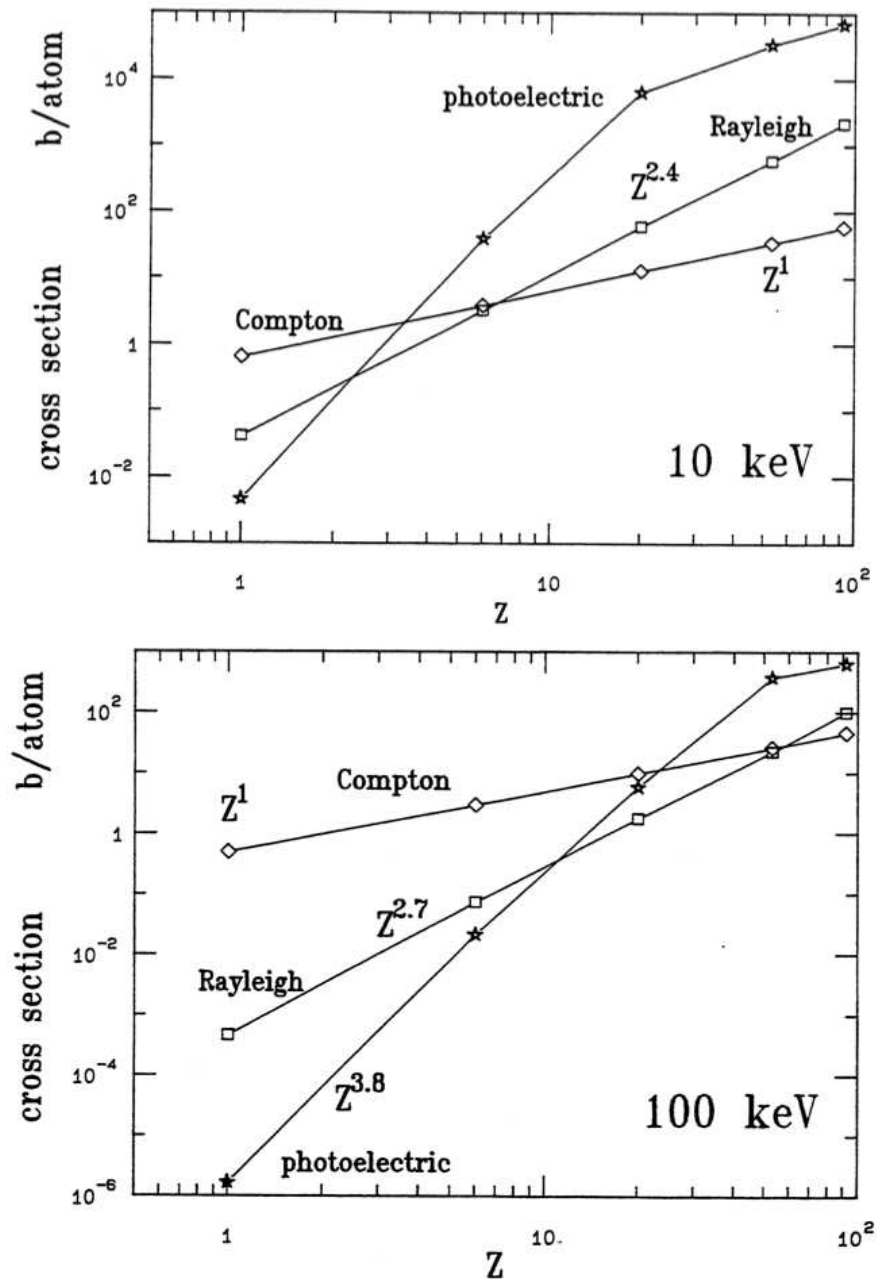


Figure 8: Photon cross sections as a function of atomic number Z for the photon energies shown. The photoelectric (stars), free electron Compton scattering (diamonds), and pair production (triangles) cross sections are from Hubbell (1969) and the Rayleigh data (squares) are from Hubbell and Overbo (1979). The Z dependences shown are based on simple fits to the data.

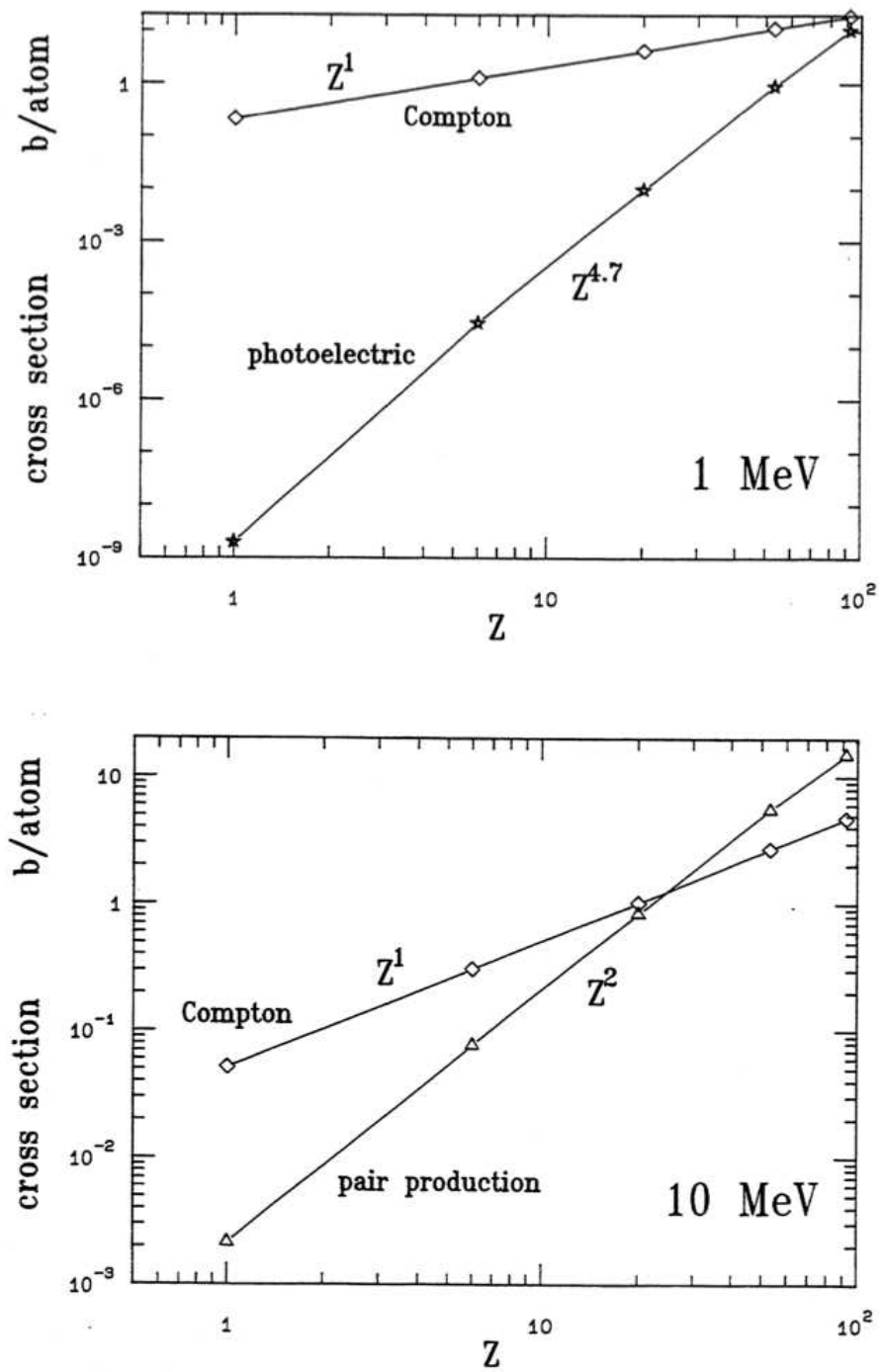


Figure 8: cont

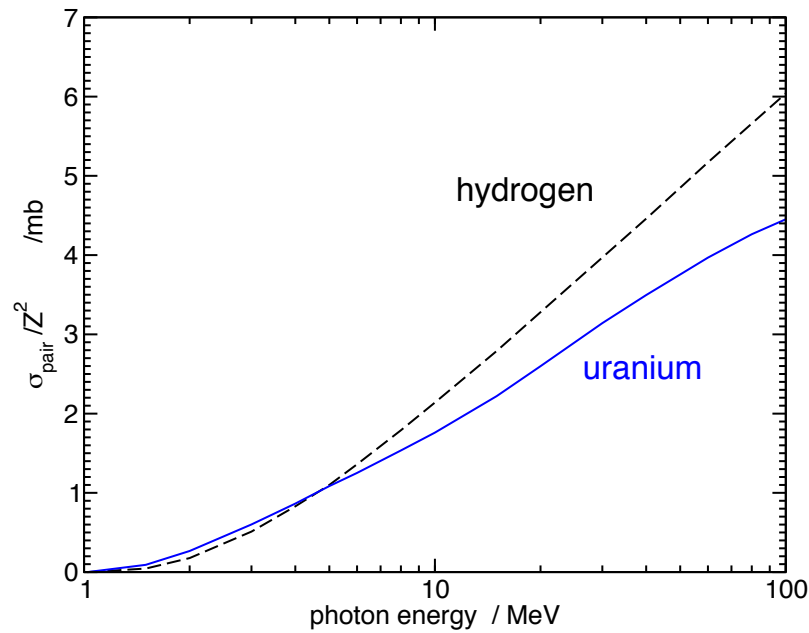


Figure 9: Pair production cross section σ_{pair} divided by Z^2 versus photon energy for hydrogen (dashed) and uranium (solid). The similarity of the curves indicates how closely the cross section scales as Z^2

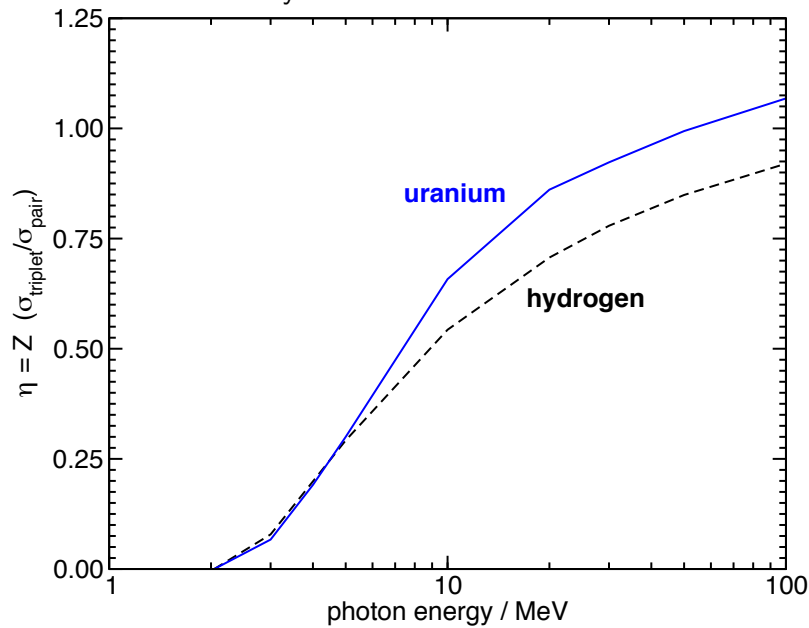


Figure 10: Z times the ratio of triplet (σ_{triplet}) to pair (σ_{pair}) production cross sections versus photon energy for hydrogen (dashed) and uranium (solid).

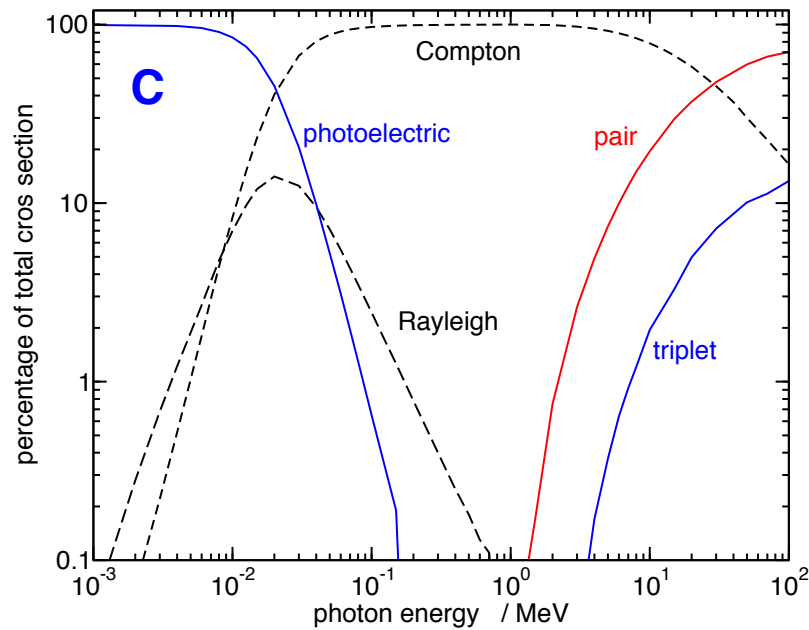


Figure 11: Percentage contribution of various photon interactions to the total cross sections of carbon as a function of photon energy. Data are taken from the EGS4 system (Nelson et al., 1985) and Hubbell (1969) for the triplet component.

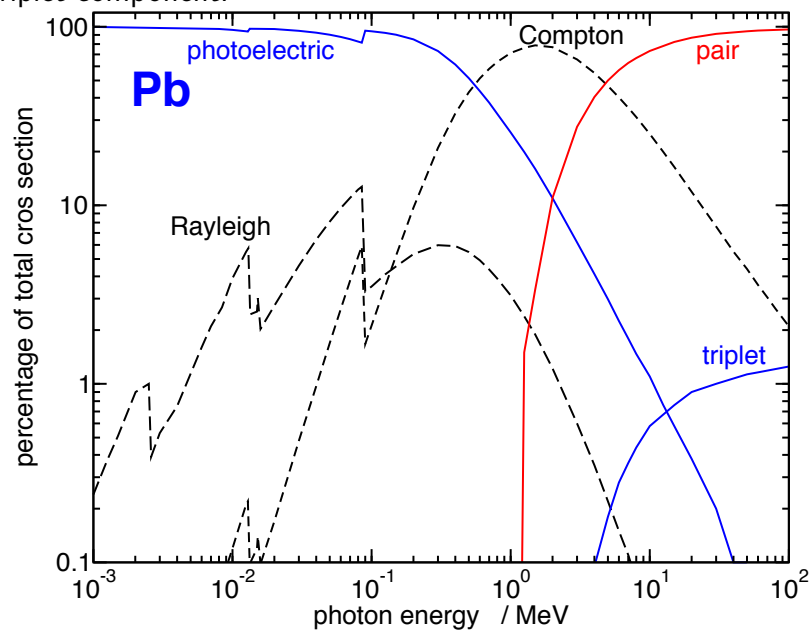


Figure 12: Percentage contribution of various photon interactions to the total cross sections of lead as a function of photon energy. Data are taken from the EGS4 system (Nelson et al., 1985) and Hubbell (1969) for the triplet component.

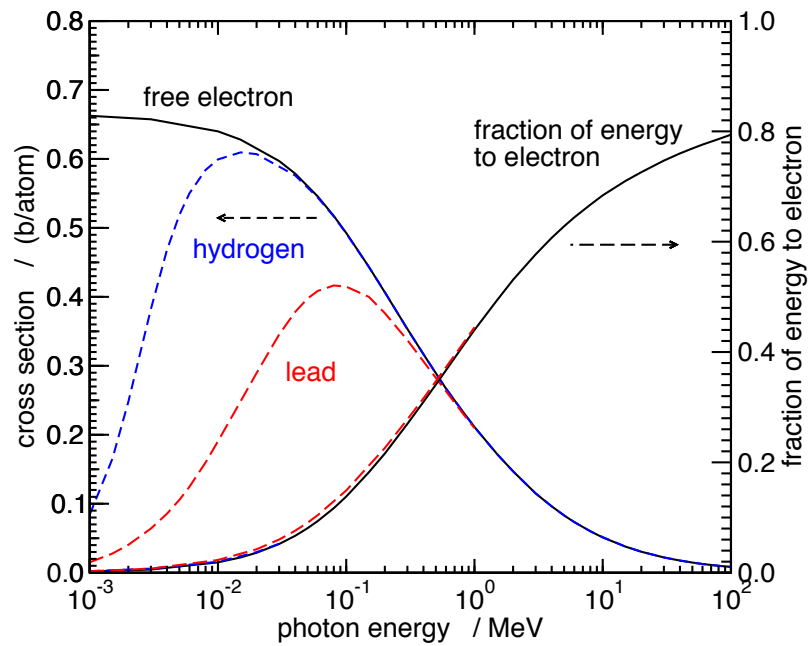


Figure 13: Compton cross section per electron for a free electron (solid) and for electrons bound in hydrogen or lead atoms (dashed) as a function of photon energy (data from Hubbell, 1969, and Hubbell et al., 1975). Also shown is the fraction of the photon energy which is transferred, on average, to electrons. The solid curve is for a free electron and the dashed curve for electrons from lead (data from Hubbell, 1969, and Veigle, 1973).

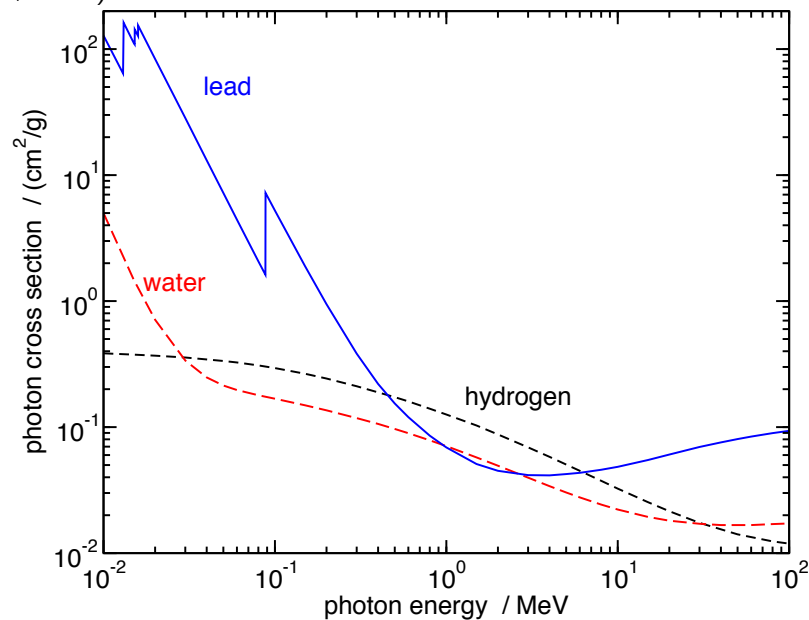


Figure 14: Total photon cross section versus photon energy for hydrogen (short dash), water (long dash) and lead (solid).

Figure 13 also compares the total Compton cross section per electron, assuming the electron is unbound, with that taking into account the atomic binding. It is clear that binding plays an important role at low energies. However, many codes use the free-electron assumption because the photoelectric effect usually dominates the cross section at these low energies.

Figure 14 compares the total photon cross section as a function of energy for hydrogen, water, and lead. Between 1 and 3 MeV the Compton process dominates and here the cross section is smallest for lead and largest for hydrogen because it is proportional to the electron density. Above and below this energy region the cross section for lead becomes significantly higher because the pair production and photoelectric cross sections increase much more rapidly for high- Z materials.

Any Monte Carlo code needs access to the cross sections, differential in angle, in order to simulate the physical processes. We will not review these here for reasons of space and because decisions about which processes must be accurately simulated in any given calculation are usually based on the total cross sections discussed above. The references cited for the total cross sections also discuss the differential cross sections.

II.B.2. Electrons and Positrons

The cross-section data required for electrons and positrons are somewhat complicated to discuss because class I and class II algorithms characterize the same data in different ways. In particular, for class II methods the data depend on the production thresholds for knock-on electrons and bremsstrahlung photons.

Figure 15 presents the unrestricted collision and radiative stopping powers as a function of electron energy for a variety of elements. The unrestricted collision stopping powers decrease by roughly an order of magnitude between 10 keV and several hundred kilo-electron-volts and then remain roughly constant between 1 and 2 MeV g^{-1}cm^2 at energies up to 100 MeV. The energy dependence is similar for the solid materials shown, whereas for gaseous argon the stopping power rises more quickly at higher energies because the density effect (Sternheimer and Peierls, 1971) does not reduce the higher-energy stopping powers as much for gases as for the higher-density solids. The radiative stopping power is strongly energy dependent, increasing slightly faster than linearly with the energy (above a mega-electron-volt or so). The radiative stopping power per atom also varies roughly as Z^2 like the bremsstrahlung and pair production cross sections).

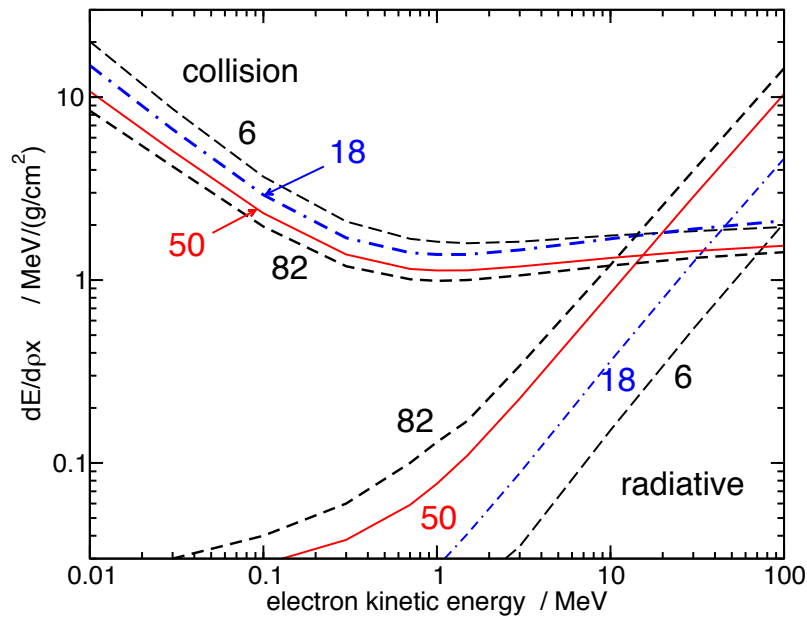


Figure 15: Unrestricted collision and radiative mass stopping powers versus energy for electrons in a wide variety of materials. Labels are atomic numbers: $Z = 6$, carbon; $Z = 18$, argon gas; $Z = 50$, tin; $Z = 82$, lead. Data are from Berger and Seltzer (1982a).

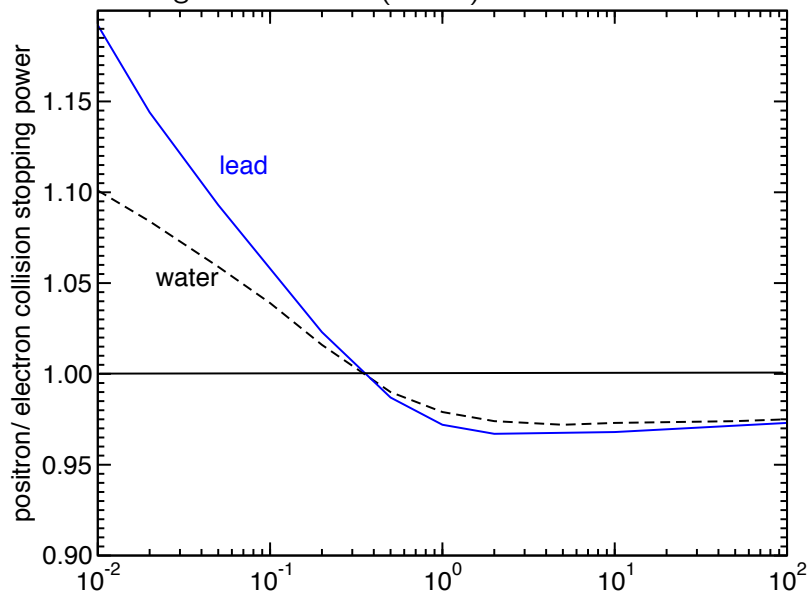


Figure 16: Ratios of positron to electron collision stopping power as a function of energy in water (dashed) and lead (solid). Data are from Berger and Seltzer (1982a).

Positrons have somewhat different stopping powers from electrons. For collisional losses this is because the Bhabha rather than the Moller cross section is involved and because a positron can lose all of its energy in a single collision, whereas, by convention, an electron can lose at most one-half of its energy. Figure 16 shows the ratio of the positron to the electron collision stopping power. At low energies and for high- Z materials the radiative stopping power for positrons can be significantly lower than that for electrons. Berger and Seltzer (1982a) proposed the universal curve shown in Fig. 17 to relate the scaled positron and electron radiative stopping powers caused by nuclear bremsstrahlung. The scaled stopping powers are given by $\phi_{\text{rad}}^{(n)}(E) \propto$ radiative stopping power/ $(E + m_e c^2)Z^2$. A more recent paper has discussed this curve fully (Kim et al., 1986). At 1 MeV, this implies that the positron radiative stopping power is lower than that for electrons by a few percent in carbon and by 60% in lead. These effects are not accounted for in current general-purpose Monte Carlo codes. Although they should not significantly affect any dosimetry applications, they could play a significant role in specialized applications involving positron beams.

Class II algorithms for electron transport consider the creation of secondary particles above energy thresholds in a discrete manner and creation of those below these thresholds using a continuous model and restricted stopping powers. Figure 18 shows the variation in the restricted collision stopping power for 2 and 20-MeV electrons in carbon and lead as a function of the maximum energy of the knock-on electron included in the restricted stopping power. There are several features to note. First, the restricted stopping power is equal to the unrestricted stopping power for maximum knock-on energies over one-half of the incident energy because no knock-ons above this energy can be created. Second, these curves are not dramatically dependent on Z or E . Third (and most important), even when restricted to knock-on electrons with energies less than 1 keV, the restricted stopping power makes up considerably more than 50% of the unrestricted stopping power; i.e., most of the collisional energy loss occurs in events which give up less than 1 keV.

Figure 19 shows a similar plot for the radiative stopping power. Here we note that (1) an electron can lose all of its energy to a single photon, (2) one-fourth to one-third of the radiative energy is lost to photons with energies greater than 50% of the electron energy, (3) the dependence on electron energy and Z is not strong, and (4) the restricted stopping power becomes negligible for low photon thresholds; i.e., virtually no radiative energy loss is due to creation of very soft photons. This last point means that by using a sufficiently small threshold for photon production one is, in fact, simulating the production of all bremsstrahlung photons.

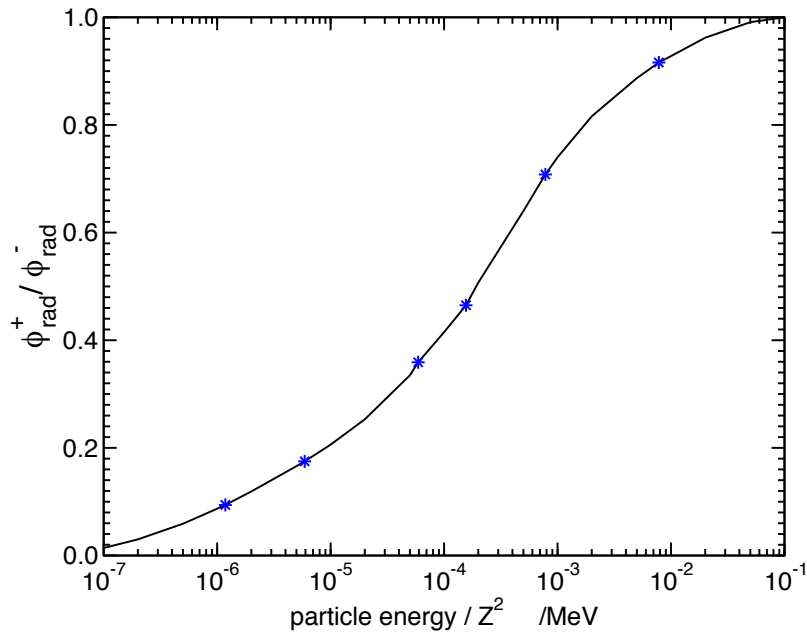


Figure 17: Ratio of scaled cross sections for the production of bremsstrahlung by positrons and electrons interacting with nuclei of different Z values. The curve is based on the very limited number of calculated points shown by stars. Data are from Berger and Seltzer (1982a).

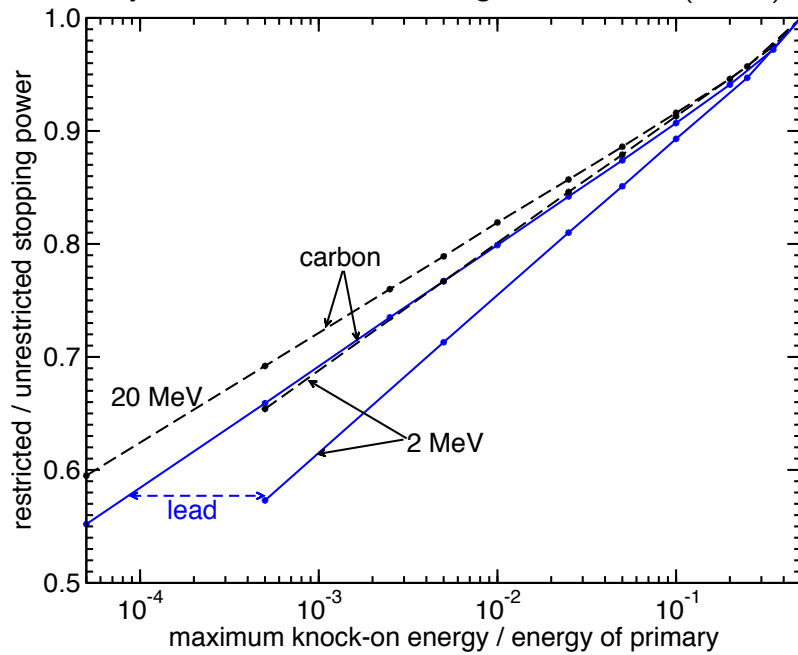


Figure 18: Ratio of the restricted to unrestricted collision stopping powers in carbon (dashed) and lead (solid) for 2- and 20-MeV electrons as a function of the maximum energy of knock-on electrons included in the restricted stopping power (as a fraction of the primary electron's energy). Data generated by the EGS4 system (Nelson et al., 1985).

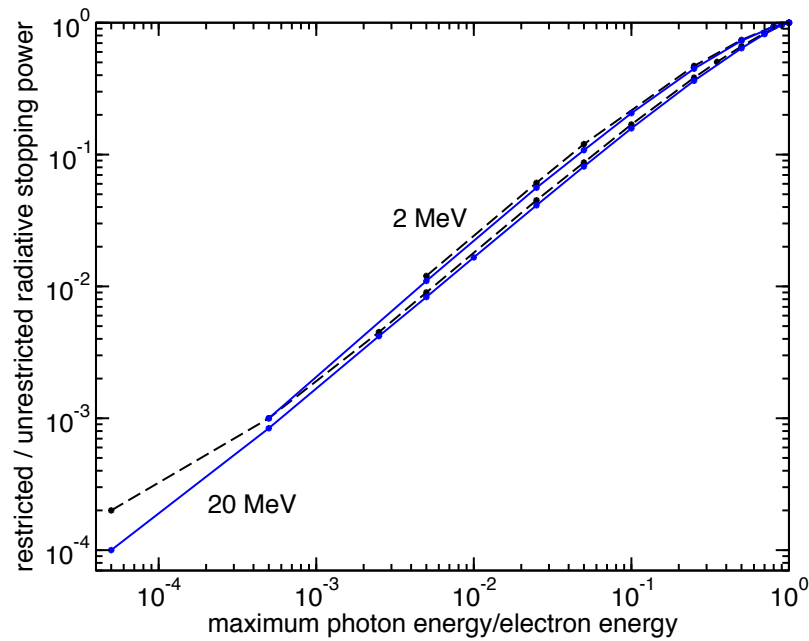


Figure 19: Same as Fig. 18 except for restricted radiative stopping powers. Dashed curves are for carbon, solid curves for lead.

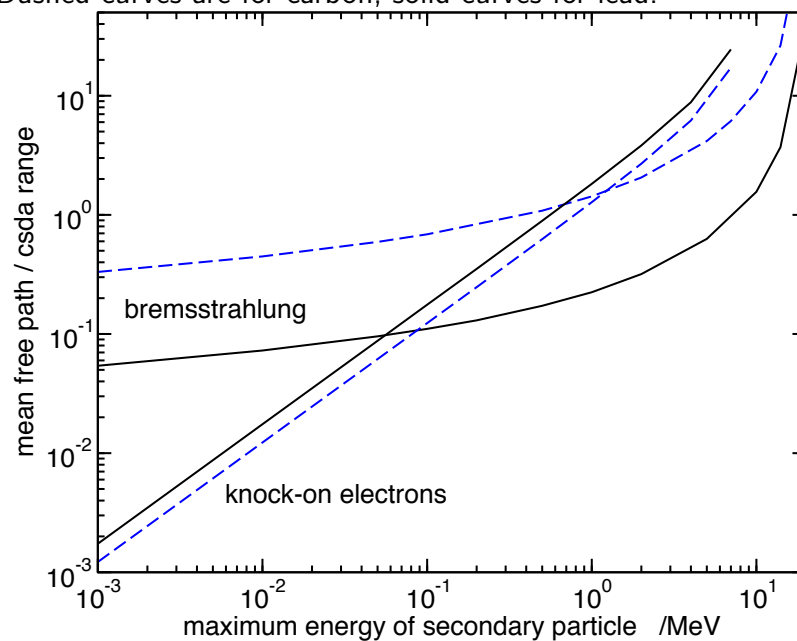


Figure 20: Mean free path to events producing knock-on electrons or bremsstrahlung photons above a minimum energy for 20 MeV electrons in carbon (dashed) and lead (solid). Distances are as a fraction of the CSDA range. Data are from the EGS4 system (Nelson et al, 1985).

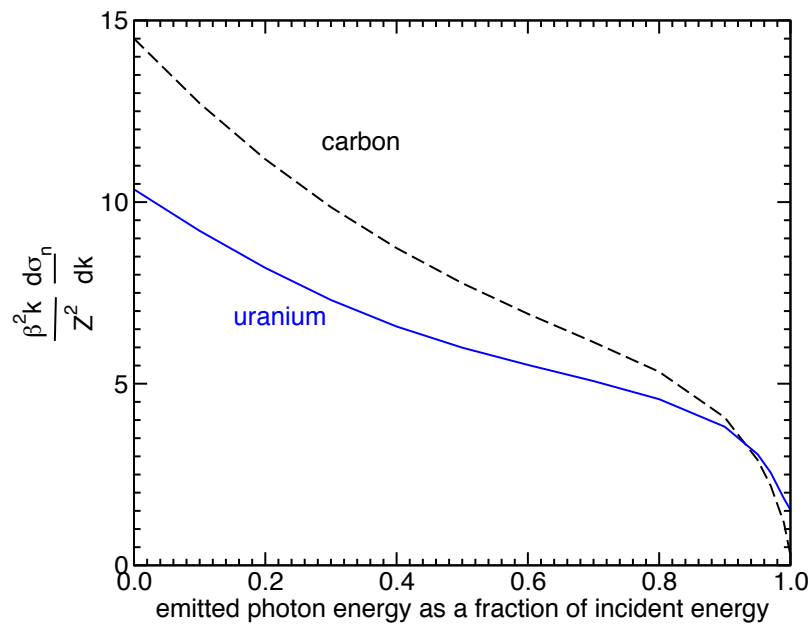


Figure 21: Scaled bremsstrahlung cross section differential in emitted photon energy for 20 MeV electrons interacting with carbon and uranium nuclei. Data are from Seltzer and Berger (1986).

Figure 20 presents data showing the mean free path of 20-MeV electrons in lead or carbon before the creation of a secondary photon or electron above the production threshold. Even for very low thresholds, the electrons produce only a “few” bremsstrahlung photons. From Fig. 19 we know that if we use a threshold of 1 keV for a 20-MeV electron, the discrete events account for more than 99.9% of the radiative energy loss. Figure 20 tells us that for the same threshold, a 20-MeV electron slowing in lead has a mean free path of 0.05 times its CSDA range. Thus it would generate about $1/0.05 = 20$ photons while slowing down if the mean free path between discrete events did not change with energy. The mean free path actually increases as the electron slows down and hence even fewer photons would be created.

Figure 20 also shows why it is impossible to simulate the creation of all secondary electrons. Reducing the threshold energy from 100 to 1 keV requires 100 times as many secondary electrons to be simulated but accounts for only 15% more of the energy loss (Fig. 18).

Figure 21 presents a comparison of the scaled bremsstrahlung cross section differential in emitted photon energy, $\beta^2 Z^{-2} k d\sigma_n/dk$, for 20-MeV

electrons in uranium and carbon. It is interesting to note how similar these two cross sections are even though the corresponding thick-target spectra would be very different due to photon attenuation in the targets. Note also that it is the relative flatness of this shape which, in Fig. 19, leads to the linearity of the curves that are related to the integral of this cross section.

Another aspect of electron transport is the angular deflection of the electrons by multiple elastic scattering from atomic nuclei. There are approaches to the description of this effect, such as the multiple-scattering theories of Goudsmit and Saunderson (1940) or Moliere (1948) and the simpler Gaussian approximation used by, e.g., Nahum (1975). For a detailed review, see Scott (1963). To get a feeling for multiple-scattering effects one can consider the mass scattering power T/ρ which is defined as the increase $d\theta^2$ in the mean square angle of scattering θ^2 per unit mass thickness traversed, ρdl (ICRU, 1984a). Figure 22 presents the mass scattering powers of lead and carbon versus electron energy. Electron multiple scattering is much more important in heavier elements and decreases rapidly as electron energy increases.

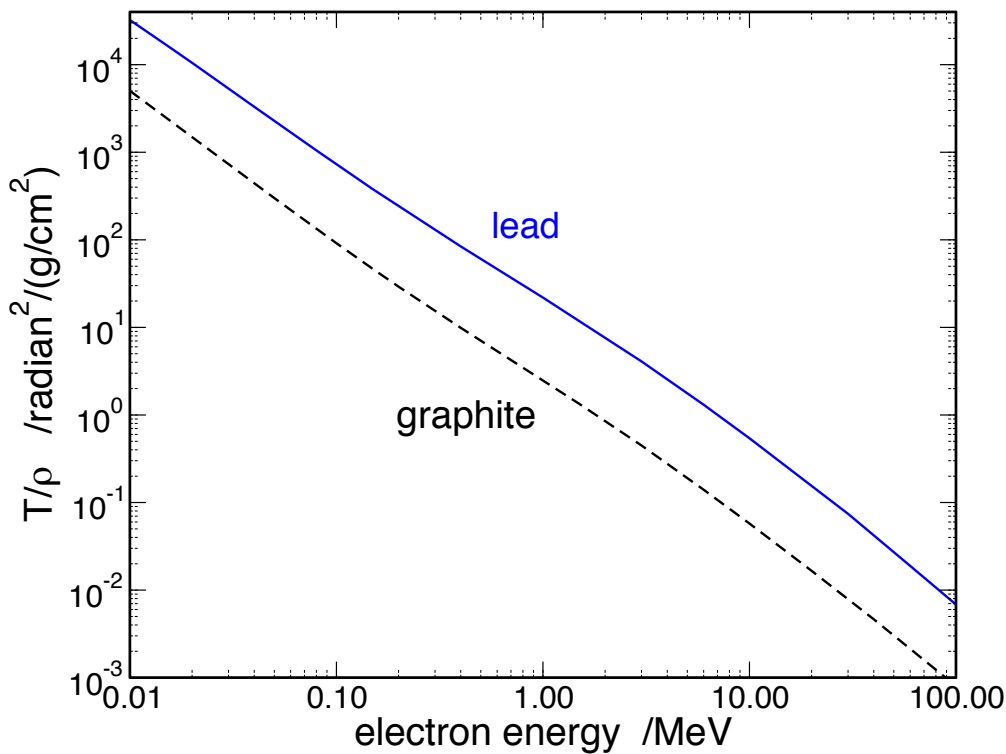


Figure 22: Mass scattering power as a function of electron energy for carbon (dashed) and lead (solid).

This completes the overview of cross-section trends. One caveat should be mentioned, namely that electron cross sections for energies near or below the binding energy of the medium should be regarded skeptically if binding effects have been ignored.

II.C. STEP-SIZE EFFECTS

So far we have paid no attention to how to choose the size of each electron step in a Monte Carlo simulation. Step-size selection can affect dramatically both the accuracy and the computation time.

At the beginning of an electron step, one knows the initial position \mathbf{x}_i and the initial direction \mathbf{u}_i , and one needs to choose the total path length t to the end of the electron step. This total path length is used by the various physical theories to determine (perhaps stochastically) the energy of the electron at the end of the step, the position at the end of the step \mathbf{x}_f , and the new direction at the end point \mathbf{u}_f , as characterized by the multiple scattering angle θ . The equations relating \mathbf{u}_f to \mathbf{u}_i through θ are fully described by Berger (1963).

To compute the position of the end point of the step \mathbf{x}_f , one must calculate s , the component of straight-line transport of the step along the initial direction. The quantities s and t are depicted in Fig. 23 for a typical electron transport step. The quantity s is related to \mathbf{u}_f through the relation

$$\mathbf{s} = (\mathbf{x}_f - \mathbf{x}_i) \cdot \mathbf{u}_i \quad (1)$$

Berger proposed the following relationship between s and t :

$$s = \frac{1}{2}t(1 + \cos \theta(t)) \quad (2)$$

and proved that $\langle s \rangle$, the average value of s , computed from Eq. (2) is valid when θ is small and computed according to the multiple-scattering theory of Goudsmit and Saunderson (1940). Note that s as computed by Eq. (2) is

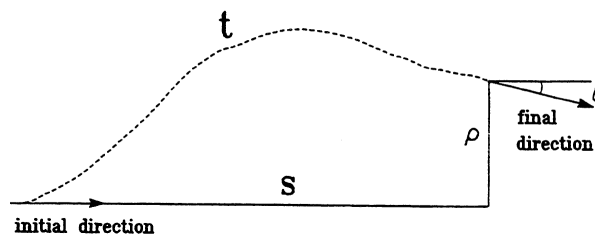


Figure 23: A representative electron step depicting the various geometric components: t , the total (curved) path length of the step; s , the component of transport distance along the initial direction; ρ , the lateral displacement; and θ , the multiple-scattering angle.

correlated with the multiple-scattering angle and hence it exhibits a distribution about its mean value. (It is unknown at this stage whether or not this distribution is accurate.) Lewis (1950) has given the exact expression for $\langle s \rangle$,

$$\langle s \rangle = \int_0^t dt' \langle \cos \theta(t') \rangle \quad (3)$$

The “path length correction” (PLC), defined as $(t - \langle s \rangle) / \langle s \rangle$, is a relatively strong function of t and is a measure of the curvature in the electron step. To illustrate this, Fig. 24 presents the PLC in water versus electron kinetic energy for various electron step sizes, characterized by the fraction of the electron’s kinetic energy lost to all collisional processes. One can conclude from this figure that the PLC is significant except for very high electron energies or very small step sizes. Thus, for accurate transport one should include a correction for path length curvature, unless one is willing to pay the cost of calculating electron histories using exceedingly short steps. Equations (2) and (3), evaluated using the Moliere multiple

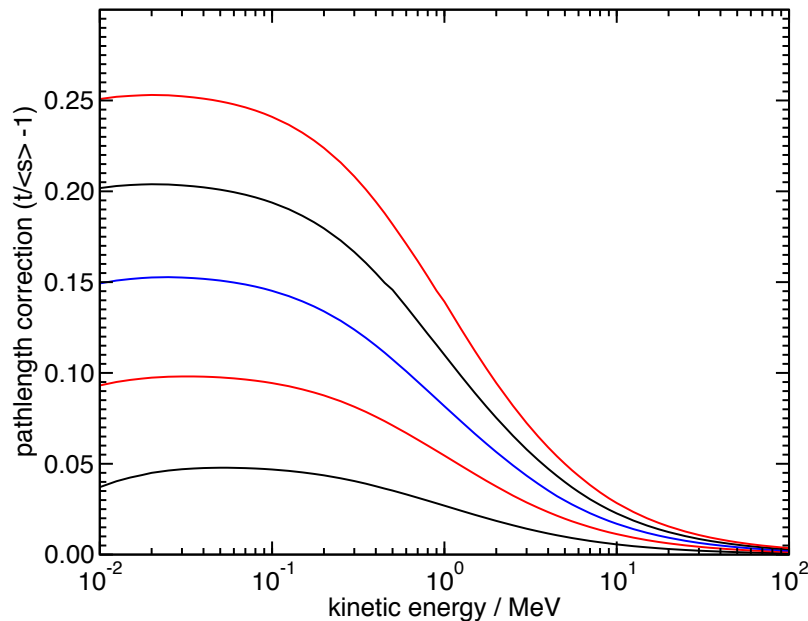


Figure 24: Path length correction $t/\langle s \rangle - 1$ in water versus electron kinetic energy for various step sizes characterized by the percent energy loss due to all collisional processes. Calculated using Eq. (3) and the Moliere multiple-scattering theory. Computational details are given in Bielajew and Rogers (1986a, 1987).

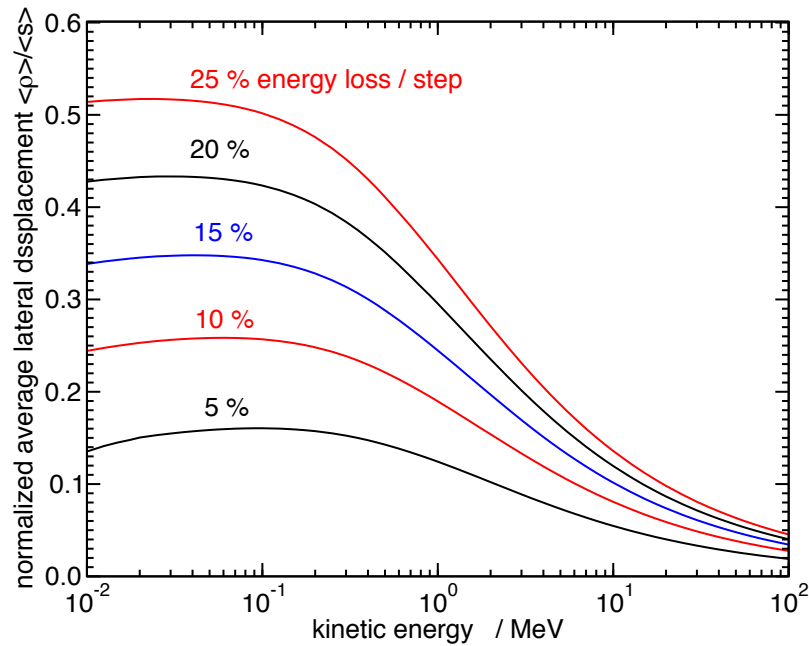


Figure 25: Average lateral displacement $\langle \rho \rangle$ divided by $\langle s \rangle$ versus electron kinetic energy for various step sizes.

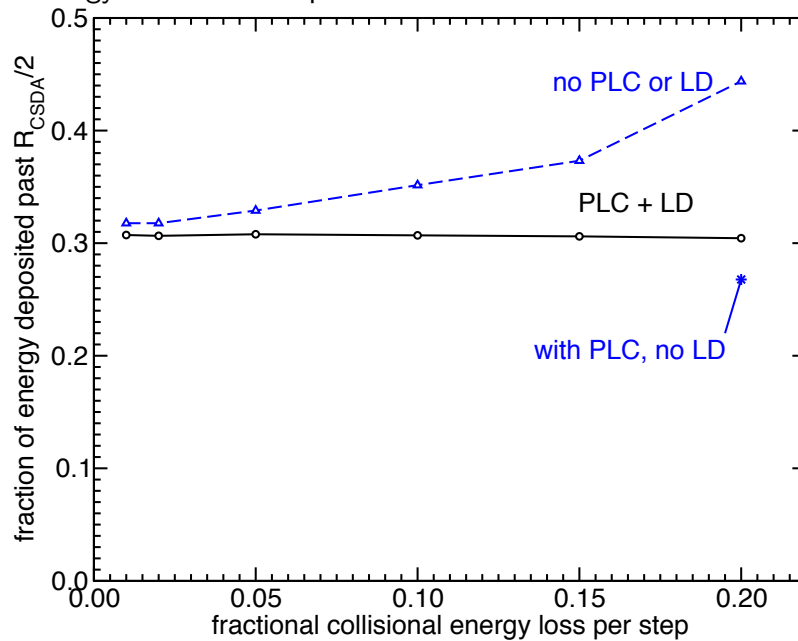


Figure 26: Fraction of energy deposited past one-half the CSDA range for 1.0-MeV electrons incident normally on water, versus step size, as characterized by the fraction of energy lost per step.

-scattering theory, have been shown to produce reliable results for $\langle s \rangle$ even for average angles as large as 1 radian (Bielajew and Rogers, 1986a, 1987). Presumably, this conclusion would also apply to the use of the Goudsmit-Saunderson multiple-scattering theory since both theories lead to similar angular distributions (Bethe, 1953; Berger, 1963). However, the use of the Fermi-Eyges multiple-scattering theory (Eyges, 1948) to calculate the PLC (Messel and Crawford, 1970; Nelson et al., 1985) has been shown to be unsatisfactory for all energies (Bielajew and Rogers, 1986a, 1987).

Figure 24 illustrates some interesting facts about electron transport. As the electron energy increases, the electrons tend to travel in straighter lines, and path curvature due to multiple scattering becomes less important. As one decreases the electron energy, one notices a “leveling off” of the curves with constant energy loss per step. This reflects the fact that, although the electron steps have more curvature at low energy, the collision stopping power is also increasing, reducing the relative size of the step for a given fractional energy loss. A useful rule of thumb (which appears to be merely coincidental) is that, for electrons in water with energies below about 100 keV, the PLC is roughly equal to the fractional energy loss.

One should also consider the lateral displacement ρ of the electron during the course of a step as depicted in Fig. 23. Berger (1963) proposed the expression

$$\rho = 1/2t \sin \theta \quad (4)$$

which expresses the basic correlation of ρ with the multiple-scattering angle θ . We have calculated $\langle \rho \rangle / \langle s \rangle$ from Eq. (4), evaluating $\langle \sin \theta \rangle$ in the small-angle approximation ($\sin \theta \approx \theta$) and using the first (Gaussian) term in the Moliere multiple-scattering theory. Figure 25 shows $\langle \rho \rangle / \langle s \rangle$ in water for various fractional collisional energy losses and indicates that it is necessary to include the lateral displacement for an accurate description of electron transport trajectories, except at high energies or with very short step sizes.

To illustrate step-size dependence when a PLC and lateral displacement (LD) are not included, Fig. 26 shows the calculated fractional energy deposited beyond a boundary at one-half of the CSDA range $r_0/2$ for 1.0-MeV electrons incident normally on water. The “no PLC or LD” case shows a significant overestimate that grows with step size (in this case, the fractional energy loss per step). The results of calculations with PLC and LD do not depend on step size, if the electron transport is being done accurately. The difference between the two calculations arises almost entirely from the omission of the PLC. The effect of lateral displacement

is less significant, as shown by the results for a fractional energy loss of 0.2 which included the PLC but not the lateral displacements. The PLC defined in Eq. (3) was used for this and the next simulation, with the average value of the cosine evaluated using the Moliere multiple-scattering theory (Bielajew and Rogers, 1986a, 1987). Note that at small step sizes the “no PLC or LD” results converge to the “with PLC and LD” results, reflecting the fact that small step sizes provide more accurate electron transport. The lateral displacement can have large effects as well. Figure 27 demonstrates the calculation of dose in a cylindrical air cavity, 2 mm in depth and 1 cm in radius, surrounded by 0.5 g cm^{-2} carbon walls, irradiated by a broad parallel beam of 1.25-MeV photons. The dose to the air cavity is known by ionization cavity theory (Spencer and Attix, 1955; Bielajew, 1986a). The results of the calculations that include the PLC and lateral displacements are independent of step size, while a similar calculation

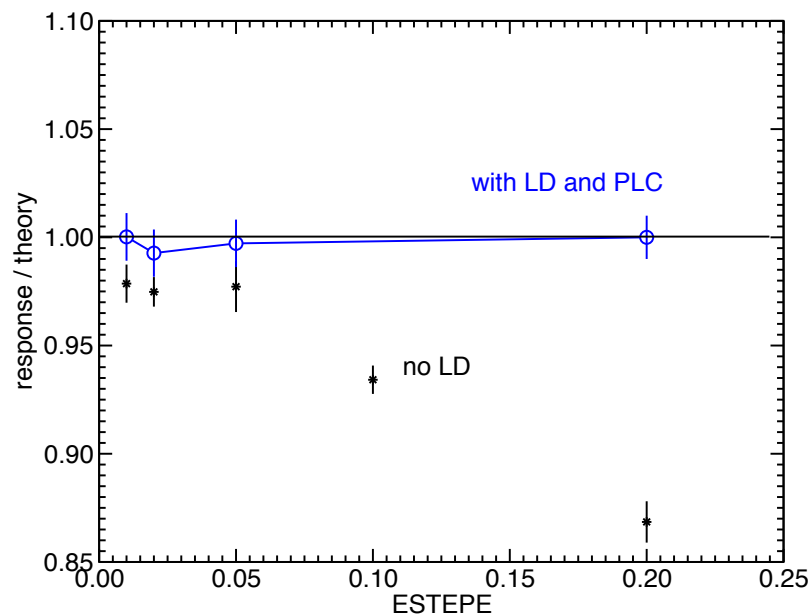


Figure 27: Ion chamber response to ^{60}Co γ rays as a function of the electron step size, characterized by the fractional energy loss to low-energy processes below a 100 keV threshold. The calculation with path length correction, PLC, and LD, shows no step-size dependence, whereas the calculation without LD shows a marked dependence.

that neglects lateral displacements shows a marked dependence on step size.

Step-size dependences of this kind are typical in electron transport calculations (Seltzer and Berger, 1974; Rogers, 1984a). If one does not properly account for path length correction and lateral transport, one may still obtain accurate results by reducing the electron step size. One should take care, however, not to reduce the electron step size so much as to violate fundamental constraints of multiple-scattering theory; otherwise, spectacular calculational artifacts can occur (Rogers, 1984a). It is preferable to include PLC and lateral displacement, thereby greatly reducing step-size dependence. This permits larger electron step sizes and, potentially, faster execution times (Bielajew and Rogers, 1986a, 1987). However, these new methods have not been as extensively validated against experimental data as have traditional methods (Berger and Seltzer, 1973; Nelson et al., 1985).

For the previous two examples, Figs. 26 and 27, electron transport was simulated in the vicinity of “interfaces.” Interfaces are surfaces that delineate different scoring regions (e.g., in Fig. 26, the region beyond $r_o/2$) or different material regions (e.g., in Fig. 27, the air cavity of the ion chamber). Careful electron transport simulation is required in the vicinity of such interfaces. The underlying reason for this is the fact that the multiple-scattering theories used by condensed-history Monte Carlo simulations are valid only in infinite or semi-infinite media. The introduction of interfaces violates the fundamental constraints of the underlying theories.

To avoid calculational artifacts one must, at least in the vicinity of an interface, shorten the electron steps so that for a majority of them the transport takes place as if in an infinite medium. EGS4 does this by allowing the user to control the geometric step length or the fractional energy lost to “continuous” energy loss processes per electron step. These constraints are chosen with regard to the geometry in which the simulation takes place and apply everywhere, not only in the vicinity of interfaces. The ETRAN-based codes also control the amount of energy lost “continuously” per step.

PRESTA (Bielajew and Rogers, 1986a, 1987), an electron transport option available with the EGS system, employs yet another strategy. In the vicinity of an interface, electron steps are shortened so that for the majority of them no part of the actual curved path, or lateral displacement, can straddle the interface, whether or not the media on either side of the interface are different. As an electron approaches the interface the steps are reduced until they are so short that there is almost no path length

correction associated with the step. At this point lateral displacements are turned off so that boundary crossing, if it is to occur, can take place without ambiguity. The reverse holds true as well. As an electron moves away from an interface its steps are progressively lengthened, but only enough to make it seem that the transport takes place in an infinite medium.

Whatever the strategy employed, the underlying reason is the same: the majority of electron paths must take place as in an infinite medium. This is accomplished by shortening the electron steps, if only in the vicinity of interfaces. Some violation of the underlying multiple-scattering theories must occur as an electron crosses a surface, but if this is allowed to affect only a small fraction of the total electron path, the quality of the calculated results should not be unduly compromised.

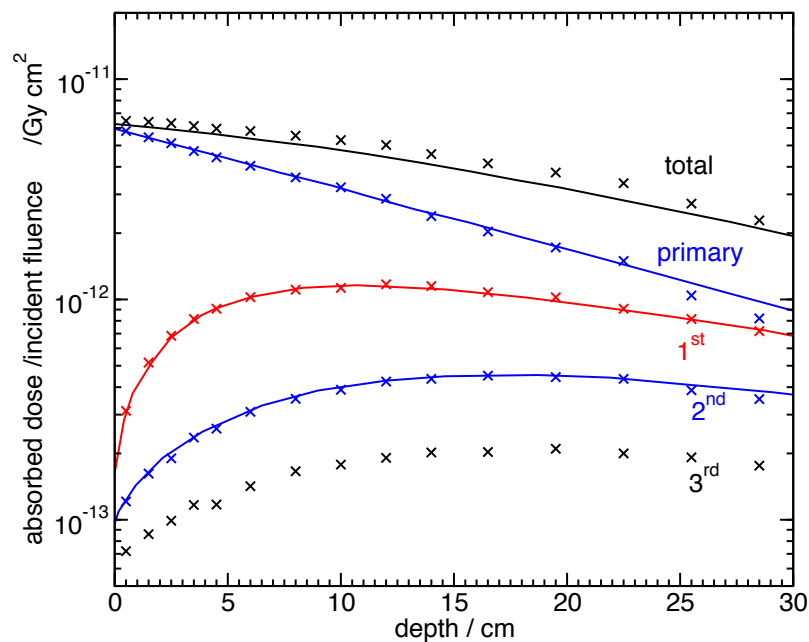


Figure 28: Monte Carlo and analytic calculations of the dose components versus depth for a broad beam of ^{60}Co γ photons on water. Components arising from the primary, first, second, and third Compton interactions as well as the total dose are shown. Analytic calculations are shown as solid lines (Wong et al., 1981) and the Monte Carlo results (Rogers and Bielajew, 1985) as x's. The analytic "total" calculation sums the primary, first, and second scatter contributions while the Monte Carlo calculation sums all scattering orders.

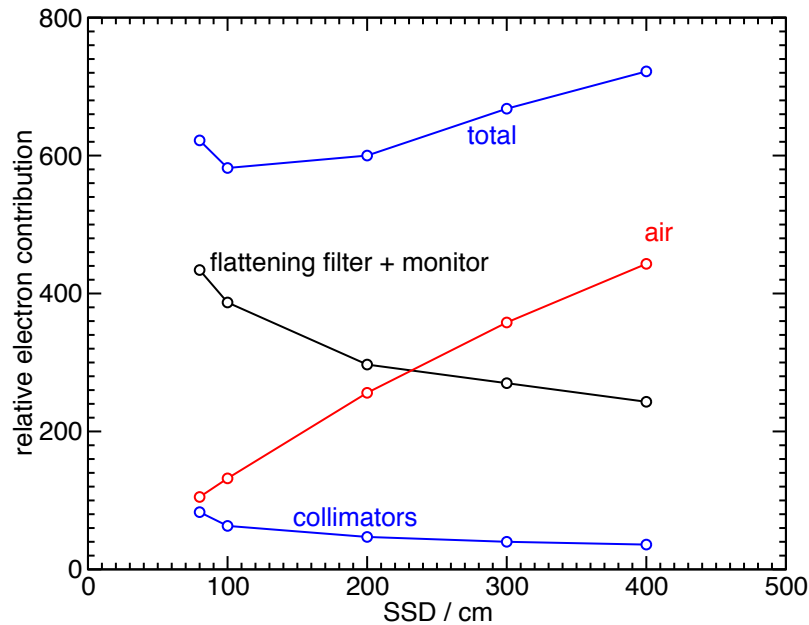


Figure 29: Sources of electron contamination versus source-to-surface distance (SSD) in the 25-MV photon beam of a Clinac-35 accelerator as calculated by Petti et al. (1983) using EGS. The electron contamination from the flattening filter and monitor chamber and from the fixed and movable collimators decreases with distance, while the air-generated electrons increase with distance.

II.D. SCORING QUANTITIES OF INTEREST

II.D.1. Introduction

Up to this point we have discussed the simulation of electron and photon transport. In this section we discuss scoring or extracting from the simulations the quantities of interest. One of the major advantages of Monte Carlo techniques is that we can score many more quantities than are physically measurable except under unusual circumstances. For example, we can not only score the energy deposited in a water tank but also keep track of the origin of the electron or photon depositing the energy and how often it or one of its ancestors were involved in a Compton scattering event. Figures 28 and 29 show examples of two calculations in which such scoring techniques have been applied to separate different scattering components of the dose in a phantom irradiated by ^{60}Co

photons and to identify the origins of the electron contamination in a 25 MV photon beam.

II.D.2. Scoring Techniques

In many situations one is interested in scoring a quantity, such as absorbed dose, averaged over some physical region. These scoring regions may or may not coincide with the regions that define the geometry through which the particles are transported. For example, if one were calculating a depth-dose curve in a homogeneous medium one could, for transport purposes, consider the entire slab as one region with no internal boundaries and allocate the energy deposition into various depth bins. This technique makes the transport simulation as fast as possible since there are no internal boundaries to cross and boundary crossing, or at least checking for it, can take a lot of time. On the other hand, the allocation of deposited energy can be complicated and necessitate some approximations, especially if the average electron step size is large compared to the dimensions of the scoring regions. The other approach is to define the scoring and geometric regions to be the same. Most Monte Carlo codes terminate particle steps at geometric boundaries (as EGS does) or at least arrange to take very small steps near the boundaries. In either case, scoring energy deposition becomes simple and more exact because steps are generally all in one region. However, the transport can be slowed considerably.

In general, to ensure accuracy we use the second procedure, in which the scoring and geometric regions are the same. However, we have also found that using scoring regions different from the geometric regions becomes essential in certain complex geometries. In these cases, short electron steps must be used in order to minimize errors.

a. Energy and Charge Deposition. Energy and charge deposition are the most straightforward quantities to score. They must be scored in regions of finite dimensions and this can lead to binning artifacts. For example, compare the “no-multiple-scatter, no-straggle” case with different bin widths as shown in Figs. 30 and 31.

b. Particle Fluence. Particle fluence (or simply “fluence”) is a point function which is formally defined as the number of particles entering a sphere per unit cross-sectional area (strictly speaking, in the limit of an

infinitesimal sphere). Starting from this definition, it can be shown that the average fluence in a given region is the sum of the particle track lengths in that region divided by its volume (see Chilton, 1978, 1979). This relationship between track length in a volume and average fluence is the basis for scoring fluence in many Monte Carlo codes. The only drawback is that by nature it computes the average fluence in a region. In a slab geometry, this restriction can be overcome by letting the volume of interest shrink to zero thickness, in which case the track length per unit volume is equivalent to the sum, over the particles crossing the plane, of $(1 + PLC)/|\cos\theta|$ divided by the area of the plane, where θ is the angle the particle makes with respect to the normal to the plane (i.e., $\theta = 0^\circ$ for normal incidence), and the path length correction is defined in Section II,C. This quantity gives the fluence at the plane and follows from the previous formulation because the path length for each particle in an infinitesimal slab volume of thickness dl is given by $(1 + PLC)dl/|\cos\theta|$. When using this approach one must set some maximum on θ since for θ near 90° , $1/|\cos\theta| \rightarrow \infty$ and this will distort the fluence calculation. One must then investigate the sensitivity of the calculated fluence to the choice of cutoff angle (we find that 5° is often acceptable). For photons, $1 + PLC$ is unity, but as discussed in Section II,C it can be significantly different from unity for large electron step sizes.

Two comments are in order. The technique of scoring particles crossing a plane is attractive because it calculates the fluence at a specific depth for slab geometries. For photon or neutron calculations this can be efficient, but for electron transport simulations, the total path length of low energy electrons is so short that only a very small fraction of them ever cross a particular plane. It is virtually essential to use path length per unit volume when scoring electron fluence spectra for low energies. In this case, a large number of short paths contribute to the fluence estimate.

The second comment is to emphasize that experiments often measure the planar fluence (the number of particles crossing a plane per unit area of the plane) and this is not the same as the fluence (e.g., see Attix, 1986).

c. Statistical Estimation. In most electron transport simulations only the current parameters of the particles are used in scoring. However, for photon (and neutron) transport there are various statistical estimation techniques for scoring various quantities. These techniques for scoring can greatly enhance the efficiency of certain calculations (for example, the probability of getting through a shielding wall). These techniques are summarized by McGrath and Irving (1975), Stevens (1980), and Alm

Carlsson (1981). Examples from medical physics are given by Persliden and Aim Carlsson (1986) and Williamson (1987).

d. Tagging a History. One of the advantages of the Monte Carlo technique is the ability to ask questions about any aspect of the history of a particle. In the EGS system each particle has a tag associated with it and the value of this tag, which can be set by the user, is passed to all the descendants of the particle. The user can interrogate or change this tag under a wide variety of circumstances (e.g., before or after any particular class of interaction has occurred, energy has been deposited, or a boundary has been crossed). This flexible interface to the transport simulation makes it possible to score a broad range of quantities with ease.

e. Retrospective Versus “On-the-Fly” Scoring. The extreme of retrospective scoring is to run a simulation, store the parameters of each particle at the end of each step, and then score or analyze the data using a second program. While this was a reasonable approach for certain neutron transport calculations, it is not useful for electron calculations because of the huge quantities of data that would have to be stored for each of the multiple-scattering steps. It is cheaper to recalculate.

A more practical form of retrospective analysis is to “bin” certain results (e.g., fluence spectra) and use these after the simulation to calculate spectrum-averaged quantities of interest. As long as the quantities of interest or the fluence spectra do not vary rapidly over any single bin, this procedure is accurate [as was the case, e.g., in the work on $(\bar{\mu}/\rho)$ by Cunningham et al., 1986]. However, one can lose considerable accuracy with this technique when fluence spectra are sharply peaked. For example, when calculating the average energy lost by a particle passing through a thin plate (e.g., Fig. 4, where bins as narrow as 50 keV were needed), one would lose considerable accuracy by using wide bins (say 500 keV or greater). In general, the accuracy is no better than the bin width. For this reason it is often advisable to score parameters directly, e.g., score the average energy as

$$\bar{E} = \frac{1}{N} \sum_{i=1}^N E_i$$

where E_i is the energy of each particle and N is the total number of events, rather than binning the results into M bins and calculating

$$\bar{E} = \frac{1}{M} \sum_{j=1}^M \bar{E}_j N_j$$

where E_j is the “energy” of bin j and N_j is the number of particles in that bin.

There are also classes of problems which require that scoring be done “on-the-fly.” An example is the calculation of the correction factor A_{wall} for ionization chambers (Nath and Schulz, 1981; Rogers et al., 1985a). In this case one must weight the energy deposited in the gas cavity by a factor which depends on the location of the initial photon interaction giving rise to the electron which deposits the energy.

II.D.3. Use of Symmetries

Use of symmetries in a problem can greatly improve the efficiency of a Monte Carlo calculation. In particular, one should strive to reduce the number of dimensions in a problem whenever possible. For example, in many cases the distinction between a circular or a square beam is unimportant. If so, simulating the circular-beam case is much preferred because quantities of interest can be scored in two dimensions rather than three. If a rectangular beam is critical but the phantom is a two-dimensional slab geometry (i.e., the composition varies only with depth), many symmetries can be exploited. For instance, there are symmetries about both midlines of the rectangle. In scoring fluence or dose, one can make use of this by adding the data from all four quadrants at the end of the simulation but before analyzing the results. Another, somewhat more complex, solution is to treat the symmetry planes as “mirrors” and do the entire simulation in only one quadrant, letting particles “reflect” from each symmetry plane. Careful electron transport must be done near these reflecting planes, but the technique can be very effective.

Another useful application of symmetry, called the reciprocity theorem in ICRU Report No. 35 (1984a), was pointed out for medical physics applications by Bruce and Johns (1960). If one tries to calculate the depth-dose curve in a small region around the central axis for a circular beam of larger radius, a great deal of time is wasted by simulating all the particles which never enter the small region near the central axis. For the case of uniform parallel beams incident normally on slab phantoms, a great deal of computing time can be saved by applying this reciprocity theorem to make use of most particle histories. This theorem states that the energy deposited in a cylindrical detector region of radius r_d per unit incident fluence in a beam of radius r_b is the same as the energy deposited in a scoring region of radius r_b due to the same incident fluence of particles in a beam of radius r_d . Since the number of histories is proportional to the incident fluence times the beam area, and since the statistical uncertainty

is roughly the same when the calculated energy deposition is the same, it is clearly more efficient to do the calculation with a small beam area and large detector. For beams and detectors of finite dimensions, the theorem gives

$$D(r_b, r_d) = D(r_d, r_b)r_b^2/r_d^2 \quad (5)$$

where $D(r_1, r_2)$ is the average dose in a region of radius r_2 per unit incident fluence in a beam of radius r_1 . In the extreme case, one uses a pencil beam and large scoring region to determine the central-axis dose in a broad or even infinite beam [i.e., $r_d = 0$ and $r_b \rightarrow \infty$ in the terminology of Eq (5)]. It can be shown that in this case

$$D(r_b, 0) = E(0, r_b)/Nt \quad (6)$$

where $E(O, r_b)$ is the energy deposited in a cylinder of radius r_b and thickness t (in kg m^{-2}) by a pencil beam of N particles and $D(r_b, 0)$ is the central-axis dose per unit incident fluence from a beam radius r_b where r_b can be infinite. Using this equation the central-axis depth-dose curves for beams of various radii can be scored simultaneously by using an incident pencil beam and scoring the energy deposited in regions corresponding to the radii of the beams of interest. The results of this powerful theorem also apply for other quantities of interest such as the particle fluence and particle fluence spectra.

II.E. THE SELECTION OF RANDOM NUMBERS

Monte Carlo calculations attempt to simulate the stochastic nature of particle-particle interactions by sampling in a random fashion from known particle interaction cross sections. This requires a random number generator (RNG) capable of producing a sequence of truly independent random numbers. The only way to guarantee such a sequence is to utilize some naturally occurring random phenomenon, such as electrical noise or the decay of radioactive nuclides. However, it is often impractical to couple such a device to computers.

Digital computers cannot provide a truly random sequence of numbers but can calculate pseudorandom sequences that are acceptable for most Monte Carlo applications. These pseudorandom number generators have limitations which should be understood before one attempts a Monte Carlo calculation.

The RNG most commonly used in Monte Carlo calculations is of the form

$$I_{n+1} = (aI_n + c) \text{ modulus } 2^k \quad (7)$$

where I_n is the n th random integer in the sequence, a is the "multiplier," c is the "increment," and k is the number of bits in the integers of the computer. This RNG with the modulus related to the machine word size is an important subset of linear congruently random number generators (LCRNGs) since it can produce the number very quickly. An important further subset of LCRNGs is obtained by setting $c = 0$ in Eq. (7). This defines the multiplicative congruently random number generator (MCRNG). LCRNGs and MCRNGs are the methods of choice for many Monte Carlo codes (Berger, 1963; Nahum, 1975; Andreo, 1980; Nelson et al., 1985) and can produce long sequences of random numbers with little cost in computing time.

However, LCRNGs and MCRNGs suffer from two major shortcomings. The first is that they have a finite sequence length, ultimately repeating themselves. Knuth (1981) gives general guidelines for choosing a and c . For appropriate choices the sequence lengths of LCRNG and MCRNG have maximum values of 2^k and 2^{k-2} (4×10^9 and 1×10^9 , respectively, for 32-bit machines).

In some cases, even this maximum sequence length is inadequate. The Monte Carlo simulation of a single particle history may consume hundreds or even thousands of random numbers and an accurate simulation may require in excess of a million particle histories. To be sure of not cycling a simulation, it is advisable not to exhaust an RNG or even approach its sequence length. However, even if the RNG does repeat its sequence, the particle histories will often still be different because the random numbers must also become synchronized before causing duplicate histories; i.e., it is only when the initial random number of a history repeats that the simulation begins to repeat itself. The problem is that it is virtually impossible to tell when this has occurred. To guarantee the independence of Monte Carlo histories, it is possible to use alternative forms of RNGs with longer sequence lengths (Knuth, 1981). However, these RNGs have been subjected to less theoretical study than LCRNGs. Alternatively, it is possible to perform 64-bit integer arithmetic on 32-bit computers with random sequences that are long enough (5×10^{18}) for any practical calculation (Biela-jew, 1986b). The factor of 7 increase in time to calculate the random numbers causes an increase of 15-20% in typical problems.

The second significant shortcoming of LCRNGs is the fact that n -tuple sets of random numbers can be highly correlated; i.e., they align themselves along $(n-1)$ -dimensional hyperplanes in n -dimensional space. For example, if one selects triplet sets of random numbers to define points in a cube, these points lie on a finite set of planes within the cube. This effect was first discussed in a paper by Marsaglia (1968). RNGs which distribute the points over many planes are said to have good “spectral” qualities. For most practical problems, the fine granularity from many planes will not bias the final result, but even some of the RNGs distributed by major manufacturers have had bad spectral qualities and these can have disastrous consequences.

At present no theoretical method exists for predicting the optimum LCRNG parameters a and c . Rather, a and c must be determined experimentally. Examples of good parameters have been published (Knuth, 1981; Ehrman, 1981). Unless one is prepared to undertake extensive testing of new LCRNG parameters, it is safest to use those already evaluated. The EGS4 system, implemented on a 32-bit machine, uses an MCRNG with $a = 663608941$, $c = 0$, $k = 32$. Ehrman (1981) showed that this is one of the fastest RNGs available, has over 1100 planes in a unit cube, and has a cycle length of $\sim 10^9$.

The amount of computer code required for an LCRNG is quite small. To maximize the speed of random number selection, the RNG should be coded “in-line” whenever it is needed rather than calling a RNG subroutine. Typically, the time required for executing a subroutine call is equivalent to the time required to perform several floating-point operations. Therefore, in-line RNG coding can save significant computing time. For example, when we changed the call to the VAX random number generator used by the ITS code CYLTRAN (Halbleib and Melhorn, 1984) to the inline random number generator used by EGS4, we found the entire CYLTRAN code ran about 15% faster.

II.F. AN EXAMPLE: 20-MEV ELECTRONS ON A SLAB OF WATER

The case of 20-MeV electrons incident on a flat slab of water has been discussed often (Seltzer et al., 1978; Nahum, 1975; Andreo and Brahme, 1984; Berger and Seltzer, 1982b) because it is representative of an important class of problems in radiotherapy and radiation dosimetry and it also demonstrates a variety of important concepts.

II.F.1. Depth-Dose Curves

We will first consider a series of EGS4 depth-dose calculations in which various physical effects are turned on and off. Recall that Figs. 3 and 4 show the effects of various processes as a 20-MeV beam passes through a thin slab of water.

First consider a CSDA calculation in which there is no multiple scattering and no energy straggling. The electrons travel in straight lines and go the same depth into the phantom, where they deposit their residual cutoff energy. This would lead to an effectively infinite value of the dose unless the residual cutoff energy was deposited in a finite-sized depth bin (Fig. 30). If we now include multiple scattering, there is a large effect as the electrons spread out laterally. This shortens their depth of penetration and causes a broad peak in the depth-dose curve because the fluence (which is most usefully thought of as the total path length per unit volume) has increased due to the scattering. Note that the multiple scattering has introduced a distribution of depths of penetration, although the actual

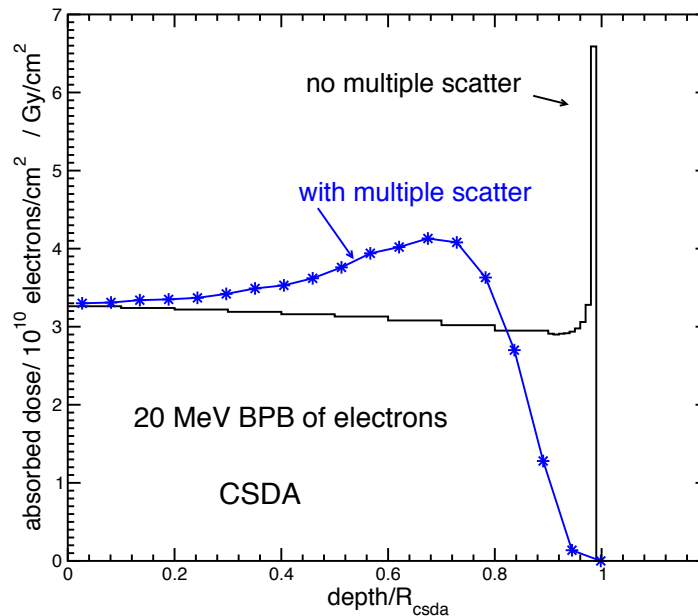


Figure 30: Depth-dose curves calculated for a broad parallel beam (BPB) of 20-MeV electrons incident normally on a thick slab of water. The histogram is a CSDA calculation with multiple scattering turned off. Note here and elsewhere where multiple scattering is turned off that the value of the dose at the end of the range is very much an artifact depending on the width and location of this bin (see the next figure). The stars show a CSDA calculation with multiple scattering included but with no energy-loss straggling. In all these calculations, electron histories are terminated at $ECUT = 700$ keV.

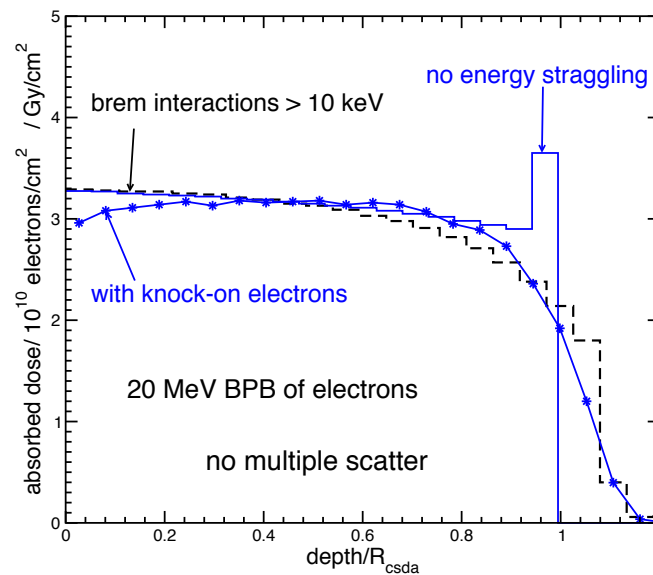


Figure 31: Same situation as Fig. 30 but with no multiple scattering (i.e., all electron paths are straight lines) and with energy-loss straggling included by considering different discrete energy-loss mechanisms. Stars represent calculations including only the creation of secondary electrons above 100keV kinetic energy; the short-dash histogram only the creation of bremsstrahlung photons above 10 keV; the solid histogram no energy-loss straggling.

distance traveled by each electron is still its CSDA range r_0 (less the residual range at the cutoff energy).

Now consider Fig. 31, in which there is no multiple scattering (i.e., all the electrons move in straight lines). The creation of knock-on electrons leads to the curve, shown by the stars, that is lower at the surface because some of the energy transferred to knock-on electrons is transported into the phantom. There is a buildup region until a quasi-equilibrium of knock-on electrons is achieved. At the same time the dose peak at the end of the range has been eliminated because of the range straggling. Each time a knock-on electron is created, the path length of the primary electron is reduced. However, if an electron does not create a knock-on electron, it penetrates farther than in the true CSDA calculation because the continuous portion of the stopping power (which is now given by a restricted stopping power) is smaller. That so little energy is deposited at the end of this range reflects the fact that most electrons create one or more knock-on electrons. Thus, energy straggling leads to range straggling even without multiple scattering. On the other hand, multiple scattering leads to a different sort of range (really depth) straggling.

For an electron beam with no scattering and no knock-on electron production, including the creation of bremsstrahlung photons (dashed histogram in Fig. 31) produces more range straggling than does including

knock-on electron production while ignoring bremsstrahlung and, in particular, has more effect on the slope in the dose falloff region. This may seem surprising since the probability of creating a photon is much lower than that of creating a knock-on electron (see Fig. 20), but the average energy loss per bremsstrahlung photon is much higher than that per knock-on electron.

In Fig. 32 the multiple scattering has been turned on again and we present a comparison of a true CSDA calculation with three calculations that include different energy straggling. It is again clear that the energy straggling induced by bremsstrahlung production has a stronger effect on the dose falloff portion of curves than that from knock-on electron production.

II.F.2. Fluence Versus Depth

It is also instructive to consider the electron and photon fluences (defined in Section II,D,2) as functions of depth in water irradiated by a 20

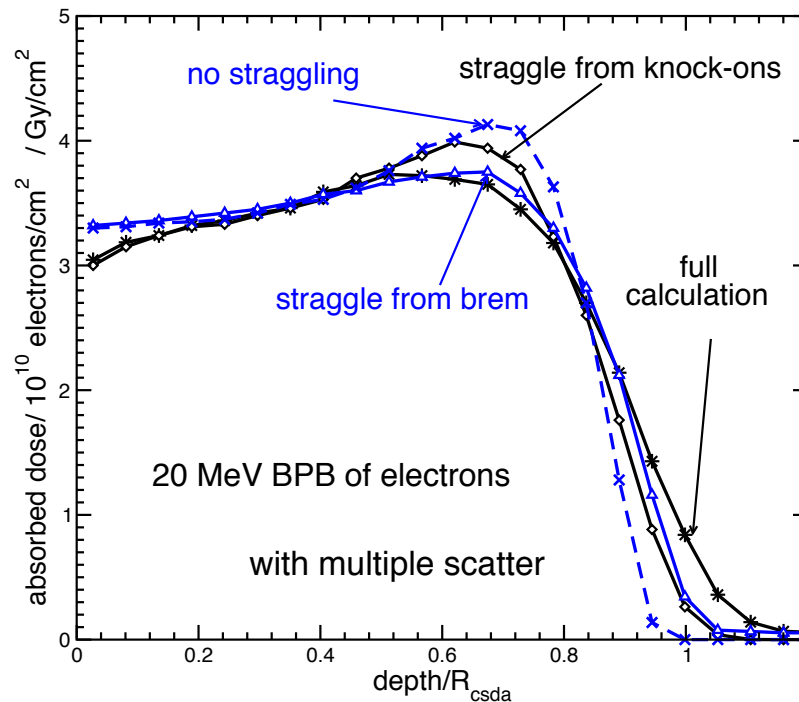


Figure 32: Same situation as Figs. 30 and 31 but with multiple scattering included along with various energy-loss straggling mechanisms. The full calculation with all secondaries created is shown by stars and the CSDA calculation with no straggle by x's. Note that the straggling induced by creation of bremsstrahlung photons with energy greater than 10 keV (triangles) has more effect than the straggle from knock-on electrons (diamonds).

MeV electron beam. The histograms in Fig. 33 show that the total fluence of primary electrons per unit incident fluence is very close to unity near the surface and grows by roughly a fifth due to multiple scattering. Only beyond the fluence maximum does the fluence of primaries exhibit a slight dependence on the cutoff energy, as the fluence of primary electrons between the various cutoffs (10-500 keV) becomes significant. Figure 33 also presents the total fluence per unit incident fluence of electrons with energies above the cutoffs of 10-500 keV. As expected, the total fluence is a strong function of the cutoff energy chosen.

The photon fluence is seen to build up steadily as long as there are high-energy electrons in the beam to create the bremsstrahlung. Past the electron range, the photon fluence decreases due to attenuation. Note that the photon fluence reaches a peak roughly 2.5 times as great as the electron

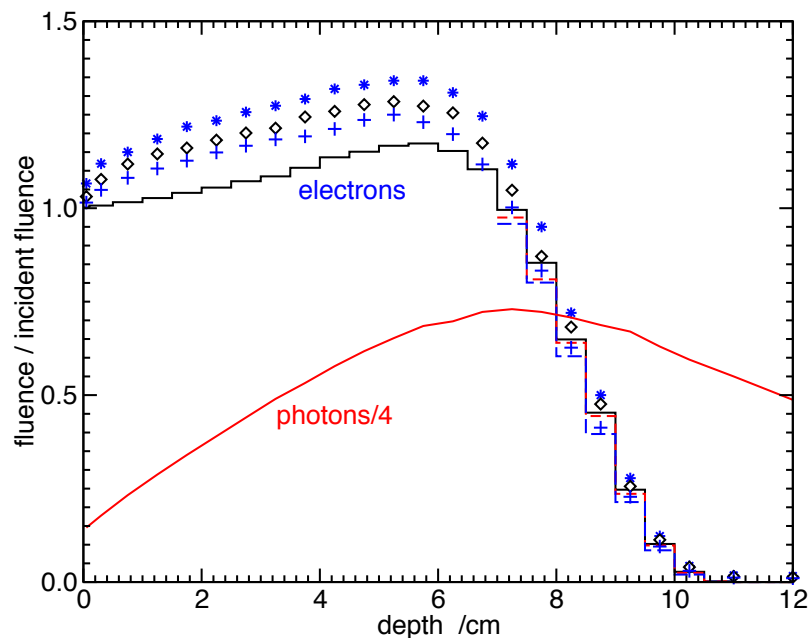


Figure 33: Fluence, per unit incident fluence, as a function of depth for a broad parallel beam of 20-MeV electrons incident on water. The histograms show the fluence of primaries for energy cutoffs $ECUT = 10, 200,$ and 500 keV. The only significant differences are at depths greater than 6 cm, where the larger cutoff causes the fluence to decrease. The symbols show the total fluence for various ECUT values (cross, 500 keV; diamond, 200 keV; star, 10 keV). The smooth curve shows the photon fluence divided by 4. All calculations were done with $AE = AP = 10$ keV.

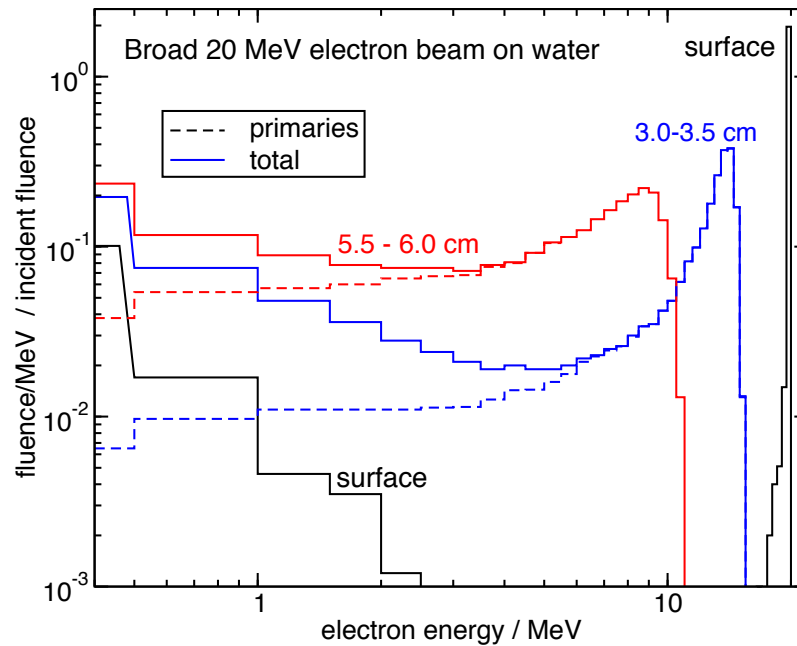


Figure 34: Fluence spectra, differential in energy, in three depth bins for the same calculation as in Fig. 33. Primaries (dashed); total (solid).

fluence although it makes only a small contribution to the energy deposition. Figure 34 presents electron fluence spectra differential in energy at three depths in water irradiated by 20-MeV electrons. The shape of the primary electron fluence spectrum shows the familiar energy-loss straggling distribution discussed earlier. The low-energy knock-on electrons are a significant part of the total spectrum.

II.F.3. Energy Versus Depth

Figure 34 also illustrates the difference between the mean and most probable electron energies at a given depth. At 5.5-6.0-cm depth, the most probable energy is 8.8 MeV, whereas the mean electron energies are 6.45 and 5.74 MeV for primaries and all electrons, respectively. The differential electron fluence at the mean energy of 5.7 MeV is only 50% of the peak value at 8.8 MeV.

Figure 35 shows how different energy parameters vary as functions of depth in water. The major point is that one must carefully specify which

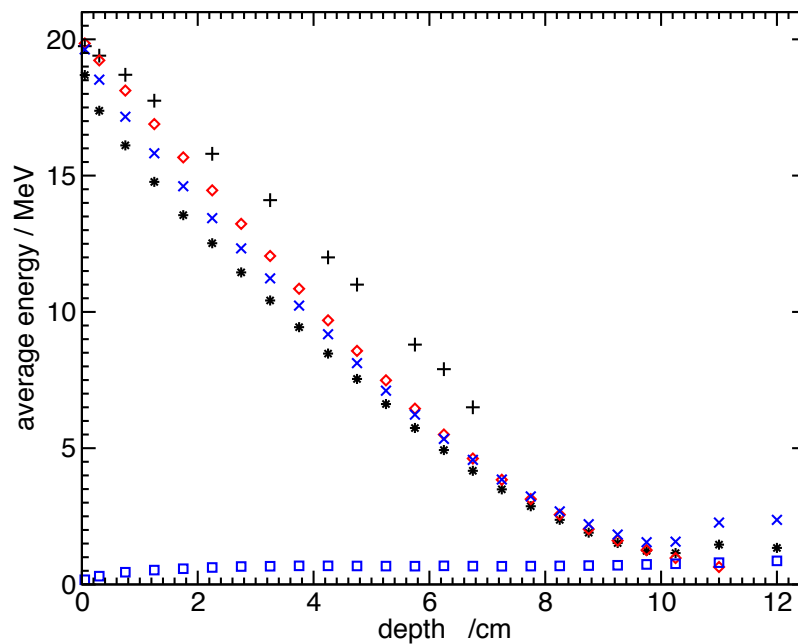


Figure 35: Various energies as a function of depth for the same calculations as in figures 33 and 34 (20 MeV BPB on water). The plus symbols represent the most probable energies in the spectrum. The stars and x's represent the mean energy for the total fluence spectrum for electron energy cutoffs of 10 and 500 keV, respectively. The diamonds show the mean energy of only the primary electrons for a cutoff of 10 keV. Finally the squares represent the mean energy of the bremsstrahlung photons generated within the phantom.

energy is meant. The most probable energy of primaries is distinctly higher than the mean energy. The mean energies of the primaries is the next highest and is reasonably independent of the energy cutoff value used until a depth of ~ 7 cm is reached, where a higher cutoff causes the mean energy to increase slightly. The mean energy of the total spectrum is sensitive to the choice of cutoff since low-energy electrons play a significant role in the spectrum, even near the surface. Andreo and Brahme (1981) have compared mean-energy calculations from a variety of Monte Carlo codes.

The average photon energy shown in Fig. 35 increases for the first few centimeters until an equilibrium seems to be established. Past the depth at which electrons are creating bremsstrahlung, the mean photon energy increases because the water attenuates the low-energy photons more strongly.

II.F.4. Beam Radius Effects

So far, we have discussed only broad beams of 20-MeV electrons, but the behavior of beams of smaller diameter is also of interest. Figure 36 shows the central-axis depth-dose curves for circular parallel beams of area 0.01-200 cm². These curves are calculated from a single simulation using a pencil beam (see Section II,D,3). The dose in the narrow beams falls off more quickly, not because the electrons fail to go as deep but because they scatter away from the axis without being replaced by other electrons scattered onto the axis. In fact, these curves can be used to deduce the spread of a pencil beam by considering the relative values of the dose at one depth. For example, at 5-cm depth a pencil beam deposits 97% of its dose within a circle of area 50 cm², 79% within 10 cm², 55% within 4 cm², 35% within 2 cm², 21% within 1 cm², 11% within 0.5 cm², and 3% within 0.1 cm².

II.G. A COMPARISON OF ETRAN AND EGS

Any general-purpose Monte Carlo code contains a large number of compromises between accuracy and time, both CPU time and programmer's

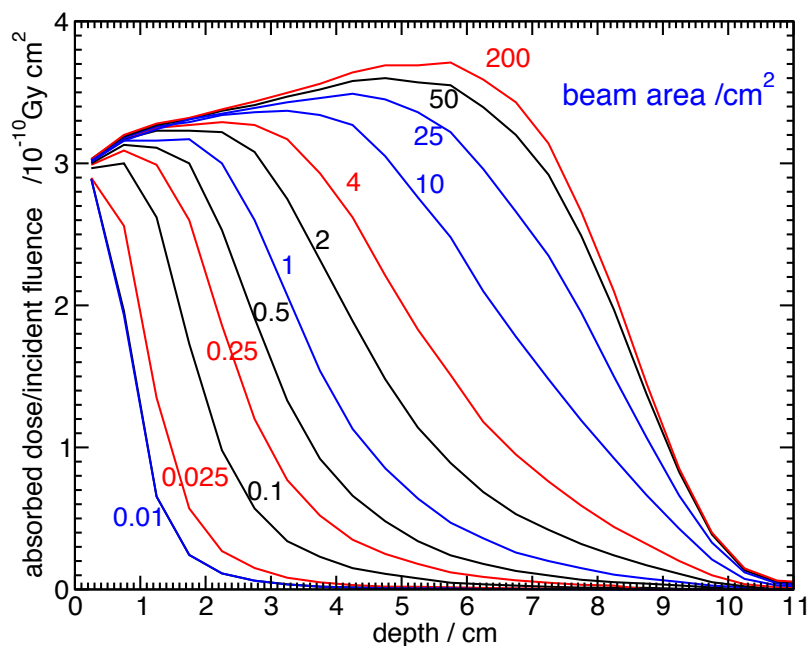


Figure 36: The central-axis depth-dose curve calculated with EGS4 for parallel, circular beams of 20-MeV electrons incident normally on water. The beam areas are shown in square centimeters.

time. A comparison of two such codes, EGS and ETRAN, will serve to illustrate some of these compromises as well as the limitations of these particular codes, both of which are in wide use.

A major difference between EGS and ETRAN (and its descendants, in particular the ITS system) is one of overall system design. The EGS system (Ford and Nelson, 1978; Nelson et al., 1985) is a package of subroutines which simulates electron and photon transport. It provides users with a well-defined interface to specify their own geometry and to score the physical parameters of interest. This has the drawback of requiring users to write their own user's code (or find an existing code which addresses their problem) but it makes the system very flexible. In contrast, the distributed versions of ETRAN (Berger and Seltzer, 1973) or ITS (Halbleib and Melhorn, 1984) come as complete codes which allow the user to select one of a wide variety of geometries and elect a variety of outputs (energy and charge deposited, fluence spectra in each region, spectra of particles escaping from the geometry, etc.). This makes the codes easier to use initially since they can be treated as "black boxes," but it restricts the user's options and ability to get information. For example, the EGS results on the origin of different dose components shown in Figs. 28 and 29 could not be obtained with the ETRAN-based codes without detailed knowledge of the inner workings of the code.

There are also many differences in how the codes simulate electron and photon transport, often reflecting the different origins of the two codes. Although both systems now cover much wider energy ranges, ETRAN was originally designed for the energy regime below a few mega-electronvolts, whereas EGS was a high-energy physics code designed for energies up to the giga-electron-volt region. In what follows we concentrate on differences in algorithms, although there are also some differences concerning the cross sections which we will not discuss because they are "inputs" to the codes and can be changed.

II.G.1. Class I Versus Class II Algorithms

In Section II.A.5 considerable emphasis was placed on the distinction between class I codes, in which the energy and direction of the primary charged particle are not correlated with the creation of secondary particles, and class II codes, in which there is such a correlation. EGS uses class II algorithms, whereas ETRAN uses a class II algorithm for bremsstrahlung production and a class I algorithm for the production of knock-on electrons. Collision-induced energy-loss straggling is described by sampling from the Blunck-Leisegang modification of the Landau energy-loss straggling distribution, L(BL). Unfortunately, in all versions prior to

1987, there was an error in the L(BL) distribution which caused the mean energy loss to be underestimated. This led to about a 7% underestimate of dose near the surface for 10-20-MeV electrons on water and caused about a 4% underestimate of R_{50} , the depth at which the dose drops to 50% of its value (see Rogers and Bielajew, 1986, for details). This error was not a fundamental problem and was corrected in ETRAN in 1987 (Seltzer, 1989) and in Version 2.1 of the ITS system.

The choice of class I or class II models can lead to real differences, which are, however, rarely significant. Consider the average energy as a function of angle of 20-MeV electrons passing through a thin (0.2-mm) plate of titanium (e.g., the exit window of a linac). The average energy lost by electrons passing through the plate is 236 keV. For a class I code, this would be the average energy lost by electrons emerging from the plate at any angle (except for small differences due to increased path length in the plate). In a class II code such as EGS, this is not the case because electrons which create knock-on electrons are deflected and lose energy. Hence, the electrons at larger angles have a lower average energy and, more importantly, the electrons near the central axis will have lost less energy. Figure 37 shows the magnitude of the differences between the two models as well as the number of electrons at each angle. These differences between the average and actual energy loss are not large. For example, the calculation of electron beam energy after the beam has passed through accelerator exit windows, air, and possibly scattering foils can be done properly only with a class II algorithm. However, this distinction between EGS and ETRAN does not play a significant role.

The class II algorithm in EGS has a slight inconsistency. The multiple scattering formalism includes a term to account for scattering from atomic electrons, but scattering from these electrons is accounted for explicitly when knock-on electrons above the threshold energy are created. Although this scattering is counted twice, the effect is small (Rogers, 1984a).

II.G.2. Multiple Scattering

The other major distinction between EGS and ETRAN is found in the multiple-scattering formalisms used to account for angular deflections caused by elastic scattering from nuclei. EGS uses the Moliere (1948) theory, whereas ETRAN uses the theory of Goudsmit and Saunderson (1940). Berger (1963) gives a good overview and comparison of the two theories and Berger and Wang (1989) extend the comparison.

The theory of Moliere contains a small-angle approximation and also requires a certain minimum number of scattering events to occur. Hence it can be applied only in a certain range of step sizes. Also, it does not

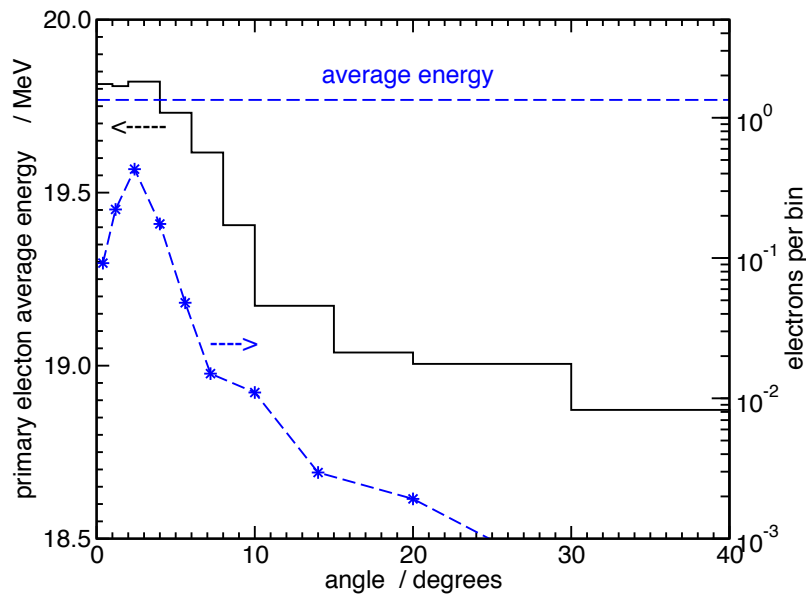


Figure 37: Average energy (histogram) and number (stars) of primary electrons per bin as a function of angle after 20-MeV electrons pass through 0.2 mm of Ti, as calculated using the class II algorithm in EGS. To first order, a class I algorithm would calculate a constant average energy (dash).

distinguish between electron and positron scattering. In comparison, the Goudsmit-Saunderson theory is exact for a given single-scatter cross section, can be evaluated in terms of a Legendre series, and can distinguish between electron and positron scattering (although ETRAN does not use this feature). However, Bethe (1953) showed how to compensate for the effects of the small-angle approximation and Berger (1963) has shown that, in practice, there is often little difference between the two theories. Figure 38 shows Berger's calculated comparison for 1-MeV electrons and positrons incident on a thin aluminum plate. Similar good agreement between angular distributions calculated with EGS and ETRAN for low-energy electrons passing through a thin slab of water has been reported (Rogers, 1984a).

As discussed in Section II, multiple scattering plays a major role in defining the shape of the depth-dose curve for broad beams of electrons, especially if energy-loss straggling is turned off. To investigate the effects of the different multiple-scattering theories used in EGS and ETRAN, we

have calculated a series of depth-dose curves for electrons on lead and water with these two codes. We turned off the production of all secondary particles and energy-loss straggling to obtain CSDA calculations which emphasize differences in multiple-scattering formalisms. Figure 39 shows that the two multiple-scattering formalisms produce very similar results in water over a wide energy range. Figure 40 shows a similar comparison for electrons on lead. Here, discrepancies of up to 11% of the peak dose occur. These discrepancies are due in part to the different collision stopping powers used in the two codes, those used in EGS being -2% smaller above a few mega-electron-volts. The reason for the remaining differences is probably to be found in the multiple-scattering formalisms, although other causes may contribute. In particular, the EGS calculations in lead must be done using the PRESTA algorithm (at least below 5 MeV) because the minimum step size for which the Moliere theory is valid is so large that path length corrections are essential. These differences warrant further investigation.

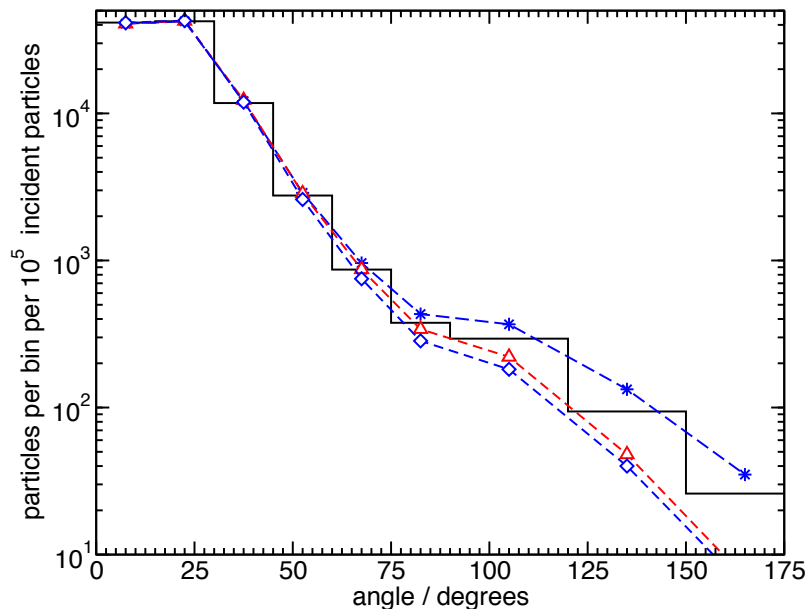


Figure 38: Calculated angular deflections for 1-MeV electrons and positrons passing through 0.029 g/cm^2 of aluminum. The histogram shows the Moliere results and the symbols show Goudsmit-Saunderson results for different cross sections: stars, Rutherford cross section; triangles and diamonds, e- and e+, respectively, using the Mott cross sections. Data from Berger (1963).

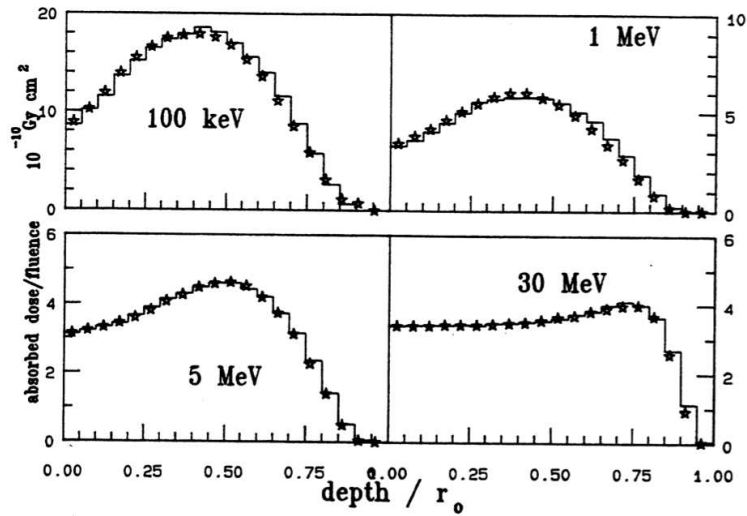


Figure 39: A comparison, at various energies, of the depth-dose curves for broad parallel beams of electrons on water, calculated using the Goudsmit-Saunderson multiple-scattering formalism in ETRAN (histogram) and the Moliere multiple-scattering formalism in EGS4 (stars). In both cases, the calculations were done in the CSDA approximation without secondary particles or energy-loss straggling. The depth axis is in terms of the CSDA range, r_0 . The EGS4 calculations used the PRESTA algorithm (Bielajew and Rogers, 1986a, 1987).

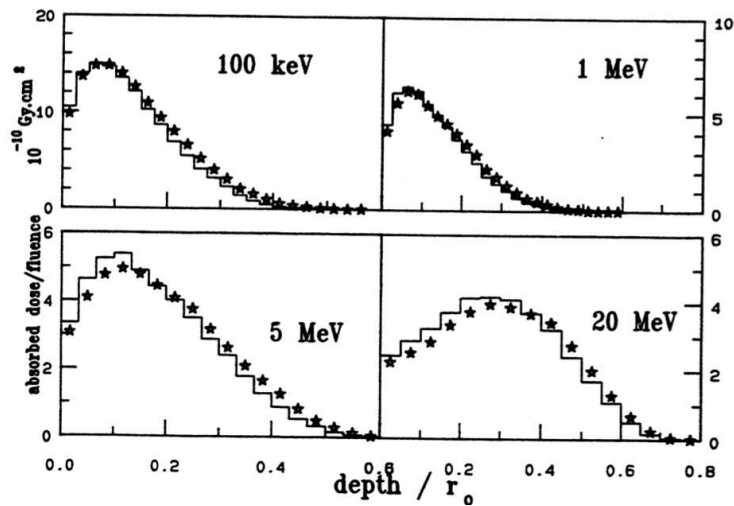


Figure 40: Same as Fig. 39 except for beams of electrons on lead.

II.G.3. Transport at Low Energies and Termination of Histories

Generally speaking, ETRAN handles low-energy transport more accurately than does EGS, although there are exceptions [in particular, EGS4 has an option to include coherent (Rayleigh) scattering of photons, a process which ETRAN lacks]. Both codes contain aspects which are based on the assumption that electrons are unbound (e.g., electron inelastic-scattering cross sections and differential Compton-scattering cross sections). Hence, in any situation where electron binding is comparable to the energy of the particle being transported, one must exercise care with both codes. This is especially true of electron transport in high-Z materials, where there are large uncertainties in the stopping powers and interaction cross sections below 100 keV. Even more important are the approximations contained in the overall model of the transport. One must use extreme caution when interpreting the results of any calculations in which the details of electron transport in this regime play a significant role.

One major difference in the low-energy transport models is that the standard version of EGS does not include the creation of fluorescent photons and Auger electrons, whereas ETRAN does. ETRAN considers K-shell ionization caused by the photoelectric effect and by electron impact ionization and then accounts for production of fluorescent x rays and Auger electrons from the highest-Z element in the material. For situations in which fluorescent x rays are important (e.g., fluorescent escape peaks in detectors for low-energy photons), Nelson et al. (1986) have written a subroutine which extends EGS4 to follow fluorescent x rays (also just from the highest-Z element in the material) after photoelectric events have created K-shell vacancies. The code SANDYL (Colbert, 1974) and some of the ITS codes (the P codes; see Halbleib and Melhorn, 1984) consider electron ionization of all shells, and atomic relaxation from the K, L, M, and N shells is explicitly taken into account (see Halbleib and Morel, 1978). These additions require considerable core space and increased run time, but Halbleib and Melhorn report that “in the vast majority of problems, the P-codes give results that are virtually identical to those of the standard codes” (which use the ETRAN model).

Another difference between the ETRAN-based codes and the standard EGS code is that EGS does not sample the angular distribution of photoelectrons whereas ETRAN does. We have written a subroutine to extend EGS4 for this purpose (Bielajew and Rogers, 1986d) but find that it rarely has a large effect because the multiple scattering of these low-energy electrons tends to dominate their angular behavior.

In the ETRAN-based codes, when an electron history is terminated for falling below the cutoff energy, its kinetic energy and charge are deposited at a point along its current direction and at a distance randomly chosen from a uniform distribution up to the residual practical range of the electron. In some situations this allows a significantly higher cutoff energy to be used in ETRAN than in EGS, where a particle history is terminated at the end of the step during which its energy fell below the cutoff.

Another difference in the low-energy transport of the two codes is the use, in the ETRAN codes, of the Elwert correction factor to modify the Bethe-Heitler bremsstrahlung cross sections taken from Koch and Motz (1959). This Coulomb correction factor increases the bremsstrahlung production at low energies. Although the approximations inherent in its derivation restrict it to low energies, Berger and Seltzer (1970) applied it up to 15 MeV because it improved agreement with experimental results. The latest version of ETRAN (Seltzer, 1989) uses a new set of bremsstrahlung cross sections based on their own evaluation (Seltzer and Berger, 1986). Even without the Elwert factor, EGS overestimates by 40% the bremsstrahlung production from 2-MeV electrons incident on a thick tungsten target (Ewart and Rogers, 1982; see Fig. 50 below). Similarly, for 2-MeV electrons on a 3-mm slab of silicon, EGS predicts more bremsstrahlung than does ETRAN. At 4 MeV and above the differences are small and, in particular, the predicted backward bremsstrahlung is similar for both codes (Rogers, 1984a). However, with the exception of cases which isolate the bremsstrahlung from low-energy electrons, this shortcoming in EGS is not a major problem because the bremsstrahlung yield from low-energy electrons is only a small fraction of the energy loss and a small fraction of the total bremsstrahlung production from an electron slowing down from higher energies (see Fig. 15).

A final difference in the low-energy transport is that EGS4 has an option to include coherent (Rayleigh) photon scattering, whereas the ETRAN-based codes (except SANDYL) do not. In order to maintain generality, the EGS code assumes that coherent scattering occurs from independent atoms. This can be a good approximation in non-crystalline elements but causes problems in materials which have molecular or other order in the system, such as liquid water (Johns and Yaffe, 1983). In general, it has been found that coherent scatter of low-energy photons has a significant effect on the transmitted and reflected photons (see, e.g., Persliden and Alm Carlsson, 1984; Williamson et al., 1984) but that energy deposition is not significantly affected for broad beams. Figure 41 presents some EGS4 calculations with and without coherent scattering

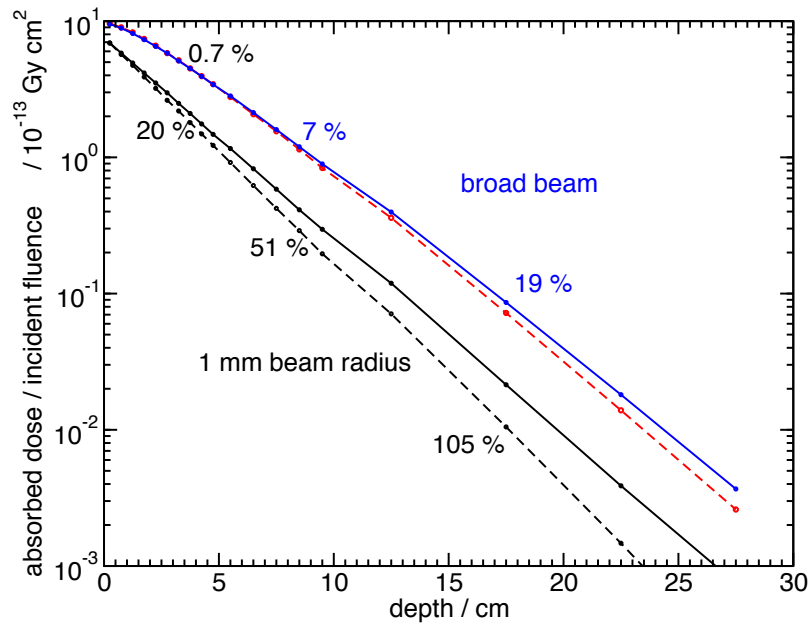


Figure 41: Central-axis depth-dose curves calculated with (dash) and without (solid) coherent (Rayleigh) scattering in EGS4 for 30-keV beams of photons on a 30-cm-thick water phantom for incident 1-mm-radius and broad beams. Percentage differences (shown) between the two calculations are much greater for the narrow beam because the coherent scattering removes photons from the beam even though it causes no energy deposition.

which show that for narrow beams, coherent scattering can have a considerable effect. However, this is for the photon energy at which coherent scattering plays its greatest role in water (see, e.g., Fig. 11) and at 100 keV the effect, even for the narrow beam, is reduced by an order of magnitude and is always much smaller in broader beams.

II.G.4. Step Sizes, Boundary Crossings, Variance Reduction, and Timing

ETRAN and EGS use different approaches for selecting electron step sizes. In ETRAN, major step sizes for electron transport are chosen so that, on average, electron energy decreases by a constant fraction, usually $2^{-1/8}$ ($= 0.917$). For this step, the energy lost by the electron is determined by sampling from the energy-loss straggling distribution. Within this major step, a series of n substeps of equal length are taken. The value

of n increases with Z , typically being 4 for Al and 16 for W, since smaller steps must be taken with higher Z to ensure that the electron transport is accurate without a path length correction (cf. Section II,C). For each of these substeps the appropriate distributions are sampled to determine the deflection due to multiple scattering and whether a knock-on electron or bremsstrahlung photon is produced, or whether K-shell ionization has occurred. If any secondary particles are created, the appropriate differential cross sections are sampled to determine the particle energies and directions. Their points of origin are selected randomly along the substep, but the step length of the primary electron is not affected. Only in the case of bremsstrahlung production does the creation of a particle directly affect the energy of the primary electron; in the other processes this energy loss is already included in the Landau energy-loss straggling formalism.

In ETRAN, a material boundary is usually crossed in the middle of a substep. When this occurs, the energy loss is recomputed for the distance up to the boundary, and the last substep is shortened to cause it to end on the boundary. The multiple-scattering deflection in this substep is then sampled using a Gaussian approximation since the Goudsmit-Saunderson formalism cannot be sampled for arbitrary step sizes during a simulation.

ETRAN's technique of more or less fixed step size selection makes it possible to introduce a variety of variance reduction techniques directly into the standard version of ETRAN. For example, one can easily create more bremsstrahlung photons or knock-on electrons by artificially increasing the cross sections (see Section IV,C).

In contrast, EGS allows all physical processes as well as boundaries to affect the choice of electron step sizes. This is possible because the Moliere multiple-scattering formalism can be used during the simulation to determine the deflection for an arbitrary step size within its region of applicability. EGS first samples the appropriate cross section to determine the distance to the next discrete interaction on the assumption that it stays within the current material. It then selects a step size which is the shorter of this distance or the maximum step size allowed by the multiple-scattering theory (or related constraints such as ESTEPE, the maximum continuous energy loss per step; see Section II,C). Finally, if the current step size would cause the electron to cross a boundary, the step size is reduced to make the electron stop on the boundary. The code then transports the electron through this step, takes into account multiple scattering, and finally allows the discrete interaction to be simulated if that was what defined the step size.

This step-size algorithm is very different from that in ETRAN, but aside from differences between class I and class II models, the different step-size algorithms do not appear to lead to different results.

The standard version of EGS uses no variance reduction techniques; i.e., it is a completely analog model. However, it is designed to allow users to implement whatever techniques they find useful (see Section IV).

It is appropriate to consider the question of timing in this section because timing is almost entirely determined by the number of electron steps taken, and this parameter is under the user's control to a greater or lesser extent. For example, if one uses the standard versions of EGS or CYLTRAN to calculate photon response functions for scintillation detectors (see Rogers, 1982), one finds that EGS runs about five times faster for comparable accuracy. However, this is only because EGS uses much larger electron step sizes. Although this means that the details of the electron transport are inaccurate, it does not affect the results in this case. In general, the two codes are comparable in speed (within a factor of 2) for calculations which require similar accuracy in electron transport -i.e., if, in EGS, we adjust the energy loss per step, ESTEPE, to be similar to that used in ETRAN.

The above comments apply when variance reduction has not been introduced and when using a VAX single-precision version of CYLTRAN (Halbleib and Vandevender, 1976a) or the double-precision version of CYLTRAN from the ITS package (Halbleib and Melhorn, 1984) and the standard EGS4 code (with ESTEPE). If we use the PRESTA algorithm with EGS4 (Bielajew and Rogers, 1986a, 1987), we can get factors of up to 5 improvement in computing efficiency in favorable cases. Hence we expect this code usually to be faster than the ETRAN-based codes, except where the built-in ETRAN variance reduction techniques are important.

II.G.5. Other Differences

The ETRAN-based codes consider electrons and positrons to be the same except that positrons annihilate, creating two 511-keV photons, when their histories terminate. The EGS system explicitly takes into account the differences between the electron and positron stopping powers and the Moller and Bhabha scattering cross sections. In some cases these differences cannot be ignored. For example, the maximum dose from broad beams of 100100-MeV positrons on tissue has been shown to be about 5-8% less than that for electrons (Rogers, 1984b). Perhaps more important, even after ignoring the effects of annihilation radiation (which cause the overall response to positrons to be very different from that to electrons), the response of a germanium detector for positrons is significantly different from that for electrons. For example, for a 4-MeV source the calculated full energy absorption peak for incident positrons is 13%

lower than that for electrons (Rogers, 1984a). This fact must not be ignored when calculating response functions for positrons, a fairly common situation in spectroscopy.

EGS also takes into account positron annihilation in flight. The only study we know of which directly compares results with and without this process indicates that it is not a major effect. Grosswendt and Waibel (1975) considered its effect on the double-escape-peak efficiency of a Ge(Li) detector.

III. Code Accuracy

III.A. CROSS-SECTION DATA

Ultimately, no matter how well the Monte Carlo code works or how much physics it models, the quality of the calculated results will be limited by the quality of the cross sections employed. Any result calculated by a Monte Carlo program should be analyzed with some knowledge of the intrinsic errors in this most basic component of the code. In this section we discuss the accuracy of the available photon and electron cross-section data. Additional errors derive from how the Monte Carlo code tabulates, fits, and accesses the data. For example, EGS has a discontinuity of several percent in the photon cross section at 50 MeV because it uses data from different sources above and below this energy (see Rogers, 1984b). EGS also has severe problems fitting the photon cross-section data near the photoelectric absorption edges if it is simultaneously fitting cross sections above several hundred mega-electron-volts. This is because the grid in some of the fitting procedures becomes too coarse, not because of any inaccuracy in the cross section.

In this section we do not consider the effect of making approximations that neglect some of the relevant physics in the energy range of interest. Every code is different in this respect and such approximations have already been discussed for the general-purpose EGS-and ETRAN -based codes.

In the next few paragraphs we present an overview of the uncertainties in various cross-section data. The uncertainties these produce in the final results are very hard to determine. As an extreme example, a 50% error in the electron stopping power below 2 MeV would have virtually no effect on a calculated depth-dose curve for 10-MeV photons because these electrons have a short range and deposit all of their energy locally. The

user must always analyze the problem at hand to determine how uncertainties in cross sections affect the overall uncertainty.

III.A.1. Photons

The estimates of uncertainty for the photon total cross sections come from Storm and Israel (1970) and Hubbell (1982). In the region where the photoelectric effect dominates (consult Section II,A,2), the uncertainty is 3-5%. Although there is 3% uncertainty associated with coherent scattering in this region, the overall uncertainty is entirely dominated by the photoelectric cross section. In general, for the energy region dominated by Compton interactions the cross sections are accurate to about 2-3%. However, for the light elements normally associated with radiation dosimetry and therapy, the uncertainty may be less than 1%. The cross section for pair production should be accurate to about 5% but in the energy region up to 30 MeV one must be aware of the uncertainty in the total cross section associated with the omission of photonuclear processes (see Section II,A,2).

III.A.2. Electrons

As discussed in ICRU Report No. 37 (1984b), the uncertainty in the electron and positron collision stopping power is governed by the inaccuracy of the inelastic-scattering cross section and the approximations inherent in how the statistical theories sum the many small energy losses. At low energy, between 10 and 100 keV, the ICRU estimates the uncertainty to be 2-3% for low-Z materials and 5-10% for high-Z materials. Above 100 keV, the uncertainty is estimated to be 1-2%. The uncertainty in the radiative stopping power arises totally from the uncertainty in the bremsstrahlung cross section since the former is an integral of the latter. The uncertainties in the ICRU radiative stopping powers are expected to be about 5% below 2 MeV and 2-5% between 2 and 50 MeV. Codes such as EGS4 and the ITS system, which use older bremsstrahlung cross section data, will have considerably larger uncertainties and errors in the radiative stopping powers, especially at low energies.

III.B. OTHER SYSTEMATIC AND STATISTICAL UNCERTAINTIES

Aside from errors in the cross-section data, several other sources of error are inherent in Monte Carlo calculations, both systematic and statistical

in nature. Too often, systematic errors are not considered and one tends to lend too much credence to Monte Carlo results. We enumerate the various sources of systematic errors in the first part of this section.

Since Monte Carlo calculations simulate physical processes by sampling from particle-matter interaction cross sections in a stochastic fashion, the calculated results are subject to statistical uncertainties. In the second part of this section we describe how to calculate these statistical uncertainties. .

In the final part of this section we describe a method for quantifying computing efficiency. This is useful for determining the improvement obtained by using variance reduction techniques (discussed in Section IV), for comparing the execution speeds of different computers running the same simulation, or for estimating the computing time required to obtain a desired statistical accuracy.

III.B.1. Systematic Errors

a. Programming Errors. Monte Carlo codes are large, complicated, integrated systems of software. No large computer code is free of errors or works exactly as intended. One major advantage of employing widely used codes is that they have been checked in a variety of applications. This does not mean all the errors have been found, and users of these codes should document and communicate any errors they find to the authors of the codes.

b. Modeling Inaccuracies. Inaccuracies are often associated with the analytic components of the simulation and reflect the inherent approximations. Until 1987 the Blunck-Leisegang (1950) extension of the Landau (1944) energy-loss straggling theory used by ETRAN and its descendant codes contained an error, the effect of which can be seen in Fig. 5 (Rogers and Bielajew, 1986; Seltzer, 1989). Also, the electron path length curvature correction in EGS is known to overestimate the curvature (Bielajew and Rogers, 1986a, 1987). Fortunately, this latter error and inaccuracies in some other important aspects of electron transport (discussed in Section II,C, 1) are greatly reduced if sufficiently small electron step sizes are employed.

As well as errors in the model employed (as in the above two examples), there are well-known limits to many of the models used. For example, many codes do not include coherent scattering or binding effects in Compton scattering. These are insignificant problems for many calculations

but could be critical in certain applications. One must always carefully investigate the limitations of any code being used.

c. Roundoff and Truncation Errors. Sometimes difficulties can occur because of the finite precision of real numbers as represented by digital computers. For example, if poorly coded when using 32-bit single-precision floating-point numbers,

$$x = 1 + \sum_{i=1}^{1,000,000} x_i \quad (8)$$

where $x_i = 10^{-8}$ for all i , gives the answer $x = 1.00$, not 1.01 as expected. Accumulation variables used in this fashion should be set to double precision. Truncation errors sometimes cause problems with the geometric transport of particles. For example, a particle may be expected to be in one geometric region when truncation causes it to be in another. Well designed geometry codes minimize this kind of error and can detect and correct these errors when they occur. Double-precision coding-helps in this case but does not eliminate the problem.

III.B.2. Statistical Uncertainties

A Monte Carlo result, like any experimental result, is of virtually no use unless some estimate of its statistical uncertainty is given. While there is no rigorous theory on how to assign this uncertainty, it is common practice to break a Monte Carlo run into a number (N_B) of independent batches, each considering the same number of histories, and to calculate an estimate x_i for each quantity of interest for each batch. With N_B such estimates, the final estimate of x is the average $\langle x \rangle$ of the x_i values. On the , assumption that the X_i are drawn from a normal distribution, the best estimate of the variance of the mean σ^2 is given by

$$s_{\langle x \rangle}^2 = \frac{1}{N_B(N_B - 1)} \sum_{i=1}^{N_B} (x_i - \langle x \rangle)^2 \quad (9)$$

Note that s^2 is an estimator of the true variance σ^2 . For $N_B \geq \sim 10$ one can assert that the interval $(\langle x \rangle - s, \langle x \rangle + s)$ contains the true value of the mean in about 68% of all cases, or 95% of all cases for $\pm 2s$. There appears to be some dependence of s on the choice of N_B (which should be 10 or larger). Therefore, when publishing results one should indicate what N_B was used.⁶

⁶Since this was written, a much improved method has been developed, see Walters et al, History by history statistical estimators in the BEAM code system Med. Phys. 29 (2002) 2745-2752.

To combine the results and uncertainties of m independent runs, the following formulas apply:

$$\langle x \rangle = \sum_{k=1}^n \frac{N_k}{N} \langle x \rangle_k \quad (10)$$

and

$$s_{\langle x \rangle}^2 = \sum_{k=1}^n \left(\frac{N_k}{N} \right) s_{\langle x \rangle_k}^2 \quad (11)$$

where N is the total number of histories and the subscript k indicates that the variable is associated with the k -th independent run. Equation (11) requires the additional assumption that the uncertainties are relatively small, being a lowest-order approximation.

We have found that calculated uncertainties greater than 5% or so tend to be slight underestimates. Uncertainty estimates below this appear to be more accurate and qualitatively agree with what one expects if the distribution of the x_i was truly normal.

However, one must be wary of placing too much faith in these uncertainty estimates. We have discovered many exciting effects which were statistically significant at the 95% confidence level. Further computing has “made the effect go away,” indicating that it was one of the 5% of calculations which are more than two standard deviations away from the expectation value. Also, one must take care to recognize when results are correlated. For example, when calculating a depth-dose curve for high-energy photons, if there happens to be a large number of photon interactions in one bin, this may show up as a high dose in several adjacent bins at greater depth.

III.B.3. Computing Efficiency

On the assumption that the individual batch estimates are drawn from a normal distribution, in the limit of a large number of histories, the quantity $N\sigma^2$ is a constant. It is usual to assume that Ns^2 is also a constant. Thus, for a given calculation, the estimated uncertainty is roughly proportional to the inverse of the square root of the number of histories used. One can use this relation to estimate the number of histories it would take to reach a result with a certain precision, given that one already has one estimate for it with poorer statistics.

The above relation also permits a useful definition of the efficiency of a Monte Carlo calculation:

$$\epsilon = \frac{1}{Ts^2} \quad (12)$$

where T is the computing time to obtain a variance estimate s^2 . If the calculation technique remains the same, ϵ should be constant as long as N is large. The reason this definition is useful is that when one introduces variance reduction techniques (see Section IV), the computing time for a given number of histories will usually increase. However, if the product Ts^2 decreases, there has been a net improvement in computing efficiency (i.e., the time to achieve a given s^2 has decreased or, alternatively, the s^2 achieved in a given time has decreased).

III.C. EXPERIMENTAL BENCHMARKS

Electron transport and photon transport are extremely complicated physical processes and the Monte Carlo codes used to simulate them are also very complex. It is essential to evaluate such Monte Carlo codes by comparing calculated data with high-quality experimental data in order to eliminate coding errors, to help refine algorithms, and, most important, to estimate the systematic uncertainties associated with approximations in the codes.

Unfortunately, it is often very difficult to find experimental data which are of sufficiently high quality, or have a simple enough configuration, for meaningful comparisons between calculations and experiment. It is preferable to have high-quality data in very simple geometries in order to do the most meaningful comparisons—and yet these data are still rare. Very few practical radiation sources are monoenergetic or even consist solely of one type of radiation, and yet most Monte Carlo calculations start with just such a source. While the limitations on source and geometry in the calculations are now being overcome, this consideration often makes the interpretation of comparisons complex.

Another complicating factor is that certain experimentally measured quantities are poor indicators of the overall accuracy of all the components of a calculation; i.e., good agreement with experiment for some calculated quantity does not verify the accuracy of the entire calculation. For example, conditions of electron equilibrium in a photon beam imply that features such as absorbed dose are often very insensitive to the electron transport part of the calculation. Thus, examination of these dose values is a poor test of the electron transport algorithm.

A further complication is that the various components of the particle transport play much different roles in various materials or in different energy ranges. For example, multiple scattering is much more important in high- Z materials, and validation of a calculation in a material with one Z does not necessarily imply that the code will work for the same calculation in a material with a very different Z .

In the following we present data against which electron-photon Monte Carlo codes have been tested. Most of the comparisons we report have been done with codes based on ETRAN or EGS. While these benchmarks prove that these codes are generally quite accurate, it is our opinion that much more work will be required before either code can be used routinely with confidence at the level of a few percent. If this is true of these extensively used codes, it certainly must apply even more strongly to less extensively used codes. Although Monte Carlo techniques have an aura of being the only “right” approach to many calculations in radiation dosimetry problems, a good rule of thumb is “user beware.”

III.C.1. Response Functions for Photon and Electron Detectors

Monte Carlo calculation of the response functions of photon or electron spectrometers, such as NaI or Si detectors, has a long history. Because of the existence of high-quality experimental data, this is a good benchmark for certain aspects of the Monte Carlo technique. Both EGS and ETRAN have been carefully studied in this context (see Rogers, 1982, 1984a; Berger et al., 1969; Berger and Seltzer, 1972). For photon detectors, it has been shown that EGS and ETRAN are in good agreement with each other except for small differences between calculated escape peak efficiencies at higher energies (Rogers, 1982). These differences are of no practical consequence but may reflect the more accurate treatment of positron transport in EGS (see Section II,G,5). Figures 42 and 43 present comparisons with experimental data in which no normalization parameters are introduced; i.e., the comparisons are absolute. For 662 keV γ rays from a ^{137}Cs source the agreement is excellent as long as the effects of the beryllium β -ray shield between the source and the NaI detector are taken into account. The backscatter from the wall behind the source leading to a peak at ~ 250 keV and the low-energy characteristic x rays from the source (~ 30 keV) were not included in the model. In this case electron transport plays a negligible role. As shown by Fig. 43, at 6.13 MeV the agreement with experiment is excellent above 4 MeV. In this case the integrated counts above 4 MeV are reproduced within the 2% uncertainty in the measurement. The inclusion of electron transport has roughly a factor of 2 effect on the calculated number of counts in the full energy peak. At lower energies in the response, the observed effects of photons interacting in the room, in particular 511-keV annihilation photons from the walls, are substantial but are not included in the calculation.

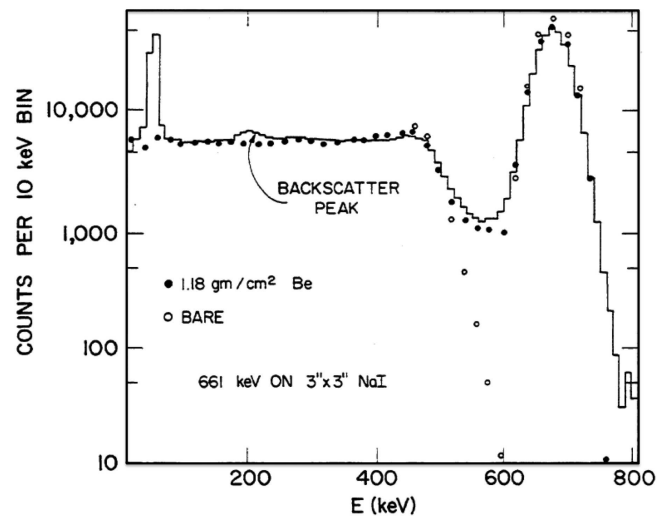


Figure 42: Measured (histogram) and calculated (circles) response of a 3 x 3 in. NaI detector to an isotropic point source placed 10 cm away and emitting 3.07×10^7 photons into 4π with energy 661 keV. The open circles are for calculations with a bare detector and the filled circles include the effects of a $1.18 \text{ g cm}^{-2} \beta$ absorber made of Be. [From Rogers (1982).]

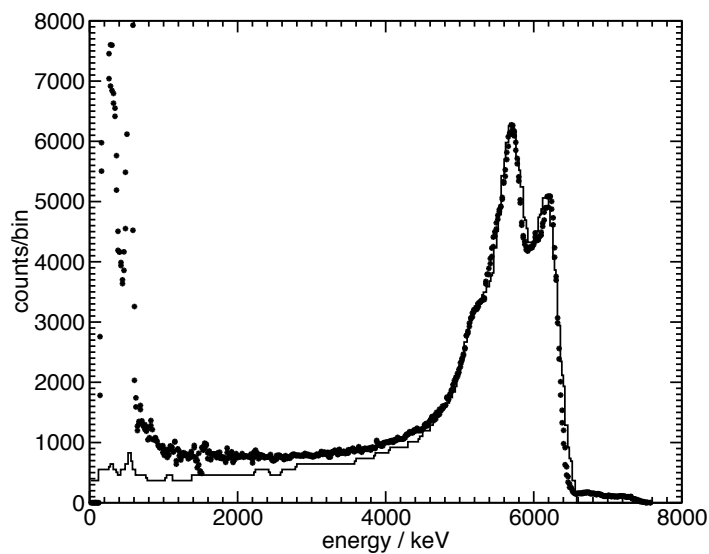


Figure 43: Absolute comparison of the calculated (histogram) and measured (symbols) of a 5x4 inch NaI to a known fluence of 6.13 MeV photons with a 2% contaminant peak at 7.1 MeV.

Monte Carlo calculations have also been shown to predict accurately the relative response functions of germanium detectors, although in this case absolute predictions are less reliable because exact specification of the active region in the detector is not possible (see Debertin and Grosswendt, 1982; Rogers, 1982).

While it is essential to include electron transport when calculating detector response to high-energy photons, the calculations tend to be insensitive to the details of electron transport. A much more severe test of an electron transport code is the calculation of the response function of an electron detector. The most severe test occurs for low-energy electron beams incident on detectors through which some electrons penetrate. The Monte Carlo code must properly calculate electron backscatter, electron transmission, and the bremsstrahlung yield. Figure 44 compares measured and ETRAN-calculated response functions for 500-keV electrons incident on Si detectors of different thicknesses (from Berger et al., 1969). In general, the agreement is very good, although there is some disagreement for detectors which have thicknesses between 10 and 60% of the CSDA range of the electron. EGS has been shown to be in reasonable, but not exact, agreement with the ETRAN calculations (Rogers, 1984a). In particular, it has the same disagreements with experiment as does ETRAN for thin detectors.

Such comparisons with measured detector response functions for electrons represent a severe test of any Monte Carlo code and should be used to evaluate any new code (for measured data, see also Varley et al., 1981; Damkjaer, 1982).

In summary, Monte Carlo codes such as EGS and ETRAN are capable of accurately calculating detector response functions for photon detectors and for electron detectors which are thicker than the CSDA range of the electrons involved.

III.C.2. Photon Depth-Dose Curves

For medical and health physicists, photon depth-dose curves represent an important test of Monte Carlo codes because energy deposition in photon beams is central to these fields. However, these curves are not sensitive tests of electron transport, which plays only a minor role, except in the buildup region where electron contamination of the beam often makes meaningful comparisons with experiment impossible.

Figure 45 presents a comparison by Han et al. (1987) of an EGS calculation and experiment for the depth-dose curve from a $10 \times 10 \text{ cm}^2$ ^{60}Co γ -ray beam. The agreement is excellent. The calculations indicate that

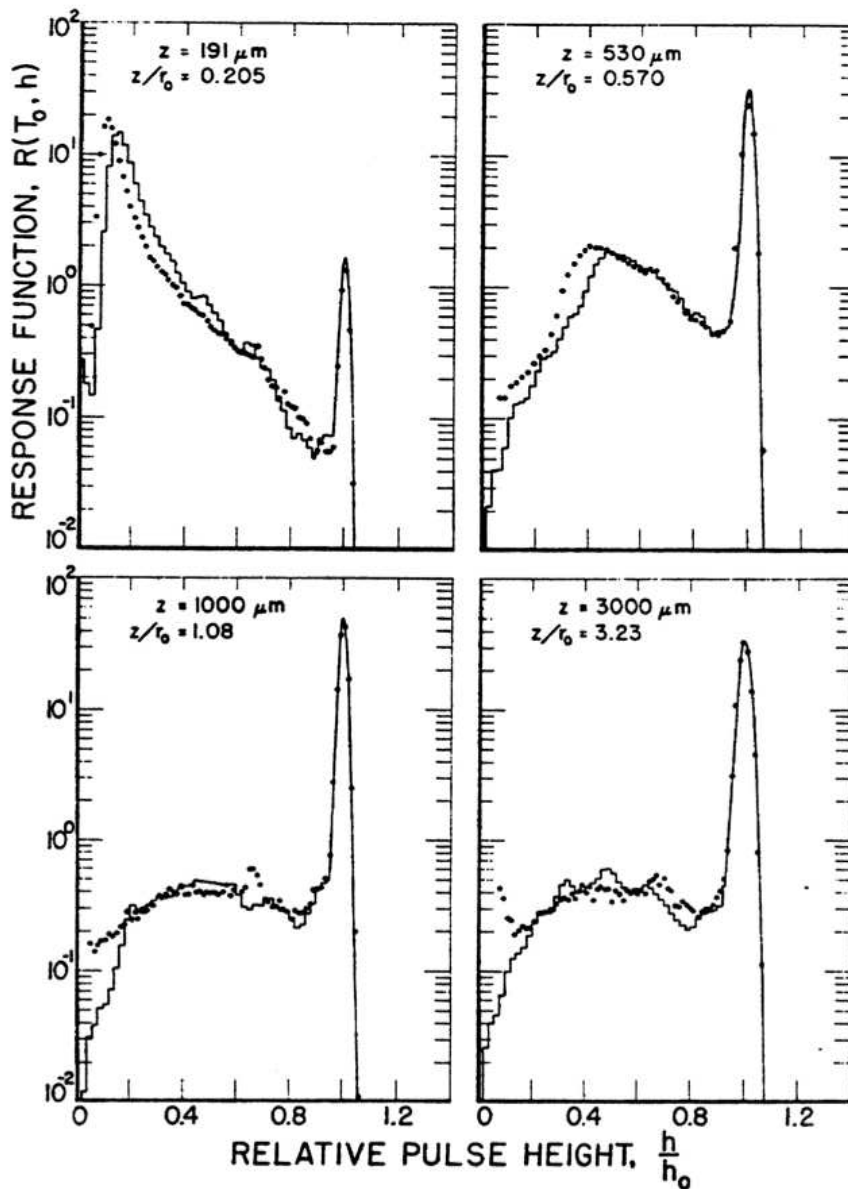


Figure 44: Comparisons of calculated and measured response functions for pencil beams of 500-keV electrons incident normally on Si detectors at different thicknesses Z . The response functions were calculated with ETRAN for semi-infinite slabs and broadened using experimental data. [From Berger et al. (1969b).]

scatter from the source capsule and collimators does not play a major role, although in this case its inclusion makes agreement with experiment slightly worse. In a similar vein, Fig. 28 showed a comparison between an analytic and an EGS Monte Carlo calculation of the dose components versus depth in a broad beam of ^{60}Co γ rays. Again, the agreement was

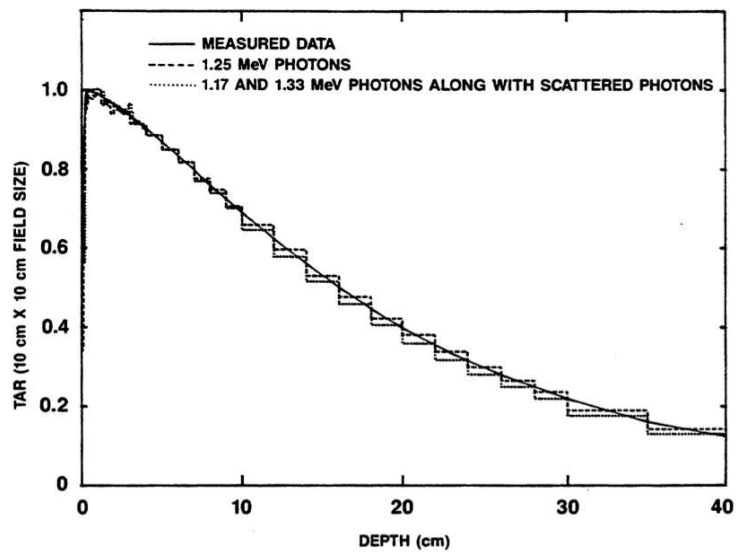


Figure 45: Comparison of measured and EGS-calculated TAR versus depth (essentially $1/r^2$ corrected depth-dose) for a $10 \times 10 \text{ cm}^2$ ^{60}Co γ -ray beam. [From Han et al. (1987).]

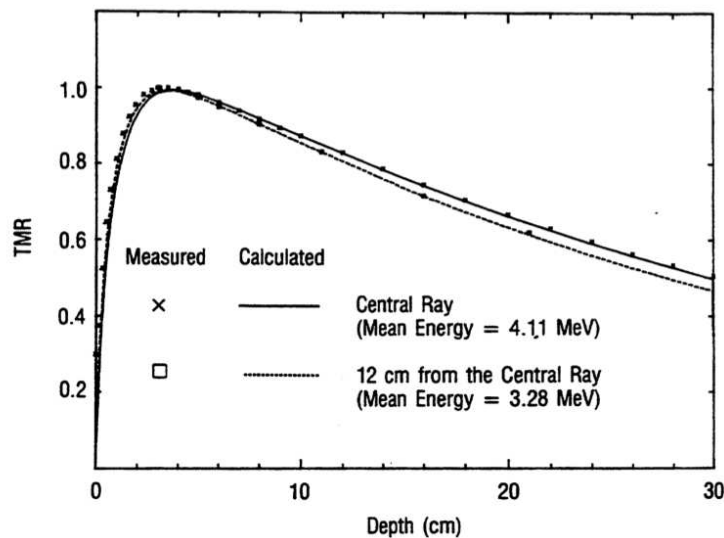


Figure 46: Comparison of measured and calculated TMR versus depth (essentially $1/r^2$ corrected depth-dose) for the 15-MV photon beam from a Clinac-20. Comparisons are given for a $10 \times 10 \text{ cm}^2$ beam on the central axis and 12 cm off axis. The calculations, done with EGS, start from the electron beam incident on a target with backing and include the effects of the flattening filter and collimators. [From Mohan et al. (1985).]

excellent although only the Monte Carlo calculation was capable of including third-order and higher scattering components.

Mohan et al. (1985) have compared EGS-calculated photon depth-dose curves with experimental data for bremsstrahlung from medical linear accelerators. The calculations modeled the generation of the bremsstrahlung beam and the effects of collimators and beam-hardening filters. Several beam qualities were investigated, from 4 to 24 MV. Figure 46 shows the 15-MV calculation of the tissue maximum ratio (TMR) versus experiment. The agreement is excellent, particularly in the falloff region. The off-axis agreement indicates the ability of the code to predict variations in beam quality across the beam. The slight discrepancy in the buildup region was attributed to the presence of contaminant electrons in the incident photon beam.

Figure 47 compares calculated doses in the buildup region of a ^{60}Co γ -ray beam to the experimental data of Higgins et al. (1985), selected because they eliminate the effects of contaminant electrons. The inclusion in

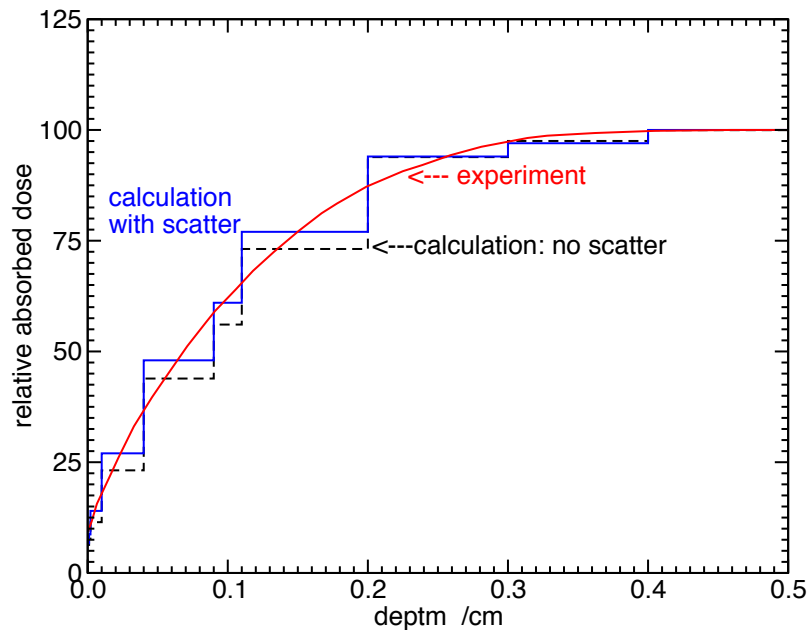


Figure 47: A comparison of measured and calculated buildup region in a ^{60}Co γ -ray beam with no electron contamination. Measurements are from Higgins et al. (1985). Calculations were done with EGS for a monoenergetic beam of 1.25-MeV photons with and without including photons scattered from the source capsule. [From Rogers et al. (1988).]

the EGS calculation of scattered photons from the source capsule makes a small but distinct improvement in the agreement.

In summary, comparisons with experimental data show that Monte Carlo calculations can accurately predict photon depth-dose curves in water-like materials over a wide energy range. While all the above comparisons refer to EGS calculations, it has been shown that EGS is in reasonable agreement with other Monte Carlo codes for photon depth-dose curves (Rogers, 1982), and in the cases in which we have compared EGS and ETRAN (CYLTRAN) results, we have obtained good agreement.

III.C.3. Absorbed Dose per Unit Incident Fluence of 7-MeV Photons

The above comparisons to experimental depth-dose curves are relative; i.e., they compare only the shapes of the curves. Absolute comparisons are difficult since, if a photon source is sufficiently weak that individual photons can be counted, it is also too weak to produce an accurately measurable signal in a dose-measuring device. Mach and Rogers (1984) have reported a precise measurement with a Baldwin-Farmer ion chamber placed at 5-cm depth in a water phantom irradiated by an absolutely known fluence of 7-MeV photons. The photon source was generated using 2.7-MeV protons incident on a CaF_2 target in an ultralight target chamber (see Fig. 48). The $^{19}\text{F}(p, \alpha\gamma)^{16}\text{O}$ reaction produces a triplet of photons between 6 and 7 MeV plus some lower-energy photon contamination ($<10\%$ of the dose). The experiment measures the charge from the ion chamber per unit fluence of 7-MeV photons incident on the phantom with an accuracy of $\pm 1.6\%$ (1σ). One can calculate the dose at 5-cm depth given the incident photon fluence (note that the finite size of the phantom reduces the dose by 2.7% compared to the dose in a semi-infinite slab). One can also calculate the absorbed dose from the measured charge and the exposure calibration factor for the chamber using anyone of a number of dosimetry protocols [American Association of Physicists and Medicine (AAPM), 1983; Nordic Association of Clinical Physicists (NACP), 1980]. A major factor in these protocols is an appropriate stopping-power ratio calculated using a Monte Carlo code (see, e.g., Andreo and Brahme, 1986). Thus, the measured charge and the calculated photon fluence lead to two estimates of the dose, which must agree if the Monte Carlo calculations (and other aspects of the dosimetry protocol) are accurate. Mach and Rogers found agreement well within the measurement uncertainties of $\pm 1.6\%$ when using EGS to calculate the dose from the fluence and

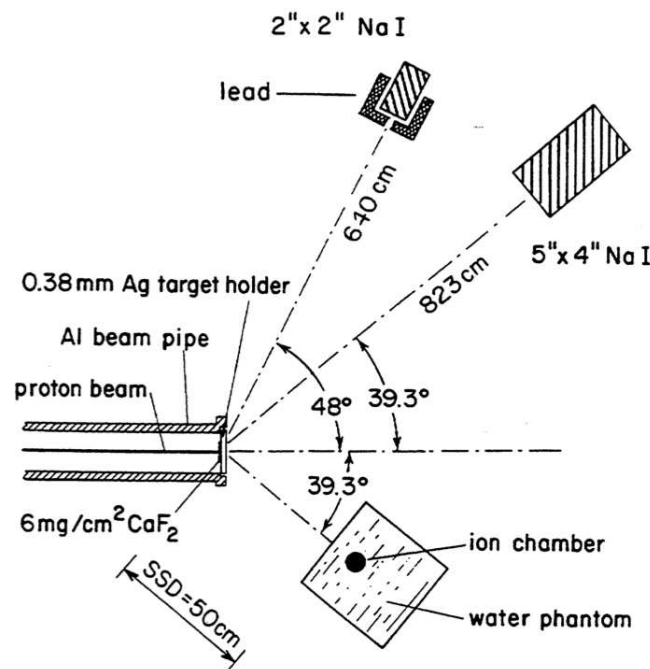


Figure 48: Experimental arrangement for measuring the absolute fluence of nearly monoenergetic photons produced by the $^{19}\text{F}(p, \alpha\gamma)^{16}\text{O}$ reaction induced by 2.7-MeV protons incident on a 6 mg cm^{-2} target of CaF_2 backed by 0.38 mm of Ag. At low beam current the 5 x-4 in. NaI detector measured the ratio of the absolute fluence of 7-MeV photons at 39° to the beam axis per count in the 2 x 2 in. monitor detector. At high beam current there is a measurable ion current (-70 fA) in the Baldwin-Farmer ion chamber placed at 5-cm depth in a water phantom at $\text{SSD} = 50 \text{ cm}$, also at 39° . From the measured ion chamber charge per count in the monitor, one can deduce the ion chamber charge per unit fluence of 7-MeV photons incident on the phantom. [From Mach and Rogers (1984).]

either the AAPM (1983) or NACP (1980) protocols to calculate the dose from the ion chamber measurement. For a proper consistency check, one should use the same Monte Carlo code to calculate all the factors needed for the comparison, but these are not yet available.

III.C.4. Bremsstrahlung Production

The production of bremsstrahlung plays an important role in many simulations. Unfortunately, because of the difficulties in the measurements, not many high-quality experimental data are available. This is also an area in which the models used in various codes are often weak, resorting to empirical scaling factors or simplifications. There has been considerable work in this area by Seltzer and Berger (1986) and the most recent

version of ETRAN (Seltzer, 1989) reflects these new data. The impact of this work on other Monte Carlo codes has not yet been established. In this section we discuss two types of data: (1) thick-target angular distribution data, which test the total production cross section and the electron multiple-scattering model (since the bremsstrahlung photons are given off in nearly the same direction as the electrons which create them), and (2) bremsstrahlung energy spectra, which are primarily a test of the cross sections, differential in energy, and of the sampling routines. .

a. Angular Distribution Data. Wyckoff et al. (1971) have measured, with an accuracy of +5 to 15% the absolute dose to polymethylmethacrylate (PMMA) per unit charge of the electron beam incident on a thick tantalum radiator as a function of depth in the PMMA and angle. Their data are compared in Fig. 49 with calculations using EGS (Ewart and Rogers, 1982). The simulation first calculates the photon spectrum at each

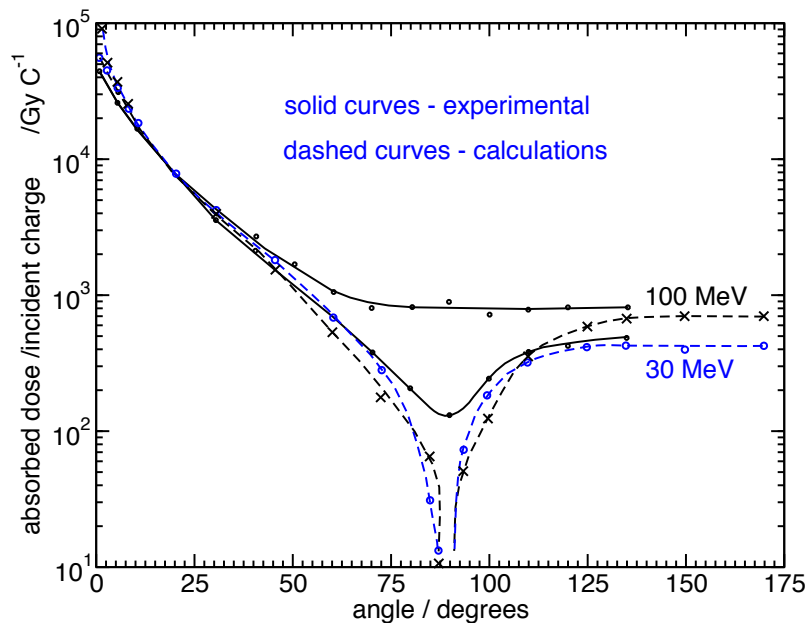


Figure 49: Comparison of calculations and experimental results for the angular distribution of absorbed dose at 4.5 g cm^{-2} depth in a phantom at 100 cm, from 100- and 30-MeV e^- beams incident on stopping thicknesses of Ta. The calculated dip around 90° is due to the infinite lateral extent of the slab in the calculations. The comparison is absolute. The calculated results at 0° are high for the reasons discussed in the text. The calculated dose is in tissue and that measured is for PMMA. [From Ewart and Rogers (1982).]

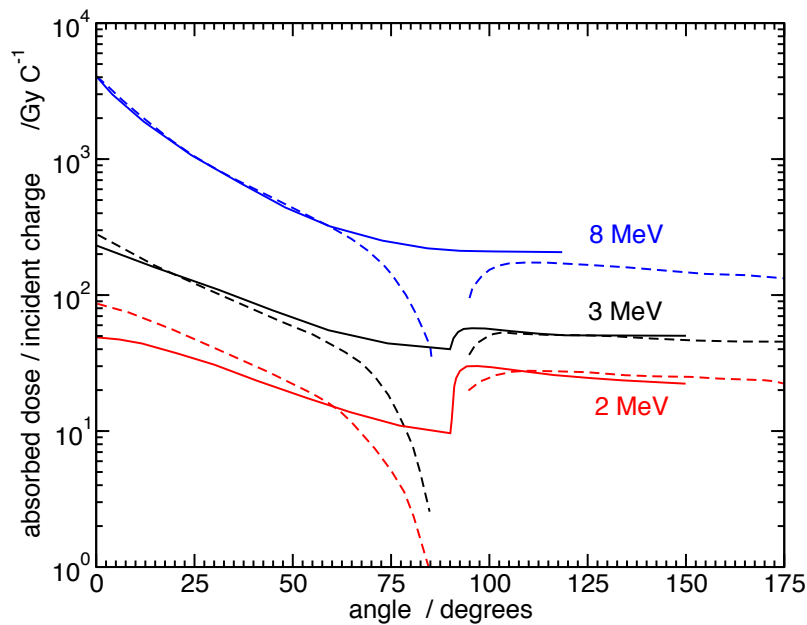


Figure 50: Absolute comparison of calculated (dashed) and experimental (solid) results presented in NCRP Report No. 51 (1977) for the angular distribution of absorbed dose at 4.5 g cm^{-2} depth in a phantom 100 cm from 8-, 3-, and 2-MeV electrons incident on a stopping target of 5.79 g cm^{-2} of W. The discontinuities at 90° are due to the finite thickness of the target. [From Ewart and Rogers (1982).]

angle and then the dose at each depth in tissue, assuming a normally incident broad beam of photons with that spectrum. This approximation leads to an overestimate of the dose at forward angles, where the dose is sharply peaked. Otherwise, the agreement is good. Wyckoff et al. showed that their data were in good agreement with ETRAN calculations for the 30-MeV case. By implication, the EGS and ETRAN results are in good agreement, although this contradicts a result presented by Ford and Nelson (1978) which shows EGS with 50% less energy intensity at back angles, compared with ETRAN, for 30-MeV electrons on a thick tungsten target (their figure 3.3.2).

Figure 50 compares EGS calculations and the experimental data of Bly and Burrill, as presented in National Council on Radiation Protection and Measurements (NCRP) Report No. 51 (1977) for lower-energy electrons incident on tungsten. The agreement is good at 8 MeV but the EGS

calculations overestimate the forward bremsstrahlung production at low energies. As discussed in Section II,G,3, this shortcoming of EGS is significant for problems which isolate the bremsstrahlung from low-energy electrons but is not important in other situations.

b. Bremsstrahlung Energy Spectra. Berger and Seltzer (1970) and Ford and Nelson (1978) have compared the results of ETRAN, EGS, respectively, to some of the available bremsstrahlung spectral data. Generally the agreement is reasonable, but there are discrepancies. Figure 51 presents an absolute comparison of EGS and ETRAN results with some experimental data for electrons on a composite target of tungsten and gold. The shapes are in reasonable accord, although the EGS results are somewhat higher than those from ETRAN and the experiment. This is an area which deserves more detailed work.

III.C.5. Electron Depth-Dose Curves

As the benchmarking of photon depth-dose curves tests the Monte Carlo transport of photons, so does the comparison of experimentally measured and calculated electron depth-dose curves form an important criterion for the reliability of electron transport modeling. Andreo and

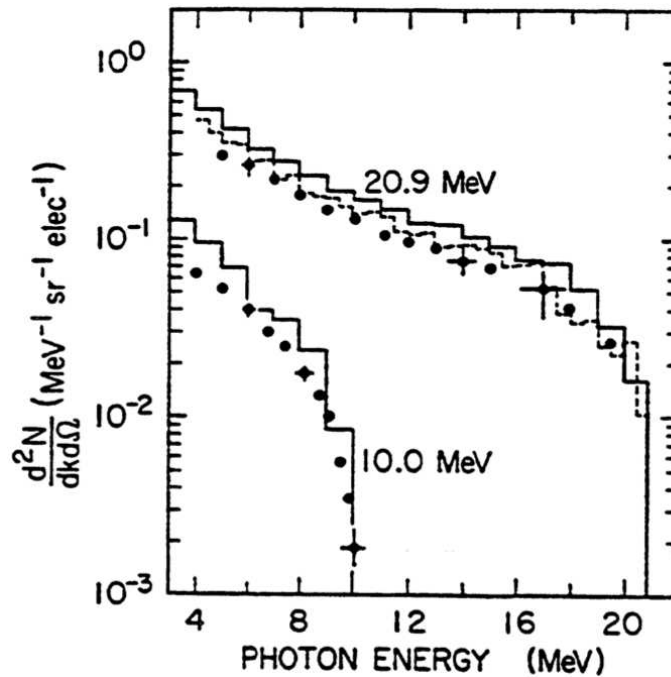


Figure 51: Comparison of EGS (solid histogram) and ETRAN (dashed histogram) calculations of bremsstrahlung spectra with the experimental data (filled circles) of O'Dell et al. (1968), for electrons incident on a composite target of tungsten (0.490 g cm^{-2}) followed by gold (0.245 g cm^{-2}), for a small detector near 0° . [From Ford and Nelson (1978).]

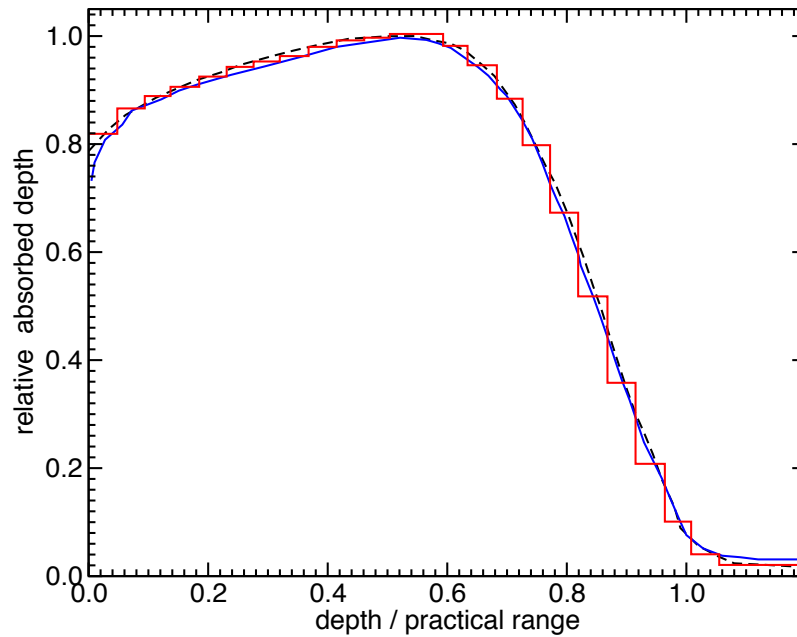


Figure 52: Central-axis relative absorbed dose distributions calculated by Andreo and Brahme (1984) (solid histogram) for a broad parallel beam of 20-MeV electrons on water compared to the experimental results of Harder and Schulz (1972) for 21.2-MeV electrons on PMMA (solid curve) and those of Brahme and Svensson (1979) for 22.5-MeV electrons on water (dashed line). The depth scale is given relative to R_p to facilitate comparison among the different energies. [Based on data from Andreo and Brahme (1984).]

Brahme (1984) have compared the Monte Carlo calculations of Andreo (1980) with the experimental data of Harder and Schulz (1972) and Brahme and Svensson (1979). As depicted in Fig. 52, the calculation with the code of Andreo fits the data excellently.

A careful study of electron depth-dose curves in water has been carried out by Shortt et al. (1986), who measured and calculated the perturbation caused by the placement of several “standard” heterogeneities in water. The heterogeneities studied were an air cylinder (1 cm in diameter, 2 cm in length) and an aluminum cylinder (1 cm in diameter, 1 cm in length) placed on the central axis at 2-mm or 2-cm depth and irradiated by 10- and 20-MeV electron beams. Representative results are shown in Figs. 53 and 54. The only normalization performed was for the homogeneous central-axis data in the peak region, and all other measurements are relative to this. These and other comparisons by Shortt et al. demonstrate that the EGS code can predict accurately the significant effects of these

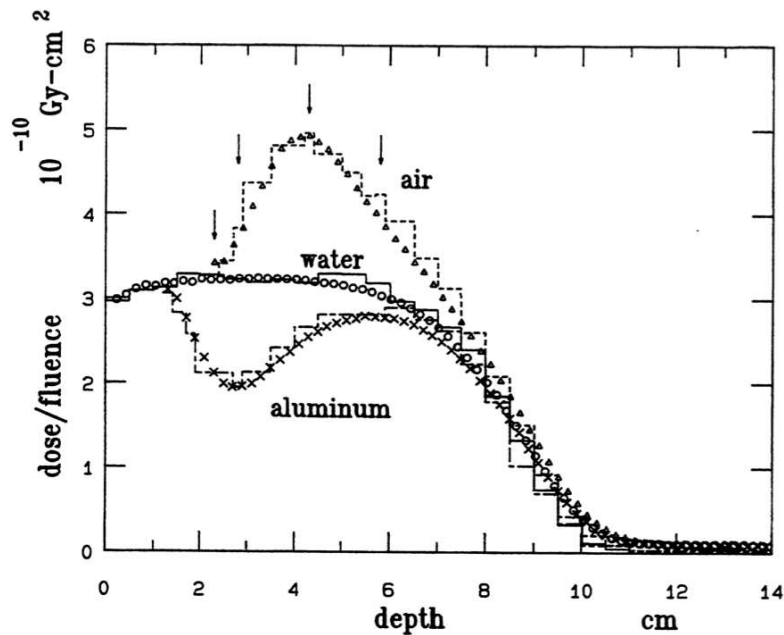


Figure 53: Depth-dose distributions obtained with 20-MeV electrons incident on water with the “standard” air and aluminum heterogeneities starting at a depth of 2 mm. The symbols represent the measured data as follows: \circ , homogeneous water phantom; \times , 1-cm-long aluminum cylinder; Δ , 2-cm-long air cylinder. The histograms are the results of EGS4 Monte Carlo calculations for a monoenergetic point source of 20-MeV electrons. The arrows show the depths at which radial profiles are presented in the next figure. The vertical axis shows absorbed dose to water per unit incident fluence of 20-MeV electrons. The experimental data are all normalized to one point on the curve for water. The measurements have a precision of about $\pm 1\%$ while the statistical accuracy of the Monte Carlo results is about $\pm 2\%$ [From Shortt et al. (1986).]

heterogeneities. However, there were some discrepancies in the depth-dose curves in a homogeneous medium, especially at 10 MeV. We find that by doing a full simulation which accounts for scattering in the titanium exit window of the accelerator, the lead scattering foil, and the air, the calculated and measured data agree within 3% of the maximum dose over the entire curve (see Fig. 55).

This example demonstrates how sensitive comparisons between theory and experiment are to the details of the experiment. With this in mind, Figs. 56-59 compare experimental depth-dose curves in a variety of materials to those calculated using EGS4 with PRESTA and using

CYLTRAN (ITS.V1). The experimental data from Lockwood et al. (1980) are absolute, whereas the experimental data taken from the compilation presented in Berger and Seltzer (1973) appear to have been arbitrarily normalized (and we have kept that normalization). There are several interesting features in these comparisons. Perhaps the most important concern is that the experimental data are scattered as much as the discrepancies between the codes and hence no strong preferences can be drawn. Both codes reproduce the data well. Figure 56, for 1-MeV electrons on beryllium, appears to exhibit the differences between EGS and ETRAN which have been ascribed to the error in ETRAN's energy-loss straggling distribution (see Section II,G,1). The fact that the EGS and ETRAN results are in closer agreement for 1-MeV electrons on copper or 10-MeV electrons on lead (Figs. 57 and 59) is at first sight somewhat surprising because the error in the energy-loss straggling algorithm also affects these materials (although the size of effect is a complicated function of energy, atomic number Z , and step size). However, Fig. 40 indicated that the multiple scattering formalisms cause differences in lead

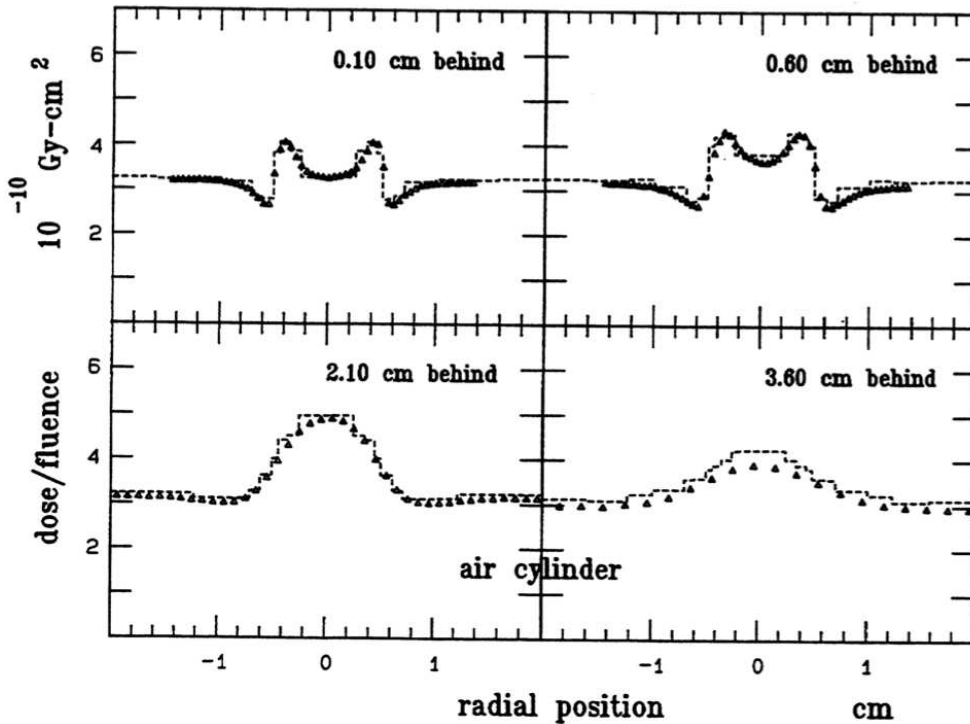


Figure 54: Radial dose profiles for 20-MeV electron beams incident on water with an air cylinder (2cm long, 1 cm diameter) starting at a depth of 2 mm. The symbols represent the measured data and the histograms are the Monte Carlo results. [From Shortt et al. (1986).]

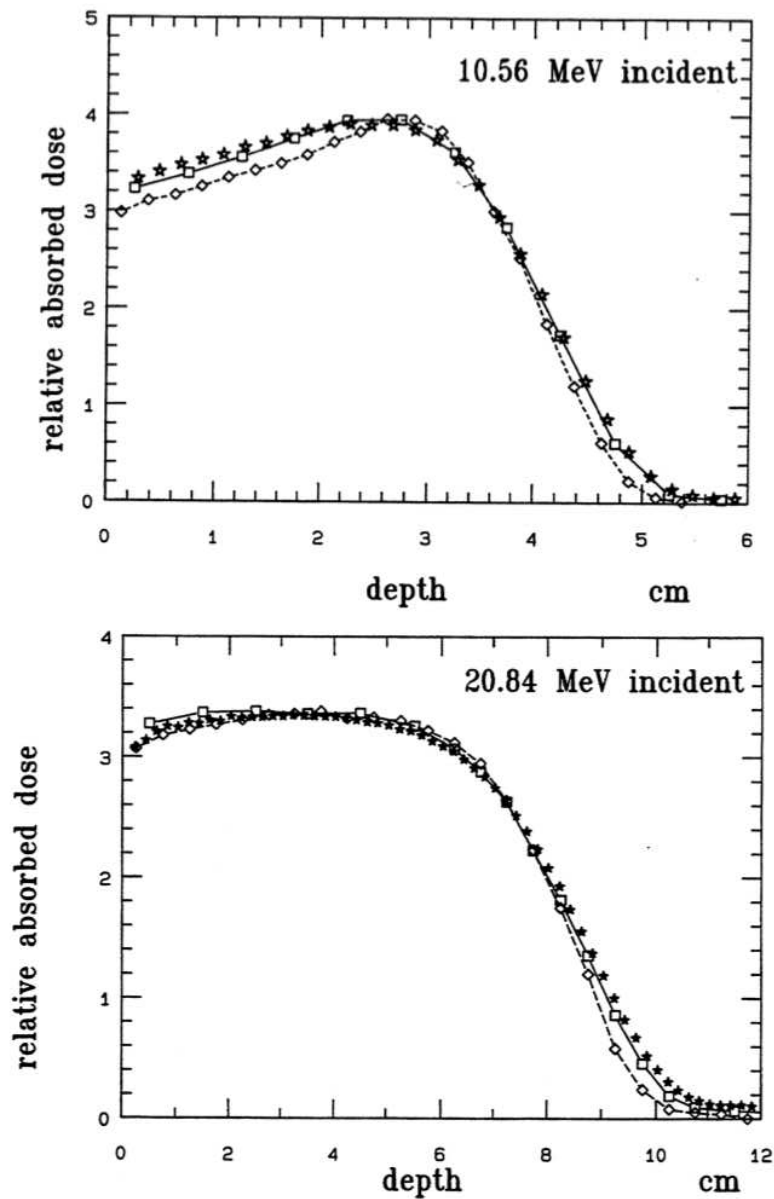


Figure 55: Comparison of central-axis depth-dose curves in water as measured (stars) by Shortt et al(1986) and as calculated using EGS4 with PRESTA. The calculations showed by the diamonds were done for monoenergetic point sources with energies equal to the mean energy of the experimental beam at the phantom surface (10 and 20 MeV). The calculations shown by the boxes start with accelerator beams with energies of 10.56 and 20.84 MeV and explicitly model the influence of the titanium exit window, the lead scattering foil, and the air.

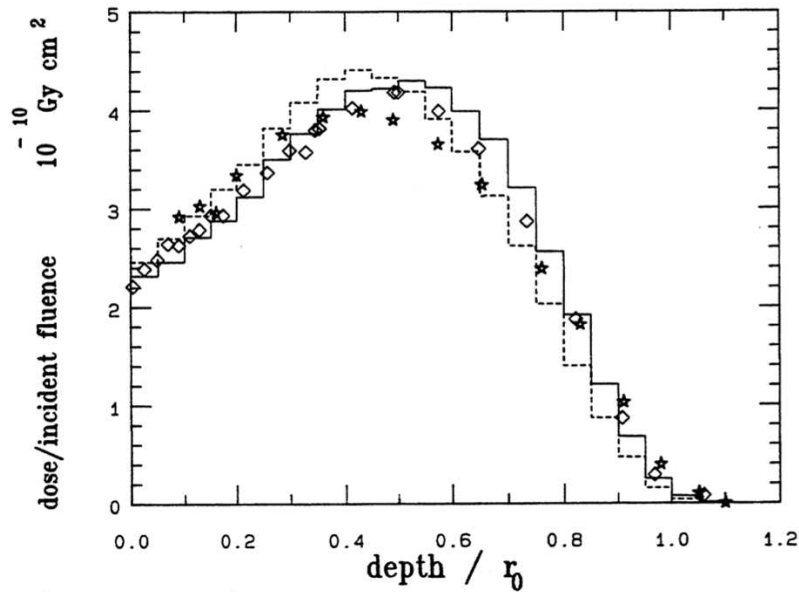


Figure 56: Broad parallel beam of 1-MeV electrons incident normally on beryllium. The solid histogram is calculated using CYLTRAN(ITS Version 1). The dashed histogram is calculated using EGS4 with PRESTA. The absolute experimental data of Lockwood et al. (1980) are shown as open diamonds and other experimental data, taken from a compilation by Berger and Seltzer (1973), are shown as stars.

which are exactly opposite to the energy-loss straggling differences and hence the two effects appear to cancel. In the higher- Z materials, energy-loss straggling due to the creation of knock-on electrons may play a smaller role because of the increased radiative energy loss and multiple scattering. The transport of low-energy electrons in high- Z materials represents the most difficult case to simulate, and it is not too surprising that significant differences are seen in Fig. 58 for 1-MeV electrons on uranium. These unexplained differences deserve further study.

III.C.6. Ion Chamber Response to ^{60}Co γ -Rays

The response of an ion chamber in a ^{60}Co γ -ray field is well understood and forms the basis of primary exposure standards for ^{60}Co (see, for

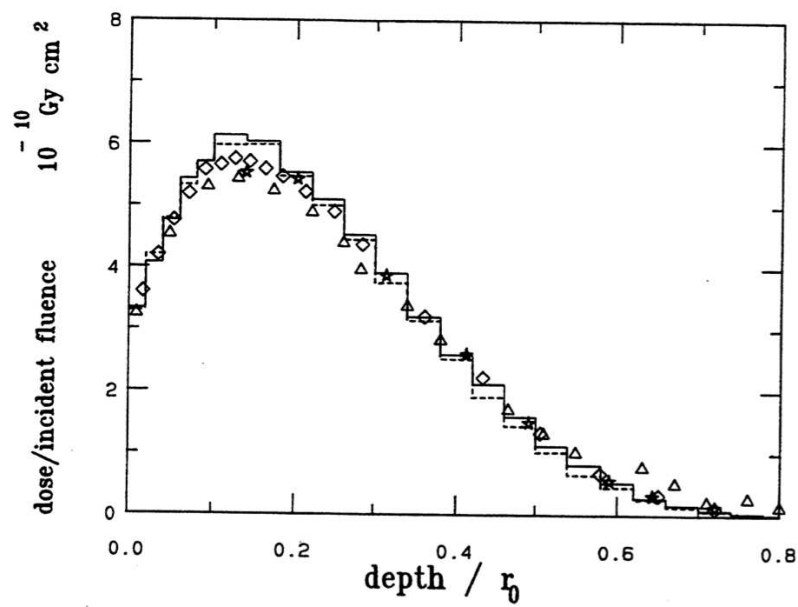


Figure 57: Same as in previous figure except for 1-MeV electrons incident on copper. The open triangles are additional data taken from Berger and Seltzer (1973).

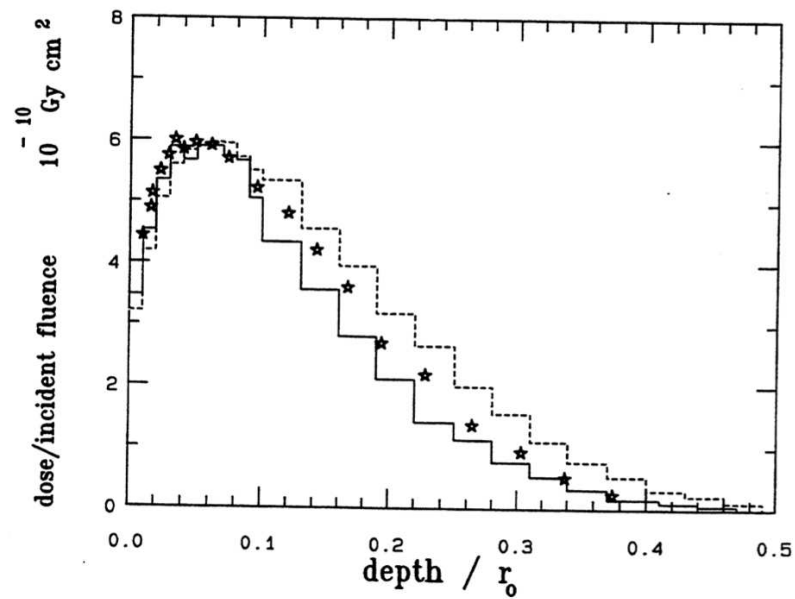


Figure 58: Same as previous figure but for 1-MeV electrons incident on uranium.

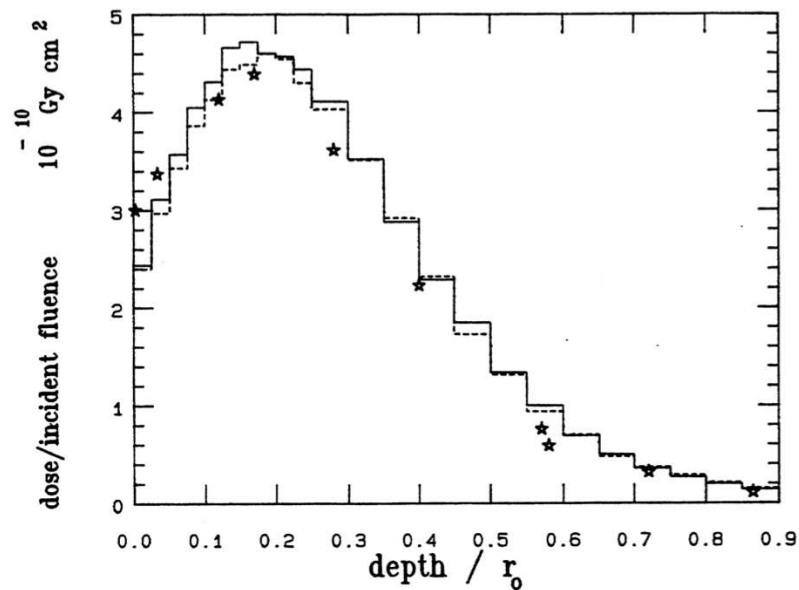


Figure 59: Same as the previous figure but for 10-MeV electrons incident on lead.

example, Attix, 1986). The response per unit photon fluence, after a usually small correction for attenuation and scatter in the chamber walls, is independent of the geometric shape of the detector, and its absolute value is given by cavity theory (Bielajew, 1986a). Calculation of the response of an ion chamber provides a very stringent test of the accuracy of a Monte Carlo code. As shown above in the discussion of step size effects (see Fig. 27) and in several detailed papers (Bielajew et al., 1985; Rogers et al., 1985a), EGS is capable of predicting the response of a carbon-walled ion chamber in a ^{60}Co γ -ray beam to within a 1% statistical uncertainty. We have found that this calculation is a very sensitive test of the electron transport algorithm in the EGS code.

However, the interpretation is more complex. One can get accurate results by deliberately simplifying the transport model, i.e., by making the simulation less realistic. Inaccuracies of one type can often be compensated for by errors of another sort. In Fig. 27 the importance of including lateral displacements during the course of a large electron step was demonstrated, and Fig. 24 shows that corrections for path length curvature are essential for accurate electron simulation if large steps are being used.

Yet, as shown in Fig. 60, ignoring both these factors (stars) recovers the

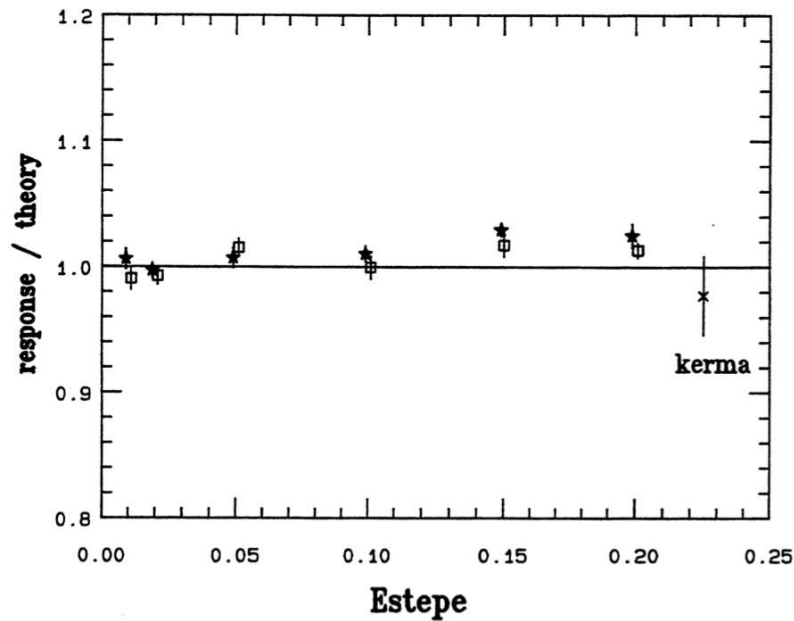


Figure 60: Ion chamber response normalized to the response predicted by cavity theory plotted against ESTEPE, the maximum fractional electron energy loss per electron step used in the calculation. The response is for a pancake ion chamber with minimal full buildup walls of graphite subject to ^{60}Co photons incident perpendicularly on the fiat face. The cavity was 1 cm in radius and 2 mm in depth. The stars are results of calculations that neglect path length curvature corrections. The open boxes neglect multiple scattering as well. The “kerma” calculation neglects all electron transport.

correct calculated ion chamber response and gives a step size-independent result (to within 2% despite errors of up to 30% in each step! One may conclude that under electron equilibrium conditions the calculated results may be very insensitive to certain details of the electron transport.

To emphasize this point further, we have included a calculation in Fig. 60 (boxes) in which multiple scattering is not modeled. The electrons merely travel in straight lines, depositing energy along their original direction of motion after the interaction which set them in motion. Again, the correct result is obtained with no evidence of a significant step size artifact. Indeed, for this particular example, one does not need to do any electron transport to calculate the correct result. This is shown by the point labeled “kerma” in Fig. 60. In this calculation, all the electron energy is deposited at the point where the electron is created.

To summarize, the prediction of ion chamber response is an important benchmark calculation for any Monte Carlo code to be used for radiation dosimetry. The situation of charged-particle quasi-equilibrium in the vicinity of a small air cavity embedded in a solid medium poses a severe challenge to general-purpose Monte Carlo codes. We have seen in Section II,C that this problem is prone to step size artifacts that can be reduced by including path length curvature and lateral displacement in the electron transport modeling or by reducing electron step size. Special-purpose codes can be constructed that are able to calculate efficiently a correct response in certain special cases. Incomplete electron transport methods can still yield correct results. Therefore, it is advisable to use this as only one benchmark of a Monte Carlo code, with other benchmarks to test the code in extreme non-equilibrium cases.

III.C.7. Dose at an Interface

It is essential that a Monte Carlo code for radiation dosimetry applications be able to calculate dose in the vicinity of an interface between two media. The ion chamber, discussed in Section III,C,6, is a special case of an interface subject to an electron fluence in quasi-equilibrium. In radiotherapy applications, knowledge of dose deposition near bone-tissue, tissue-lung, and metal-tissue interfaces is critical to accurate treatment planning. Measurements near interfaces between high- Z and low- Z materials provide an excellent test of Monte Carlo codes and extensive calculational and experimental studies of interface dose deposition have been carried out.

Eisen et al. (1972) measured dose deposition near interfaces with a dye film dosimeter. They compared their results with calculations made using the ZEBRA code (Buxton, 1971) or ETRAN (Berger et al., 1971). However, here we present new results calculated with CYLTRAN (ITS, version 1) and EGS4 with the PRESTA electron transport algorithm (Bielajew and Rogers, 1986a, 1987). A typical example, the dose to aluminum and to gold at each side of an interface irradiated by normally incident 2MeV electrons, is shown in Fig. 61. Given the scatter of the experimental data, both calculated results match the experiment acceptably well. The EGS calculation exhibits less backscatter from the gold. Another comparison, of the dose to a Cu foil with a polystyrene backing, is presented in Fig. 62. CYLTRAN and EGS4 (PRESTA) yield similar results and both exceed the experimental data in the polystyrene. This discrepancy has not been explained.

Another extensive study has been carried out by Lockwood et al. (1980), who used a calorimetric technique to measure, per unit incident

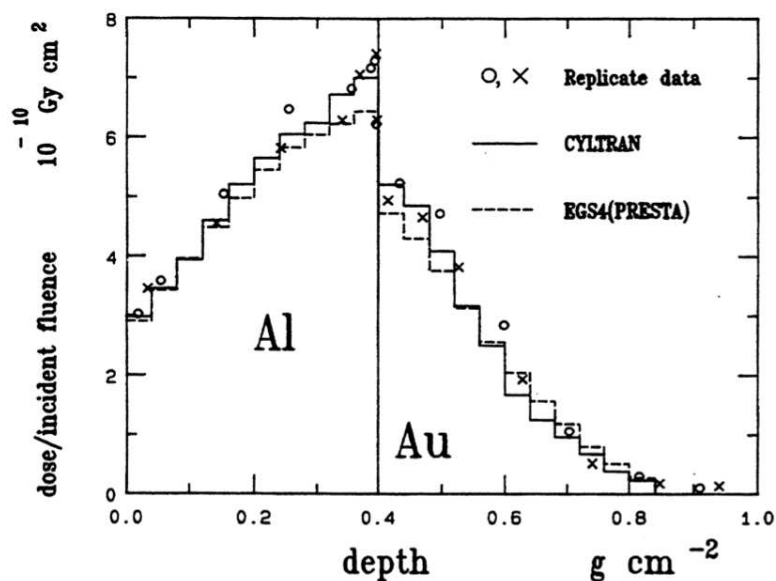


Figure 61: Comparison of Monte Carlo calculated and replicate measured doses in aluminum followed by gold irradiated by a broad beam of normally incident 2.0-MeV electrons. The measurements were performed using a dye-film dosimeter (Eisen et al., 1972).

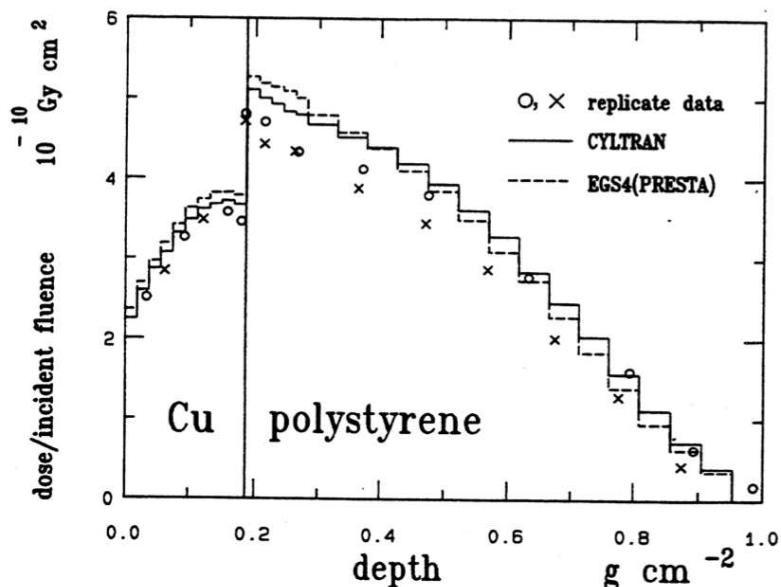


Figure 62: Comparison of Monte Carlo calculated and replicate measured doses in copper followed by polystyrene irradiated by a broad beam of normally incident 2.0-MeV electrons. The measurements were performed using a dye-film dosimeter (Eisen et al., 1972).

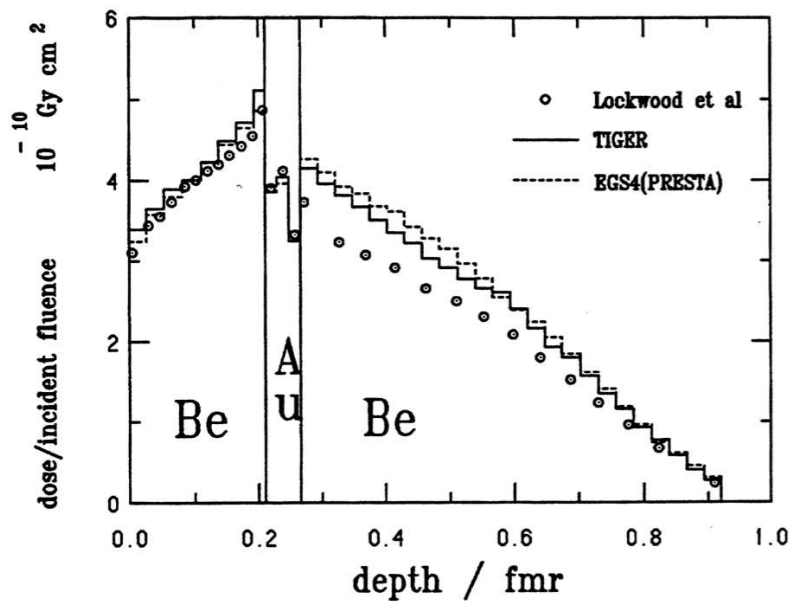


Figure 63: Comparison of Monte Carlo calculated and measured absolute doses per unit incident fluence in beryllium-gold-beryllium irradiated by a broad beam of normally incident 1.0 MeV electrons (Lockwood et al, 1980). The measurements were performed using a calorimetric technique. Depth scale is given as a fraction of the mean range for 1 MeV electrons in each material.

fluence, the absolute dose deposition across interfaces of various compositions. They compared their experimental results with calculations using the ETRAN-based code TIGER (Halbleib and Vandevender, 1975). In general, they obtained good agreement between the measurements and calculations. Figure 63 shows the doses for beryllium-gold-beryllium interfaces. In this case there appear to be significant discrepancies between the calculated and measured doses in the downstream beryllium slab, reminiscent of the discrepancy for the Cu-polystyrene interface in Fig. 62. However, both codes accurately predict the large fraction of the dose in the upstream beryllium slab which is from electrons backscattered from the gold. Both codes also accurately predict the significant decrease in the dose at the back of the gold slab because of the lack of backscatter from the beryllium.

Another benchmark for Monte Carlo calculations is a comparison of dose profiles in thermoluminescent dosimetry (TLD) material, sandwiched

between lead plates and exposed to ^{60}Co γ rays. The experiments were reported by Ogunleye et al. (1980) and the results are shown in Fig. 64. The EGS4 calculations were done with the PRESTA algorithm. In the experiment and calculations, an LiF detector 0.266 cm thick was placed between full buildup walls of Pb (0.0441 cm was used in the calculations). The standard EGS4 (PRESTA) results were obtained using monoenergetic 1.25-MeV photons. They fit the data excellently except near the back wall, possibly due to an underestimate by EGS of the backscatter from the Pb walls. A more accurate calculation, with the photoelectron angular distribution sampled correctly, demonstrates little improvement. An analogous calculation using CYLTRAN gave similar results (not shown), except the agreement was slightly worse on the front face but slightly improved at the back face. A calculation utilizing a realistic ^{60}Co photon spectrum shows some improvement. This agrees with the work of

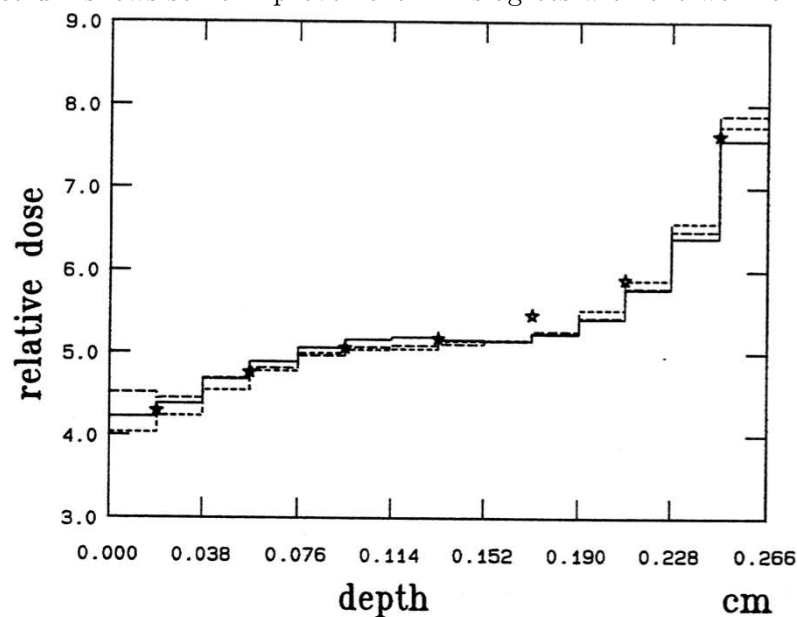


Figure 64: Comparison of measured LiF response to ^{60}Co γ rays (stars) (Ogunleye et al., 1980) with various EGS (PRESTA) calculations: (solid) EGS4 (PRESTA); (short dash) including more accurate photoelectron angular distributions, (long dash) full ^{60}Co spectrum (from Bielajew and Rogers, 1986c,d). The experimental data are arbitrarily normalized in the middle. Ideally, the experimental results would be the average of the adjacent calculated results.

Garth et al. (1980), who showed that scattered photons can play a significant role in interface energy deposition.

III.C.8. Stopping-Power Ratios

Perhaps the most important role of Monte Carlo techniques in radiation dosimetry is the calculation of stopping-power ratios. These are needed in cavity theory to convert charge measurements from radiation detectors, such as ion chambers, into estimates of the absorbed dose in the medium (see, e.g., ICRU, 1984a; Nahum, 1978; Andreo and Brahme, 1986). Determination of Spencer-Attix stopping-power ratios entails calculating the electron fluence spectrum at the point of interest in a phantom and then calculating the ratio of stopping powers in two media, averaged over the electron spectrum (see ICRU 35 for a discussion of the details). The calculation is very sensitive, varying by up to 2% to the choice of stopping powers used for the spectrum averages. Its only somewhat sensitive to the details of the Monte Carlo calculation of the electron spectrum. For example, Nahum (1978) showed that the stopping-power ratio for 20-MeV or lower-energy electron beams was wrong by at most 3% if calculated for the mean energy of the beam at depth, as given by a simple formula. Thus, any comparison with experimental data is not a very sensitive test of the Monte Carlo calculated electron fluence spectra. Furthermore, the experimental data are hard to obtain. Figure 65 presents a comparison of graphite-to-air stopping-power ratios, as measured by Domen and Lamperti (1976) using a graphite calorimeter and graphite ionization chamber and as calculated by Berger for ICRU 35 using $\Delta = 10$ keV, $\rho = 2.25$ g cm⁻³, and the Sternheimer and Peierls (1971) prescription for the density effect. Except at very large depths, agreement between theory and experiment is always better than 1 % and on average much better than this. However, both experimental problems and calculational uncertainties imply that such close agreement may be fortuitous. For example, no account was taken of gap effects in the calorimeter, reported as $\pm 0.7\%$ in ICRU (1984a), and the best value of $(W/e)_{\text{air}}$ has changed by 0.4%.⁷ Similarly, best estimates of the density effect in carbon have changed (ICRU, 1984b) and the choice of carbon density to use in calculating the density effect is an open question which causes an uncertainty of up to 1 %. Comparisons of measured water-to-air stopping power ratios are even more fraught with uncertainties (see ICRU, 1984a). In short, experimental verification of calculated stopping-power ratios is not sensitive to the quality of the Monte Carlo calculations.

⁷2011 work suggests even greater changes are needed in $(W/e)_{\text{air}}$: Thomson and Rogers, PMB 55(2010)3577

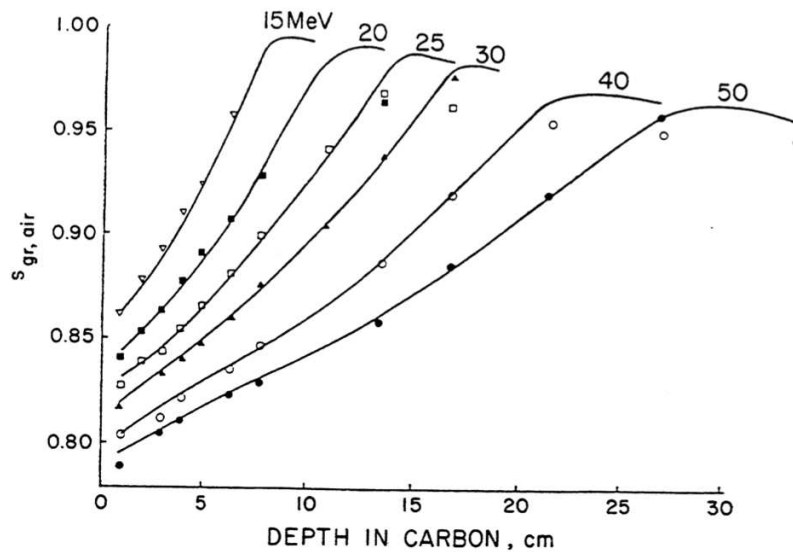


Figure 65: Comparison of experimental (symbols) and calculated (curves) graphite-to-air stopping-power ratios as a function of depth in a graphite phantom for incident electron beams of different energy. The experimental results are by Domen and Lamperti(1976) and calculations are those reported by ICRU 35 (1984a) as by Berger. [From Nahum (1983).]

IV. Variance Reduction Techniques

IV.A. INTRODUCTION

In this section we briefly survey some of the techniques available to improve the efficiency of Monte Carlo calculations. Realistic calculations can take hundreds of hours of CPU time; hence improved calculating efficiency is desirable.

In electron-photon Monte Carlo transport, most of the CPU time is spent generating random numbers, rotating coordinate frames, sampling the multiple-scattering angle, and tracing through the geometry. Efficient coding and structure in a Monte Carlo code can save a large amount of computing time. For example, a subroutine call requires considerable overhead, and for short procedures, such as generating random numbers, one can speed up a Monte Carlo code considerably by computing the random numbers in line (see Section II,E). Similarly, one can speed up calculations by doing table lookups on frequently used functions (e.g., EGS does table lookups for all sines and cosines) and one can improve the

efficiency of sampling procedures for physical processes. In contrast, variance reduction techniques can improve the efficiency by giving more emphasis to the physical quantities of interest, thus producing more relevant information for a given amount of CPU time. These techniques are the subject of this section.

Consider a shielding problem in which, on average, only one photon in a thousand gets through the shield. One could change the cross section so that for every 1000 histories, 10 photons would get through the shield. This would improve the efficiency, since the fractional uncertainty in the number of photons getting through the shield would be reduced from $\pm 100\%$ ($1 \pm \sqrt{1}$) to $\pm 32\%$ ($10 \pm \sqrt{10}$). To make the technique work, one must also have a procedure which tells exactly how the change in cross section has changed the overall probability of the event so that a “fair game” is maintained. In this case, one would have to know that the changes of the cross section increased the probability of transmission by 10, and hence the answer becomes 1.0 ± 0.3 . In the general case, a fair game is maintained by associating a weight with each particle which corresponds to the relative probability that the history being followed would actually occur. In an analog calculation, where no variance reduction techniques are used, the weight is always 1.0, whereas in the shielding example it would be 0.10. In the scoring routines, the particle weight, i.e., the relative probability of this event, is scored rather than the actual number of particles.

There are various straightforward “biasing techniques” which can dramatically improve computing efficiency. Considerable effort has gone into developing a rigorous foundation for these and other variance reduction techniques, such as using statistical estimators, especially as applied to neutron and photon transport problems. In what follows we present a brief sketch of some techniques which can be used effectively in electron-photon simulations. Various reports and books contain more extensive and rigorous treatments (see, in particular, McGrath and Irving, 1975, and the annotated bibliography therein; also Hammersley and Handscomb, 1964; Alm Carlsson, 1981; Lund, 1981; Stevens, 1980; Kahn, 1956). One particularly exciting possibility which has not yet been extensively exploited is the development of adjoint Monte Carlo transport methods for electrons as reported by Jordan (1986).

IV.B. **EXPONENTIAL TRANSFORMATION OF PHOTON PATH LENGTH AND FORCED INTERACTIONS**

Although these techniques apply only to the photon component of an electron-photon simulation, we have found them very useful, even for problems involving electron transport.

When calculating photon depth-dose curves, one is frequently interested in detailed information in the buildup region. The exponential transformation of photon path lengths can be used to bias the sampling procedure to give more photon interactions in this region and thus improve the efficiency for dose calculation there, while potentially making it worse deeper in the phantom where relatively fewer photons now interact. To implement this method, define η to be the number of mean free paths to the next photon interaction. Then let

$$\eta = -B \ln R_i \quad (13)$$

with

$$B = 1/(1 - C \cos \theta) \quad (14)$$

where C is a user-defined variable, R_i a random number uniformly distributed between 0 and 1, and θ the angle of the photon with respect to the direction of interest (the depth axis for a depth-dose curve). Recall that in the analog calculation $\eta = \ln R_i$ (see Section II,A,4), which is recovered for $C = 0$. For values of $C < 0$, B is < 1 for forward-going photons and hence the point of the first interaction is closer to the surface. For $0 < C < 1$ the path length is stretched in the forward direction, which is useful in shielding problems. This equation for B is derived, based on the underlying theory, so that a fair game is maintained by adjusting the weight W to become W' , given by

$$W' = W B e^{-\eta C \cos \theta} \quad (15)$$

Note that the new weight W' depends on η , the number of mean free paths actually selected. In the $C < 0$ case, the weight decreases in regions where the number of photon interactions has increased ($\eta < -\ln(1 - C)/C$ for $\cos \theta = 1$) and increases elsewhere. When applying this technique, the energy deposited is scored as the physical energy deposited times the weight of the particle. Table II compares the relative efficiency for calculating the dose in different depth bins for a 7-MeV photon beam incident on a water slab. As $-C$ increases, the efficiency for calculating the dose near the surface improves by a factor of 3 compared with the unbiased case, despite the fact that the computing time per history goes up by a factor of 2. Note that the efficiency for calculating the dose at depth gets worse at large values of $-C$ because fewer photons get to those depths (although for $C = -1$, the efficiency improves because this causes more photons to interact in the phantom, $\sigma_{\text{tot}}^{-1} = 39$ cm). The optimal choice of

Table 2:
Relative efficiency versus the parameter C of exponential transformation biasing for calculation of the dose at various depths in water irradiated by 7-MeV photons^a

C	Relative efficiency of calculated dose			Histories
	0-0.25 cm	6-7 cm	10-30 cm	10 ³
0	(1)	(1)	(1)	100
-1	1	1	4	70
-3	1.4	1.2	0.6	55
-6	2.7	2.8	0.07	50

^a Biasing was applied on only the first photon interaction. The relative efficiency is given by the inverse of the square of the uncertainty in doses for a series of calculations which all took the same CPU time T (see Section III.B,3).

parameter is very problem dependent. We have used $C = -6$ for studying dose buildup curves (Rogers and Bielajew, 1985). In general, one should prevent particles from having too large a weight, since otherwise these rare cases can occasionally lead to an increase in the variance.

A second, very useful, technique is to force photons to interact within the geometry of interest. In this case, select the number of mean free paths to the next interaction using:

$$\eta = -\ln[1 - R_i(1 - e^{-X})] \quad (16)$$

where X is the maximum number of mean free paths the photon can travel in its current direction within the geometry. This samples η in the range 0 to X rather than 0 to ∞ as in the analog calculation. However, the distribution of interactions does not change and the weight is reduced by a constant given by the probability that the particle would interact:

$$W' = W(1 - e^{-X}) \quad (17)$$

This technique is very easy to implement as long as one can determine X, which in general can be difficult. The structure of EGS permits a procedure for finding X in any geometry (see Rogers and Bielajew, 1984; the relevant coding is on the EGS4 distribution tape).

The improvements obtained using this technique are very problem dependent. Its use is essential when almost all photons would pass through the geometry of interest without interacting. For example, in calculating the dose on the surface of a phantom from electrons generated by ⁶⁰Co γ -ray interactions in 100 cm of air, one improves the efficiency by a factor of 7

by forcing the photons to interact in the air. Similarly, the efficiency in calculating the ion chamber response to ^{60}Co γ rays improves by 60% when interactions are forced to occur and by much more than that when calculating the contribution to the response from photons interacting twice in the chamber (Bielajew et al., 1985).

The above two techniques have been singled out because they are especially useful in a variety of problems which involve electron as well as photon transport. Many other variance reduction techniques have been developed for photon transport (e.g., splitting, Russian roulette, correlated sampling, systematic sampling, and statistical estimation). The reader is referred to the general references given in the previous section and, on the use of statistical estimators in medical physics, to Persliden and Aim Carlsson (1986) or Williamson (1987).

IV.C. ENHANCED CROSS SECTIONS

The calculation of a bremsstrahlung spectrum can be very time-consuming because each slowing electron gives off relatively few photons. The details of the electron trajectory play only a small role in determining the spectrum compared with the more important features, namely the relative number of photons generated at each electron energy and the photon attenuation and scatter in the system. One can reduce the variance of the calculated spectrum by artificially enhancing the number of bremsstrahlung photons produced and reducing their weight by the corresponding factor. This is a standard option of the ETRAN-based codes (Berger and Seltzer, 1973). ETRAN has a similar option to enhance the production of characteristic x rays. It is relatively simple to implement such procedures in ETRAN because steps are not interrupted by the production of secondaries. By disregarding the energy loss of the electron due to the extra bremsstrahlung events, its history remains properly described.

IV.D. RANGE REJECTION OF ELECTRONS

We have discussed several standard variance reduction techniques which modify the transport simulation and maintain a fair game by altering a particle's weight. We now turn to a variety of techniques which are less sophisticated but useful.

Range rejection of electrons means that one ceases to track an electron once its residual range is smaller than the distance to the nearest boundary

or to the region of interest in the problem. This technique can save a great deal of CPU time in energy deposition problems involving relatively large regions. However, it introduces one approximation by ignoring the possibility that the electron produces a photon which could then escape from the current region. For this reason, it is usual to introduce a high-energy limit for its application.

When calculating the response of an ion chamber in a ^{60}Co γ -ray beam, this technique improves the calculational efficiency by a factor of 4 because a large fraction of the electrons generated in the walls of the chamber are unable to reach the gas cavity and hence nothing would be gained by taking the time to simulate their tracks (Bielajew et al., 1985).

IV.E. USE OF PRECOMPUTED RESULTS

A general rule in Monte Carlo simulations is always to use as much prior information as possible. One approach is to use precomputed results to speed up part of the calculation. We have used this idea in two different ways.

One example comes from a study of the effects of scatter in a ^{60}Co therapy unit (Rogers et al., 1985b, 1988). To simulate the radiation transport within the ^{60}Co capsule took roughly 24 h of VAX CPU time. Rather than repeating these 24 h in each of the hundreds of runs we did in the study, we stored the phase space parameters of roughly 2 million particles as they left the capsule and entered the beam collimator system. Different random number sequences were used each time this data file was accessed, to reduce correlation of results.

Another aspect of the same project was to calculate the dose, as a function of depth, due to contaminant electrons from the ^{60}Co unit and the intervening air. Rather than track the particles in a tissue phantom and score the dose, the particle spectra were stored at the phantom surface. When adequate spectra $\phi(E)$ were obtained, the dose D , as a function of depth d , was calculated using previously calculated fluence-to-dose conversion factors, $K_E(d)$ from Rogers (1984b) and Rogers and Bielajew (1985), i.e.,

$$D(d) = \int_0^{E_{\max}} \phi(E) K_E(d) dE \quad (18)$$

This technique gains well over an order of magnitude in computing efficiency because each K_E array represents a long calculation. However, two approximations are introduced because the K_E values are for broad

beams with normal incidence. For situations in which the real beams are "broad," the first approximation can be quite accurate, although for narrow photon beams it can cause 10-50% overestimates of the peak dose, and for narrow electron beams it can be totally wrong. The approximation of normal incidence can be poor for low-energy electrons (\leq a few hundred keV) but is often quite accurate for higher-energy electrons if the geometry is appropriate.

V. Computing Requirements

V.A. INTRODUCTION

Monte Carlo transport calculations can use large amounts of CPU time. The steady decrease in the costs of computing time is one of the major reasons for the current surge of interest in this technique. We finish this review by giving some idea of typical computing times required. Most of our timings will be given for calculations done in single precision on a VAX 11/780 with a floating-point accelerator. Although this machine originally cost over \$500,000, roughly equivalent computing power is available today (1988) on a personal computer which costs about \$10,000.

As a rule of thumb, energy deposition problems take an order of magnitude longer for photon beams than for electron beams. This is because the electron beam problems frequently involve much smaller volumes with a much higher density of particle histories of a similar nature, thus reducing the variations from one history to another.

The calculation of depth-dose curves for broad parallel beams of electrons and photons illustrates this rule of thumb. For uncertainties of $\pm 1\%$ (one standard deviation) at the peak of the depth-dose curves, EGS required between 600 and 2600 s of VAX11/780 CPU time for incident electrons with energies between 1 and 10 MeV and 10,000-40,000 s for photons of the same energies. The timings are highly dependent on the exact values of various transport parameters, but these were chosen to be as fast as possible while giving the necessary accuracy (see Rogers, 1984b).

As another example, the calculation of A_{wall} the wall attenuation and scatter correction factors for ion chambers in ^{60}Co γ -ray beams takes 3-5 h of CPU time using EGS to get an uncertainty of $\pm 0.2\%$ whereas it can take over 100 h of CPU time to get $\pm 1\%$ uncertainty on the calculated γ -ray response of the same chamber (Bielajew et al., 1985). This is because, in general, it is faster to calculate a ratio such as A_{wall} and because, as a ratio, it does not require as accurate electron transport and hence larger step sizes can be used.

A final example concerns the calculation of energy deposition kernels for monoenergetic photons. This project involved determining where the energy is deposited relative to a photon's primary interaction site for use in convolution dose planning (Mackie et al., 1988). The calculations for 23 different photon energies required over 4000 h of VAX11/780 CPU time (not counting the reruns!).

V.B. A TREATMENT-PLANNING EXAMPLE

The one-or two-dimensional nature of the examples described above is typical of many kinds of problems approached using Monte Carlo techniques. To answer the question of whether Monte Carlo calculations can ever be directly useful for radiotherapy treatment planning, we must examine a fully three-dimensional problem. Since the computing time is critically dependent on many variables, as we specify various parameters we will briefly mention the effects of changing them.

The following problem simulates doing a treatment plan for a monoenergetic 20-MeV electron beam incident on a patient. Lower-energy beams would require less time to obtain a given accuracy since the electrons would spread out over a smaller volume .

The beam is assumed to be uniform, parallel, and perpendicularly incident. These parameters of the beam have no effect on the length of time required for the simulation and were introduced only for ease in coding the sample problem. It would take the same amount of time to simulate the dose deposition pattern produced by a completely realistic beam from a therapy machine including effects of scatter from the air, flattening filters, beam collimators, applicators, etc.

The variance on the calculated dose (σ^2 ; see Section III,B,3) is roughly inversely proportional to the fluence of incident particles (i.e., the number per unit area). This fluence is proportional to the total number of histories (and thus computing time) per unit area of the beam. For a given variance of the computed dose, the calculation time is thus proportional to the incident beam area.

The patient is simulated by a 19-cm³ phantom with 1-cm³ voxels everywhere except in the 1-cm² central region, which has sixteen 2.5-mm² voxels that are 1 cm thick except at the peak of the depth-dose curve, where there are four voxels, each 2.5 mm thick. The computing time is dependent on voxel size in a variety of ways. The statistical fluctuations in energy deposition are dependent on the number of particles contributing. Near the surface, where most electrons are going in the direction of the beam, this means that computing efficiency is proportional to the X-Y

area of the voxel (depth defined in the Z direction), whereas at depth, where tracks are more isotropic, the efficiency is more related to the voxel volume. The voxel size also affects electron step sizes, since the more boundaries there are, the more often steps are interrupted and the longer the calculation becomes (Bielajew and Rogers, 1986a, 1987). Voxel size can also affect calculation speed since the storage space required can become so great that arrays must be swapped in and out of core. In the example, the fairly coarse grid has 10,649 voxels, which requires 125,000 words of storage for just the main scoring arrays. A resolution of 2.5 mm everywhere would require over 5×10^6 storage locations. Furthermore, as the voxel size becomes smaller, electrons must be tracked to lower energies so that artifacts are not introduced. For example, the CSDA range of a 500-keV electron in water is about 0.018 kg m^{-2} (1.8 mm at unit density), whereas it is about 0.044 kg m^{-2} for a 1-MeV electron. Thus, for 1-cm^3 voxels a cutoff of $ECUT = 1 \text{ MeV}$ is usually acceptable, whereas for 2.5-mm^3 voxels 500 keV or less is needed. For electron transport simulations in which not many knock-on electrons are created and in which roughly a constant fraction of the energy is lost in each electron step [i.e., $E_i = E_{i-1}(1 - ESTEPE)$], the calculation time varies as

$$T \propto \frac{\ln(E_0/ECUT)}{ESTEPE} \quad (19)$$

Hence, using a value of $ECUT = 1 \text{ MeV}$ instead of 500 keV will reduce computing time by about 20% for a 20-MeV beam.

In the example, every other layer of voxels is assumed to be a different material, and the density of every voxel has been changed from the density in the input data file. This realistically models the use of patient CT data. Since a curved surface can be simulated using air-filled voxels, the fact that the “patient” has a flat surface has no effect on the computing time, except in the sense that smaller voxel sizes might be necessary to simulate a curved surface accurately.

In the sample calculation we used EGS4 and set $ESTEPE = 0.04$ since this should provide reasonably accurate results. However, for details of dose deposition near sharp inhomogeneities, a somewhat smaller $ESTEPE$ would be necessary, especially if smaller voxels were used. This would have a dramatic effect on timing since it is inversely proportional to $ESTEPE$. If the calculation were done using the PRESTA algorithm, we would not expect a dramatic change in computing time for the base case, but for smaller voxels and higher accuracy PRESTA would reduce computing time, compared to the pure EGS4 calculation, by up to a factor of 2 (Bielajew and Rogers, 1986a, 1987).

In the example we use $ECUT = 500$ keV with $AE = 189$ keV to ensure adequate energy-loss straggling. A higher value of AE may be acceptable but would not change the time significantly.

Calculation for 10^5 incident electrons took 5.1 h of VAX11/780 CPU time in the sample problem and produced an uncertainty (1σ) of $\pm 11\%$ at the peak of the depth-dose curve in the 2.5-mm^3 voxels and $+4\%$ in nearby voxels with dimensions of $1\text{ cm}^2 \times 2.5\text{ mm}$. If an accuracy of $\pm 2\%$ of the peak dose is required for treatment-planning purposes, holding $2T$ constant implies that 154 h of CPU time is required for the small-voxel case or 20 h to obtain the same accuracy in the larger voxels. These times would increase by a factor of 4 for an accuracy of $\pm 1\%$.

These values are clearly unacceptable for routine treatment-planning calculations. We have also timed the EGS code on two much faster machines. On an IBM 3090 mainframe (currently the fastest IBM serial machine), the EGS code runs 22 times faster than on the VAX 11/780. Similarly, on an FPS 264 attached processor, the code runs 11 times faster than on the VAX. This reduces the CPU time for the $+2\%$ calculation to 7 h for the IBM 3090 and 14 h for the FPS 264 for the small-voxel problems or 54 min and 2 h, respectively, for the large-voxel case. These figures are beginning to sound feasible for special cases in treatment planning, although much effort is still required to provide realistic input beam parameters.

All these calculations have been for electron beams. The calculations for photon beams generally take 10 times longer, although the requirements for resolution may be less important because perturbations by voids and bones are not nearly as dramatic as they are in the electron beam case.

Future computers should dramatically decrease the computing time and cost. Monte Carlo transport calculations are ideally suited to parallel processing, since each history can be treated independently. Thus, we can expect considerable increase in throughput from these kinds of developments, even if we do not see any dramatic breakthroughs in computing technology such as the use of high- T_c superconductors for ultrafast machines.

VI. Conclusions

We hope that this chapter has demonstrated that Monte Carlo techniques for simulating electron and photon transport have attained considerable sophistication and accuracy. They have been used in a wide variety of radiation dosimetry and other applications and their use can be expected

to increase as the cost of computing continues to decrease and as the software available increases. In view of the large amount of effort invested in the two currently available code systems, it seems advisable that most future effort should be based on these systems. This does not mean that they are perfect; on the contrary, more work is needed to improve them, to explain the various

discrepancies with experiment that we have noted, and to do careful benchmark comparisons for other situations.

Despite our belief that new users should make use of existing software technology, an underlying theme of this chapter has been that users must have a good understanding of what the code is doing so they can ensure that both they and the codes are doing appropriate and accurate simulations. Under those circumstances, Monte Carlo simulation is a powerful and versatile tool for radiation dosimetry.

VII. Appendix A: Computational Models

In this report, NRCC calculations with CYLTRAN (CYLindrical TRANsport) were done with the VAX double-precision version of CYLTRAN, which is part of the Sandia Laboratories ITS (version 1) series (Integrated Tiger Series; Halbleib and Melhorn, 1984). Aside from minor I/O changes, the only substantive change was to switch to the inline random number generator used in EGS4. By avoiding the subroutine call, this change was found to save about 15% on the CPU time. CYLTRAN contains standard options to turn off straggling and knock-on electron production. Documentation is given in Halbleib and Melhorn (1984) and the ETRAN documentation (Berger and Seltzer, 1973) and CYLTRAN documentation (Halbleib and Vandevender, 1976b).

NRCC calculations with EGS were done with EGS4 (or equivalent). See the documentation in Nelson et al. (1985). It is not a standard option in EGS to do CSDA calculations, and these have been done by modifying the data preparation program (PEGS4) to produce unrestricted stopping powers and to set Moller, Bhabha, and bremsstrahlung cross sections to zero. All bremsstrahlung photons were assumed to escape in the CSDA calculations.

VIII. Acknowledgment

The authors are indebted to Heather Matchett for her endless typing and data management efforts in writing this chapter. We would also like to express our sincere thanks to our many colleagues who have helped educate us about Monte Carlo techniques, in particular W. Ralph Nelson of Stanford Linear Accelerator Center, Alan E. Nahum of the Royal Marsden Hospital, Stephen M. Seltzer and Martin J. Berger of the National Bureau of Standards, John Halbleib of Sandia Laboratories, and Pedro Andreo of the Karolinska Institute.

IX. References

- The literature survey for this review was completed in June, 1987.
- Ahrens, J., Borchert, H., Czock, K. H., and Gimm, H. (1975). Total nuclear photon absorption cross sections for some light elements. *Nucl. Phys. A* A2S1, 479-492.
- Alm Carlsson, G. (1981). "Effective Use of Monte Carlo Methods," Rep. ULiRAD-R-049. Department of Radiology, Linkoping University, Linkoping, Sweden.
- American Association of Physicists in Medicine (AAPM) (1983). A protocol for the determination of absorbed dose from high-energy photon and electron beams. *Med Phys.* 10, 741-771.
- Anderson, D. W. (1984). "Absorption of Ionizing Radiation." University Park Press, Baltimore, Maryland.
- Andreo, P. (1980). Monte Carlo simulation of electron transport in water; absorbed dose and fluence distributions. English translation of a portion of a Ph.D. Thesis, University of Zaragoza, Zaragoza, Spain.
- Andreo, P., and Brahme, A. C. (1981). Mean energy in electron beams. *Med. Phys.* 8,682-687.
- Andreo, P., and Brahme, A. (1984). Restricted energy-loss straggling and multiple scattering of electrons in mixed Monte Carlo procedures. *Radiat. Res.* 100, 16-29.
- Andreo, P., and Brahme, A. (1986). Stopping power data for high-energy photon beams. *Phys. Med. Biol.* 31, 839-858.
- Attix, F. H. (1986). "Introduction to Radiological Physics and Radiation Dosimetry." Wiley, New York.
- Berger, M. J. (1963). Monte Carlo calculation of the penetration and diffusion of fast charged particles. *Methods Comput. Phys.* 1, 135-215.
- Berger, M. J., and Seltzer, S. M. (1970). Bremsstrahlung and photoneutrons from thick tungsten and tantalum targets. *Phys. Rev. C* 2,621-631.
- Berger, M. J., and Seltzer, S. M. (1972). Response functions for sodium iodide scintillation detectors. *Nucl. Instrum. Methods* 104, 317-332.
- Berger, M. J., and Seltzer, S. M. (1973). "ETRAN, Monte Carlo Code System for Electron and Photon Transport Through Extended Media," Documentation for RSIC Computer Code Package CCC-107. Oak Ridge Natl. Lab., Oak Ridge, Tennessee.
- Berger, M. J., and Seltzer, S. M. (1982a). "Stopping Powers and Ranges of Electrons and Positrons," Rep. NBSIR 82-2550-A; also published as ICRU (1984b). National Bureau of Standards, Washington, D.C.
- Berger, M. J., and Seltzer, S. M. (1982b). "Tables of Energy Deposition in Water Irradiated by Point Monodirectional Electron Beams with Energies from 1 to 60 MeV, and Applications to Broad Beams," Rep. NBSIR 82-2451. National Bureau of Standards, Washington, D.C.

- Berger, M. J., and Wang, R. (1989). Multiple-scattering angular deflections and energy-loss straggling in electron transport calculations. in "Monte Carlo Transport of Electrons and Photons Below 50 MeV? (W. R. Nelson, T. M. Jenkins, A. Rindi, A. E. Nahum, and D. W. O. Rogers, eds.). pp. 21-56. Plenum, New York.
- Berger, M. J., Seltzer, S. M., Chappell, S. E., Humphreys, J. C., and Motz, J. W. (1969). Response of silicon detectors to monoenergetic electrons with energies between 0.15 and 5.0 MeV. Nucl. Instrum. Methods 69, 181-193.
- Berger, M. J., Seltzer, S. M., Chappell, S. E., Humphreys, J. C., and Motz, J. W. (1969b). Tables of Response Functions for Silicon Electron Detectors. NBS Technical Note 489. National Bureau of Standards, Washington, D.C.
- Berger, M. J., Seltzer, S. M., Eisen, H. A., and Silverman, J. (1971). Absorption of electron energy in multi-layer targets. Trans. Am. Nucl. Soc. 14, 887-888.
- Berman, B. L. (1976). "Atlas of Photo neutron Cross Sections Obtained with Monoenergetic Photons," Rep. UCRL-78482. Lawrence Livermore Lab., Livermore, California.
- Bethe, H. A. (1953). Moliere's theory of multiple scattering. Phys. Rev. 89, 1256-1266.
- Bielajew, A. F. (1986a). Ionisation cavity theory: A formal derivation of perturbation factors for thick-walled ion chambers in photon beams. Phys. Med. Biol. 31, 161-170.
- Bielajew, A. F. (1986b). "RNG64-a 64-Bit Random Number Generator for Use on a VAX Computer," Intern. Rep. No. PIRS-0049. National Research Council of Canada, Ottawa.
- Bielajew, A. F., and Rogers, D. W. O. (1986a). "PRESTA-the Parameter Reduced Electron-Step Transport Algorithm for Electron Monte Carlo Transport," Rep. PIRS-0042. National Research Council of Canada, Ottawa.
- Bielajew, A. F., and Rogers, D. W. O. (1986b). Interface artifacts in Monte Carlo calculations. Phys. Med. Biol. 31, 301-302.
- Bielajew, A. F., and Rogers, D. W. O. (1986c). A Comparison of Experiment with Monte Carlo Calculations of TLD Response. Med. Phys. 13, 609 (abstr.).
- Bielajew, A. F., and Rogers, D. W. O. (1986d). "Photoelectron Angle Selection in the EGS4 Code System," Intern. Rep. No. PIRS-0058. National Research Council of Canada, Ottawa.
- Bielajew, A. F., and Rogers, D. W. O. (1987). PRESTA. Nucl. Instrum. Methods Phys. Res. Sect. B 18, 165-181. .
- Bielajew, A. F., Rogers, D. W. O., and Nahum, A. E. (1985). The Monte Carlo simulation of ion chamber response to ^{60}Co -resolution of anomalies associated with interfaces. Phys. Med. Biol. 30, 419-427.
- Blunck, O., and Leisegang, S. (1950). Zum energieverlust schneller Elektronen in dunnen Schichten. Z. Phys. 128, 500-505.
- Brahme, A., and Svensson, H. (1979). Radiation beam characteristics of a 22 MeV microtron. Acta Radiol.: Oncol. 18, 244-272.

- Bruce, W. R., and Johns, H. E. (1960). The spectra of x rays scattered in low atomic number materials. *Br J. Radiol., Suppl.* 9, 1-57.
- Butler, J. (1956). Machine sampling from given probability distributions. In "Symposium on Monte Carlo Methods" (H. A. Meyer, ed.), pp. 249-264. Wiley, New York.
- Buxton, L. (1971). "The Electron Transport Code ZEBRA 1," Rep. TR-1536. Harry Diamond Laboratories.
- Chilton, A. B. (1978). A note on the fluence concept. *Health Phys.* 34, 715-716.
- Chilton, A. B. (1979). Further comments on an alternative definition of fluence. *Health Phys.* 36, 637-638.
- Colbert, H. M. (1974). "SANDYL, a Computer Program for Calculating Combined Photon Electron Transport in Complex Systems," Sandia Rep. SLL-74-0012. Sandia Laboratories, Livermore, California.
- Cormack, D. V., and Johns, H. E. (1954). The measurement of high-energy radiation intensity. *Radiat. Res.* 1, 133-157.
- Cunningham, J. R., Woo, M., Rogers, D. W.O., and Bielajew, A. F. (1986). The dependence of mass energy absorption coefficient ratios on beam size and depth in a phantom. *Med. Phys.* 13,496-502.
- Damkjaer, A. (1982). The response of a silicon surface barrier detector to monoenergetic electrons in the range 100-600 keV. *Nucl. Instrum. Methods* 200, 377-381.
- Debertin, K., and Grosswendt, B. (1982). Efficiency calibration of semiconductor detectors by primary standard sources and Monte Carlo calculations. *Nucl. Instrum. Methods* 203, 343-352.
- Domen, S. R., and Lamperti, P. J. (1976). Comparisons of calorimetric and ionimetric measurements in graphite irradiated with electrons from 15 to 50 MeV. *Med. Phys.* 3, 294-301.
- Ehrman, J. R. (1981). "The Care and Feeding of Random Numbers," SLAC VM Note Book, Module 18. SLAC Computer Services, Menlo Park, California.
- Eisen, H., Rosenstein, M., and Silverman, J. (1972). Electron depth-dose distribution measurements in two-layer slab absorbers. *Radiat. Res.* 52, 429-447.
- Evans, R. D. (1968). X-ray and y-ray interactions. In "Radiation Dosimetry" (F. H. Attix and W. C. Roesch, eds.) 2nd ed., Vol. 1, pp. 94-156. Academic Press, New York.
- Ewart, G. M., and Rogers, D. W. O. (1982). "Calculated Thick Target Bremsstrahlung Angular Distributions and Shielding Calculations," Rep. PXNR-2640. National Research Council of Canada, Ottawa.
- Eyges, L. (1948). Multiple scattering with energy loss. *Phys. Rev.* 74, 1534-1535.
- Ford, R. L., and Nelson, W. R. (1978). "The EGS Code System (Version 3)," SLAC Rep. 210. Stanford University, Stanford, California.
- Fuller, E. G., and Gerstenberg, H. M. (1978). "Photonuclear Data Index," NBS Spec. Publ. 380, Suppl. 1. National Bureau of Standards, Washington, D. C.
- Garth, J. C., Burke, E. A., and Woolf, S. (1980). The role of scattered radiation

- in the dosimetry of small device structures. *IEEE Trans. Nucl. Sci.* NS-27, 1459-1464.
- Goudsmit, S., and Saunderson, J. L. (1940). Multiple scattering of electrons. *Phys. Rev.* 57, 24-29.
- Grosswendt, B., and Waibel, E. (1975). Determination of detector efficiencies for gamma-ray energies up to 12 MeV. *Nucl. Instrum. Methods.* 131, 143-156.
- Halbleib, J. A., and Melhorn, T. A. (1984). "ITS: The Integrated TIGER Series of Coupled Electron/Photon Monte Carlo Transport Codes," Sandia Rep. SAND84-0073. Sandia National Laboratories, Albuquerque, New Mexico.
- Halbleib, J. A., and Morel, J. E. (1978). "Improved Atomic Shell Excitation and Relaxation in the Tiger Series Codes," Sandia Rep. SAND78-0580. Sandia National Laboratories, Albuquerque, New Mexico.
- Halbleib, J. A., and Vandevender, W. H. (1975). TIGER. *Nucl. Sci. Eng.* 57, 94-95.
- Halbleib, J. A., and Vandevender, W. H. (1976a). CYLTRAN. *Nucl. Sci. Eng.* 61, 288-289.
- Halbleib, J. A., and Vandevender, W. H. (1976b). "CYLTRAN-Cylindrical Geometry Multimaterial Electron or Photon Monte Carlo Transport Code," ORNL Rep. CCC 280. Radiation Shielding Information Center, Oak Ridge Nat. Lab. Oak Ridge, Tennessee.
- Hammersley, J. M., and Handscomb, D. C. (1964). "Monte Carlo Methods." Wiley, New York.
- Han, K., Ballon, D., Chui, C., and Mohan, R. (1987). Monte Carlo simulation of a cobalt-60 beam. *Med. Phys.* 14, 414-419.
- Harder, D., and Schulz, H. J. (1972). Some new physical data for electron beam dosimetry. *Proc. Eur. Congo Radiol.* 2nd pp. 475-481. [The stated experimental curve is not actually given in this work although it is obviously associated with it, being also referenced by ICRU (1984a).
- Higgins, P. D., Sibata, C. H., and Paliwal, B. R. (1985). Determination of contaminant-free build-up for ^{60}Co . *Phys. Med. Biol.* 30, 153-162.
- Hubbell, J. H. (1969). "Photon Cross Sections, Attenuation Coefficients and Energy Absorption Coefficients from 10 keV to 100 GeV," NSRDS-NBS29. National Bureau of Standards, Washington, D.C.
- Hubbell, J. H. (1982). Mass attenuation and energy-absorbing coefficients. *Int. Appl. Radiat. Isot.* 33(11).
- Hubbell, J. H., and Overbo, I. (1979): Relativistic atomic form factors and photon coherent scattering cross sections. *J. Phys. Chem. Ref. Data* 8, 69-105.
- Hubbell, J. H., Veigle, W. J., Briggs, E. A., Brown, R. T., Cromer, D. T., and Howerton, R. J. (1975). Atomic form factors, incoherent scattering functions and photon scattering cross sections. *J. Phys. Chem. Ref. Data* 4, 471-538.
- International Commission on Radiation Units and Measurements (ICRU), (1984a). "Radiation Dosimetry: Electron Beams with Energies Between 1 and 50 MeV," ICRU Rep. No. 35. ICRU, Bethesda, Maryland.
- International Commission on Radiation Units and Measurements (ICRU)

- (1984b). "Stopping Powers for Electrons and Positrons," ICRU Rep. No. 37. ICRU, Bethesda, Maryland.
- Johns, P. C., and Yaffe, M. J. (1983). Coherent scatter in diagnostic radiology. *Med. Phys.* 10,40-50.
- Jordan, T. M. (1986). Adjoint electron Monte Carlo calculations. *Trans. Am. Nucl. Soc.* 52, 382-383.
- Kahn, H. (1956). Use of different Monte Carlo sampling techniques. In "Symposium on Monte Carlo Methods" (H. A. Meyer, ed.), pp. 146-190. Wiley, New York.
- Kim, L., Pratt, R. H., Seltzer, S. M., and Berger, M. J. (1986). Ratio of positron to electron bremsstrahlung energy loss: An approximate scaling law. *Phys. Rev. A* 33, 30023009.
- Knuth, D. E. (1981). "The Art of Computer Programming," 2nd eds., Vol. 2. Addison Wesley, Reading, Massachusetts.
- Koch, H. W., and Motz, J. W. (1959). Bremsstrahlung cross-section formulas and related data. *Rev. Mod. Phys.* 31, 920-955.
- Landau, L. (1944). On the energy loss of fast particles by ionization. *J. Phys. (Moscow)* 8, 201-205.
- Lewis, H. W. (1950). Multiple scattering in an infinite medium. *Phys. Rev.* 78, 526-529.
- Lockwood, G. J., Ruggles, L. E., Miller, G. H., and Halbleib, J. A. (1980). "Calorimetric Measurement of Electron Energy Deposition in Extended Media-Theory vs Experiment," Rep. No. 79-0414. Sandia National Laboratories, Albuquerque, New Mexico.
- Lund, T. (1981). "An Introduction to the Monte Carlo Method," Rep. HS-RP/067. CERN, Geneva.
- Mach, H., and Rogers, D. W. O. (1984). A measurement of absorbed dose to water per unit incident 7 MeV photon fluence. *Phys. Med. Biol.* 12, 1555-1570.
- Mackie, T. R., Bielajew, A. F., Rogers, D. W.O., and Battista, J. J. (1988). Generation of photon energy deposition kernels using the EGS Monte Carlo code. *Phys. Med. Biol.* 33, 1-20.
- Marsaglia, G. (1968). Random numbers fall mainly in the planes. *Proc. Natl. Acad. Sci. U.S.A.* 61,25-28.
- McGrath, E. J., and Irving, D. C. (1975). "Techniques for Efficient Monte Carlo Simulation," Vols I, II, and III. Rep. ORNL-RSIC-38. Radiation Shielding Information Center, Oak Ridge National Laboratories, Oak Ridge, Tennessee.
- Messel, H., and Crawford, D. F. (1970). "Electron-Photon Shower Distribution Function." Pergamon, Oxford.
- Mohan, R., Chui, C., and Lidofsky, L. (1985). Energy and angular distributions of photons from medical linear accelerators. *Med. Phys.* 12,592-597.
- Moliere, G. Z. (1948). Theorie der Streuung schneller geladener Teilchen II Mehrfach-und Vielfachstreuung. *Z. Naturforsch. A* 3A, 78-97.

- Morel, J. E., and Lorence, L. J. (1986). Recent developments in discrete ordinates electron transport. *Trans. Am. Nucl. Soc.* 52, 384-385.
- Nahum, A. E. (1975). Calculations of electron flux spectra in water irradiated with megavoltage electron and photon beams with applications to dosimetry. Ph.D. Thesis. University Microfilms International 77-70006. University of Michigan, Ann Arbor.
- Nahum, A. E. (1978). Water/air stopping power ratios for megavoltage photon and electron beams. *Phys. Med. Biol.* 23, 24-38.
- Nahum, A. E. (1983). "Stopping Power Ratios and Dosimetry," NRCC Rep. PXNR-2653. National Research Council of Canada, Ottawa.
- Nath, R., and Schulz, R. J. (1981). Calculated response and wall correction factors for ionization chambers exposed to ^{60}Co gamma-rays. *Med. Phys.* 8, 85-93.
- National Council on Radiation Protection and Measurements (NCRP) (1977). Radiation Protection Design Guidelines for 0.1-100 MeV Particle Accelerator Facilities, Rep. NCRP-51. NCRP, Washington, D.C.
- Nelson, W. R., Hirayama, H., and Rogers, D. W. O. (1985). "The EGS4 Code System," SLAC Rep. 265. Stanford Linear Accelerator Center, Stanford, California.
- Nelson, W. R., Jenkins, T. M., and Lockman, W. S. (1986). "Subroutine EDGSET." Stanford Linear Accelerator Center, Stanford, California (private communication).
- Nordic Association of Clinical Physicists (NACP) (1980). Procedures in external radiation therapy dosimetry with electron and photon beams with maximum energies between 1 and 50 MeV. *Acta Radiol. Oncol.* 19,55-79.
- O'Dell, A. A., Sandifer, C. W., Knowlen, R. P., and George, W. D. (1968). Measurement of absolute thick-target bremsstrahlung spectra. *Nucl. Instrum. Methods* 61, 340.
- Ogunleye, O. T., Attix, F. H., and Paliwal, B. R. (1980). Comparison of Burlin cavity theory with LiF TLD measurements for cobalt-60 gamma rays. *Phys. Med. Biol.* 25, 203-213.
- Persliden, J., and Alm Carlsson, G. (1984). Energy imparted to water slabs by photons in the energy range 5-300 keV. Calculations using a Monte Carlo photon transport model. *Phys. Med. Biol.* 29, 1075-1088.
- Persliden, J., and Alm Carlsson, G. (1986). Calculation of the small-angle distribution of scattered photons in diagnostic radiology using a Monte Carlo collision density estimator. *Med. Phys.* 13, 19-24.
- Petti, P. L., Goodman, M. S., Sisterson, J. M., Biggs, P. J., Galbriel, T. A., and Mohan, R. (1983). Sources of electron contamination for the Clinac-35 25-MV photon beam. *Med. Phys.* 10, 856-861.
- Rogers, D. W. O. (1982). More realistic Monte Carlo calculations of photon detector response functions. *Nucl. Instrum. Methods* 199, 531-548.
- Rogers, D. W. O. (1984a). Low energy electron transport with EGS. *Nucl. In-*

- strum. *Methods Phys. Res., Sect. A* 227, 535-548.
- Rogers, D. W. O. (1984b). Fluence to dose equivalent conversion factors calculated with EGS3 for electrons from 100 keV to 20 GeV and photons from 11 keV to 20 GeV. *Health Phys.* 46, 891-914.
- Rogers, D. W.O., and Bielajew, A. F. (1984). "The Use of EGS for Monte Carlo Calculations in Medical Physics," Rep. PXR-2692. National Research Council of Canada, Ottawa.
- Rogers, D. W.O., and Bielajew, A. F. (1985). Calculated buildup curves for photons with energies up to ^{60}Co . *Med. Phys.* 12,738-744.
- Rogers, D. W.O., and Bielajew, A. F. (1986). Differences in electron depth-dose curves calculated with EGS and ETRAN and improved energy-range relationships. *Med. Phys.* 13,687-694.
- Rogers, D. W.O., Bielajew, A. F., and Nahum, A. E. (1985a). Ion chamber response and A_{wall} correction factors in a ^{60}Co beam by Monte Carlo simulation. *Phys. Med. Biol.* 30, 429-443.
- Rogers, D. W.O., Ewart, G. M., and Bielajew, A. F. (1985b). "Calculation of Contamination of the ^{60}Co Beam from an AECL Therapy Source," Intern. Rep. No. PXR-2710. National Research Council of Canada, Ottawa.
- Rogers, D. W.O., Ewart, G. M., Bielajew, A. F., and Van Dyk, G. (1988). Calculation of electron contamination in a ^{60}Co therapy beam. *Proc. IAEA Symp. Dosimetry in Radiotherapy Pap.* IAEA-SM-298/48, pp. 303-312.
- Roy, R. R., and Reed, R. D. (1968). "Interactions of Photons and Leptons with Matter." Academic Press, New York. Scott, W. T. (1963). The theory of small-angle multiple scattering of fast charged particles. *Rev. Mod. Phys.* 35, 231-313.
- Seltzer, S. M. (1989). An overview of ETRAN Monte Carlo methods for coupled electron! photon transport calculation. In "Monte Carlo Transport of Electrons and Photons Below 50 MeV" (W. R. Nelson, T. M. Jenkins, A. Rindi, A. E. Nahum, and D. W. O. Rogers, eds.). pp. 151-181. Plenum, New York.
- Seltzer, S. M., and Berger, M. J. (1974). Transmission and reflection of electrons by foils. *Nucl. Instrum. Methods* 119, 157-179.
- Seltzer, S. M., and Berger, M. J. (1986). Bremsstrahlung spectra from electron interactions with screened atomic nuclei and orbital electrons. *Nucl. Instrum. Methods Phys. Res., Sect. B* 12, 95-134.
- Seltzer, S. M., Hubbell, J. H., and Berger, M. J. (1978). Some theoretical aspects of electron and photon dosimetry. *Proc. Symp. Natl. Int. Stand. Radiat. Dosim., Vol. 2*, pp. 3-43. Shortt, K. R., Ross, C. K., Bielajew, A. F., and Rogers, D. W. O. (1986). Electron beam dose distributions near standard inhomogeneities. *Phys. Med. Biol.* 31,235-249.
- Shreider, Y. A., ed. (1966). "The Monte Carlo Method." Pergamon, Oxford.
- Spencer, L. V., and Attix, F. H. (1955). A theory of cavity ionization. *Radial. Res.* 3, 239 254. Sternheimer, R. M., and Peierls, R. F. (1971). General expression for the density effect for the ionization loss of charged particles.

- Phys. Rev. B 3,3681-3692. . Stevens, P. N. (1980). Notes from a course on Monte Carlo transport. University of Tennessee, Knoxville.
- Storm, E. and Israel, H. E. (1970). Photon cross sections from 1 keV to 100 MeV for elements $Z = 1$ to $Z = 100$. Nucl. Data, Sect. A 7, 565-681.
- Varley, B. J., Kitching, J. E., and Leo, W. (1981). The response of germanium detectors to monoenergetic electron, positron and gamma ray beams. Nucl. Instrum. Methods 190, 543-554.
- Veigle, W. J. (1973). Photon cross sections from 0.1 keV to 1 MeV for elements $Z = 1$ to $Z = 94$. At. Data Tables 5, 51-111.
- Williamson, J. F. (1987). Monte Carlo evaluation of kerma at a point for photon transport problems. Med. Phys. 14,567-576.
- Williamson, J. F., Deibel, F. C., and Morin, R. L. (1984). The significance of electron binding corrections in Monte Carlo photon transport calculations. Phys. Med. Biol. 29, 1063-1073.
- Wong, J. W., Henkelman, R. M., Fenster, A., and Johns, H. E. (1981). Second scatter contribution to dose in a ^{60}Co beam. Med. Phys. 8, 755-782.
- Wyckoff, J. M., Pruitt, J. S., and Svensson, G. (1971). Dose vs angle and depth produced by 20 to 100 MeV electrons incident on thick targets. Proc. Int. Congr. Prot. Against Accelerator and Space Radiat., Vol. 2, CERN, Geneva Rep. CERN-71-16; also reported in NCRP (1977).